Dislocation-based continuum models of crystal plasticity on the micron scale

Nikolaos Nikitas

A thesis submitted for the degree of Doctor of Philosophy.
The University of Edinburgh.
February 2008

Abstract

The miniaturization trends on electronic components manufacturing, have challenged conventional knowledge on materials strength and deformation behavior. ”The smaller the stronger” has become a commonplace expression summarizing a multitude of experimental findings in micro-scale plasticity, and modelling tools capable of capturing this distinctive reality are in urgent demand. The thesis investigates the ubiquitous size effects in plastic deformation of micron-scale specimens. Tracing the source of such a behavior to the constituent elements of plastic deformation, we use as starting point the dynamics of discrete dislocations and try to embody them into a continuum framework. The thesis is structured in two independent parts.

In the first part the question why size effects occur in constrained geometries is addressed. A systematic investigation of the connection between internal and external length scales is carried out in a system where dislocations, in the form of continuous lines embedded in a three-dimensional isotropic medium, move, expand, interact, and thus create plastic distortion on the deforming body. Our modelling strategy utilizes a set of deterministic evolution equations on dislocation densities for describing the stress-driven evolution of the material’s internal state. These transport-like equations simultaneously serve the role of constitutive laws describing the deformation of the stressed body. Subsequent application to three benchmark problems is found to give good agreement both with experiment and discrete dislocation dynamics simulation.

The second part of this thesis focuses on the heterogeneity and intermittency of deformation processes on the micro scale. Recent experimental results question the concept of smooth and homogeneous plastic flow with fluctuations that average out above a certain scale. Bursts of activity, which follow power-law size distributions and produce long-range correlated deformation patterns, seem to pertain even on scales far greater than the atomic one. In short, plasticity in this view appears as a ’crackling noise’ phenomenon similar to other irregular and burst-like processes such as earthquakes or granular avalanches. But then why do we witness smooth stress-strain curves on macroscopic sample testing? Concepts originating from Self Organized Criticality and pinning theories are employed for producing an efficient continuum description which is then used to study the effect of intrinsic and extrinsic deformation parameters on the fluctuation phenomena. It is deduced that hardening, load driving and specimen size, are all decisive on constraining fluctuating behavior, and limits of classical theory’s applicability can be drawn.

Declaration of originality

I hereby declare that the research recorded in this thesis and the thesis itself was composed and originated entirely by myself in the School of Engineering and Electronics at The University of Edinburgh.

Nikolaos Nikitas

Acknowledgements

To all those who taught me and made me feel that I can think as a scientist.

I owe a great debt of gratitude to my supervisor M. Zaiser, who, acting as my mentor, guided me to new horizons, taught me a lot of values of philosophy of science and life, strengthened my self confidence as a young researcher, and helped me to successfully complete my first research endeavor. As a matter of fact, without his understanding, his advice, his critical views, and his inspiration, and even more without his friendly attitude towards me, I would not have concluded in this thesis.

I am also deeply indebted to the world top academic authority of Professor Elias Aifantis for introducing me into the field of micro-scale mechanics and for the chance he gave me to work beside leading scientists on a very competitive field.

I heartly thank Edinburgh University for the PhD course and Marie Curie Institute for the financial support through SizeDePen research training network.

Last but not least, I want to thank my family in Drama for their practical help, understanding, encouragement and love throughout the entire period of my research at Edinburgh.

Contents

List of figures

List of tables

Acronyms and abbreviations

AFM	atomic force microscopy
CDDD	continuum density-based dislocation dynamics
DDD	discrete dislocation dynamics
fcc	face centered cubic
GND	geometrically necessary dislocation
rms	root mean square
RVE	representative volume element
SOC	self organized criticality
SWLI	scanning white-light interferometry
2D	two-dimensional space
3D	three-dimensional space
3DDD	three-dimensional dislocation dynamics

Nomenclature

Whenever possible notation has been defined in the text of this thesis. This list contains notations which are used repeatedly.

α	Taylor flow stress coefficient
$\boldsymbol{\alpha}$	dislocation density tensor
$\boldsymbol{b}$	Burgers vector
b	Burgers vector magnitude
bh^2	moment scaling coefficient (here b stands for width)
B	dislocation mobility
$\boldsymbol{C}$	Hooke tensor
d	space dimension
D	back stress coefficient
D	back stress coefficient tensor
$\boldsymbol{e}_{\mathrm{g}}$	unit vector on the dislocation glide direction
$\boldsymbol{e}_{\mathrm{t}}$	unit vector on the dislocation tangential direction
E	Young's modulus
E	generic energy release
G	shear modulus
h	film thickness
H	Hurst exponent
k	curvature
K	strain hardening parameter
L	deformation length
M	bending moment
$\boldsymbol{M}$	projection tensor
$\boldsymbol{n}$	unit normal vector
N	generic variable denoting total
$p(...)$	probability density function
q	flow stress fluctuation amplitude evolution parameter
Q	flow stress fluctuation amplitude

Q	flow stress fluctuation amplitude
$\boldsymbol{r}$	position vector
R	radius of curvature
R_{e}	edge segment dislocation density
R_{s}	screw segment dislocation density
s	avalanche size
s_0	avalanche size cutoff
S	closed surface boundary
t	generic thickness
T	line tension
$\boldsymbol{u}$	deformation vector
v	dislocation velocity
v_ϕ	dislocation rotation velocity
V	volume
$\boldsymbol{\beta}$	distortion tensor
$\boldsymbol{\beta}^{\mathrm{pl}}$	distortion tensor
γ	plastic shear strain
$\dot{\gamma}$	plastic strain rate
γ_{corr}	correlation shear strain
$\Gamma(...)$	elastic kernel
$\delta(...)$	Dirac's delta function
ϵ	scaled plastic strain variable
$\boldsymbol{\varepsilon}$	strain tensor
$\boldsymbol{\varepsilon}^{\mathrm{pl}}$	plastic strain tensor
$\boldsymbol{\varepsilon}^{\mathrm{tot}}$	total strain tensor
θ	slip system inclination
Θ	hardening coefficient
κ	avalanche exponent
κ_{e}	average edge dislocation density
κ_{s}	average screw dislocation density
Λ	driving spring stiffness
μ	viscoplastic coefficient
ν	Poisson ratio
ξ	dislocation-dislocation correlation length

ρ	dislocation density
σ	stress tensor
σ_∞	stress for infinite body
τ	resolved shear stress
τ_b	pileup back stress
τ_ext	external/driving stress
τ_f	flow stress
τ_int	internal shear stress
τ_mf	mesoscopic stress
τ_lt	line tension stress
τ_surf	stress from boundary condition correction
τ_y	yield stress
ϕ	dislocation orientation
$\langle \ldots \rangle$	average
$\times$	vector product
$\otimes$	dyadic product

Part 0

Introduction and General Background

Chapter 0.1
Motives, means and goals

Continuum theories, in the form of elasticity theory, appeared in the first half of the 19th century to serve demands set by the technological progress of the time. The concept of continuum geometrical space as adopted at that time was revolutionary as it opposed the Newtonian mechanics of discrete objects, and evidently its applicability was severely questioned.

Since then a lot of new findings made their way into science. Macroscopic material objects - particularly metals which are of great importance in industrial applications - proved to possess a crystalline structure. New materials with custom-made microstructures were tailored. Nonetheless engineering mechanics kept the notion of bodies filling space in a continuous manner. Thus the simple question arises why we carry on describing discrete systems by a continuum theory and how adequate that can be.

0.1.1 Motivating the problem

Exclusion of the discreteness of nature from the mechanics of deforming bodies is obviously a simplification of a many body problem which otherwise cannot really be solved. The choice of a continuum framework endows us with many powerful mathematical tools and moreover describes in a simple straightforward way the state of a body by means of a small number of variables. These are the great virtues due to which engineering mechanics persists in the idea of continua which the current work takes as a starting point.

It has to be stressed at this point that for a great number of problems the foresaid exclusion of the structural discreteness of matter cannot be total. We may work on an idealized medium which fills space continuously, but some signatures of the discrete fabric of this medium may have to be retained for adequately modelling its properties.

This became rather clear in our ages where high-end technology expanded to extreme length scales. On the one hand, for large-scale constructions the continuum framework proved to be

fully adequate. The building of bridges or airplanes is not hampered by the fact that we regularly use continuum approximations in their design. With the exception of fatigue our understanding of the design of large structures is conceptually well-founded and has to cope mainly with implementation issues. On the other hand the miniaturization of, mostly, advanced electronic devices brought up concerns and problems which indicate fundamental deviations between the predictions of continuum models and the actual behavior of very small structures. As we reach dimensions close to those of the elementary objects nature uses to produce deformation, continuum-based models face difficulties in providing an efficient description of reality.

The most prominent case where such problems become apparent applies to the plasticity of crystalline bodies with dimensions of the order of microns. Phenomena such as size-dependent strength and hardening, deformation patterning, surface roughening and fatigue are not straightforwardly captured by traditional continuum models. An obvious strategy for extending or adapting such models to the micron scale is to look into the underlying mechanisms that drive the plastic deformation.

0.1.2 From materials physics to continuum mechanics

It is known for long that plasticity of crystalline materials is accommodated by the existence and motion of defects in the otherwise perfect lattice structure. Dislocations, which are the most important of these defects, are gliding inside the crystal along certain planes under the influence of local stresses, and their motion produces the plastic distortion of the stressed body. Hence it is natural to try and implement in a continuum model of plasticity some additional dislocation-based variables, which would provide a mapping between the behavior of the continuous body and the mechanisms that govern the discrete dislocations. This might allow us to keep track of the internal state of the deforming body during a process which may exhibit path-dependence and memory. In a continuum formulation such variables have necessarily to assume the character of density measures.

In this spirit the current thesis wants to contribute to the vast field of continuum mechanics by investigating the descriptive abilities of two physically motivated plasticity models which include dislocation mechanisms into continuum plasticity.

Using the well-defined framework of crystal-plasticity our freedom consists in defining constitutive equations which take account of the dislocation processes. The ultimate goal will be to

capture with as little phenomenology as possible the peculiarities of plastic deformation that emerge on the micron scale, and to answer the basic question that each consistent plasticity model should answer: What is the collective response of a given microstructure to a given external driving? We choose two distinct paths to address different aspects of this problem. Consequently this work will consist of two distinct parts.

Chapter 0.2
Organization of the present thesis

The present thesis is divided into an introductory part which discusses the general background of the work and establishes some important concepts and notations. The subsequent parts I and II build on this common ground but can be read independently.

0.2.1 Structure: Part I

In Part I of this thesis we attempt to obtain a rigorous description of the interplay between boundary conditions, system sizes and deformation behavior during constrained plastic flow. In particular we will address the question why size effects occur in constrained geometries. The issue of size effects leads us to a systematic investigation of the connection between internal and external length scales in a system where dislocations, in the form of continuous lines embedded in a three-dimensional isotropic medium, move, expand, interact, and thus create plastic distortion of the deforming medium. Our modelling strategy consists in deriving a set of deterministic evolution equations for densities which describe the stress-driven evolution of the dislocation distribution. These equations simultaneously serve the role of constitutive laws describing the deformation of the stressed body. Naturally such equations must have the form of transport equations.

We denote as mesoscopic the length scale of the discrete defects (the scale of the dislocation spacing), as opposed to the macroscopic scale and to the microscopic or atomistic scale which is set by the crystal lattice. The root of the problem resides in the fact that, on the mesoscopic scale, spatial variations of the plastic distortion occur over distances comparable to the spacing between individual defects. Consequently, the interactions between discrete defects, and the length scales associated with their spacing, must be explicitly incorporated into the continuum framework.

In Chapter I.1 we give a short synopsis of the experimental background, the theoretical work done on the field by other authors, and its influence on the present thesis. We then in Chapter

I.2 define the theoretical description that serves as the foundation of our analysis. Starting from a set of discrete dislocation lines, we use an averaging procedure to obtain a set of equations for the evolution of the dislocation population. All derivations and assumptions entering our analysis are given in this Chapter. Later in Chapter I.3 we apply the established framework to three benchmark problems of confined plastic flow. Namely we treat, for the special case of plane-strain deformation, the shearing (in both single and double slip) and bending of a thin film. We close this section in Chapter I.4 by discussing our results in relation with the results of other authors, experimental findings, and results of discrete dislocation dynamics simulations. Also we explore further elaborations of the present approach, and discuss perspectives and research possibilities.

0.2.2 Structure: Part II

In the second part of this thesis we focus on another important aspect of microplasticity, namely the intrinsic randomness of deformation processes on the micro scale. The concept of a macroscopically smooth and homogeneous plastic flow with fluctuations that average out above the scale of a 'representative volume element' (RVE) was recently put into challenge. Classical theory's perception is that although discreteness of the defect structure produces fluctuations in the microscopic deformation process, the influence of deviations is smeared out as we pass from the RVE to larger scales, since otherwise we would not be observing smooth stress-strain curves.

Recent experimental results, however, revealed a very different image where decreasing size brings up increasing variations from the expected average behavior even at scales that are well above the scale of the elementary defects. Bursts of activity, which follow power-law size distributions and produce long-range correlated deformation patterns, feature prominently in this image. In short, plasticity in this view appears as a 'crackling noise' phenomenon similar to other irregular and burst-like processes such as earthquakes or granular avalanches. It has even been claimed that the fluctuation phenomena are completely scale-free, which would imply that a RVE cannot be defined on any scale. In Part II of the present thesis, we will systematically investigate the validity of this claim.

The nature of our investigation requires this time a stochastic formulation rather than a deterministic approach based on reaction-transport equations as before. We propose a simple

constitutive model based on the concept that the local flow stress of every volume element is a fluctuating function of the local strain. Physically these fluctuations result from randomness in the arrangement of the microstructural defects that produce the plastic strain. Fluctuations in the local flow stress lead to shear strain fluctuations and these in their turn to stress redistribution over the whole volume. This may trigger additional deformation in other volume elements and, as a consequence, deformation proceeds in irregular bursts. In this way, the model succeeds in accounting for intermittency and randomness of the plastic flow which proceeds in discrete events.

We then examine what processes determine the statistics of these events, and how the statistical characteristics of plastic flow depend on the size of the deforming body. It turns out that the size of deformation bursts is limited by local hardening, which is contributing an additional back stress that impedes deformation and prevents the growth of infinitely big avalanches.

In Chapter II.1 we outline our modelling strategy and give references to previous works with the same objectives. In Chapter II.2 we introduce the model and describe its numerical implementation together with the relation that our modelling holds with real dislocation behavior. In Chapter II.3 we present our results regarding the formation and statistical properties of deformation bursts. Chapter II.4 closes this part by short discussion of our findings and a comparison with the results of experiments and also of recent dislocation dynamics simulations. We conclude with some proposals for future modifications and extensions of the model.

Chapter 0.3
General features of crystal plasticity theory

As plastic deformation we define the deformation of a solid body that remains after the applied driving loads are removed. By definition plasticity requires that relative positions of atoms inside the body are changed. This already indicates that plasticity is a structure sensitive process. For crystalline materials occurrence of plastic deformation involves the simultaneous occurrence of processes from the microscopic scale where plastic deformation involves the movement of atoms and breaking of bonds, over the mesoscopic scale where the unavoidably inhomogeneous and intermittent movement of discrete dislocation lines prevails, to the macroscopic scale where we witness homogeneous flow and smooth behavior.

We first discuss the conventional continuum mechanics approach towards crystal plasticity. There, the deforming continuum is not the structure-less continuum of usual elasticity theory because it preserves the key ingredient of crystal structure, namely the crystallographic directions.

0.3.1 Deformation by crystallographic slip

The predominant mode of plastic deformation in crystals, in particular at high stresses and low to moderate temperatures, is crystallographic slip. Other possible mechanisms like twinning and diffusive flow have a much more restricted field of applicability. Crystallographic slip has one very simple property: it restricts deformation to shear of adjacent lattice planes which leaves the crystal lattice invariant, i.e., the relative displacement of the planes must be a lattice vector or a multiple thereof. Accordingly, a slip system is defined through a unit normal vector $\boldsymbol{n}$ which characterizes a set of crystallographic planes (often the most densely packed planes in a given lattice structure), and through a lattice vector $\boldsymbol{b}$ contained in these planes. The *Burgers vectors* $\boldsymbol{b}$ are often the shortest lattice vectors in the lattice structure. The fact that accumulation of local slips builds the total plastic strain $\boldsymbol{\varepsilon}^{\mathrm{pl}}$ is expressed by the following relations (cf. [1–3]):

$$\boldsymbol{\varepsilon}^{\mathrm{pl}} = \sum_i \gamma^{(i)} \boldsymbol{M}^{(i)} \ , \quad \boldsymbol{M}^{(i)} = \frac{1}{2b}[\boldsymbol{b}^{(i)} \otimes \boldsymbol{n}^{(i)} + \boldsymbol{n}^{(i)} \otimes \boldsymbol{b}^{(i)}]. \tag{0.3.1}$$

Here the index i distinguishes the different slip systems, $\gamma^{(i)}$ are the respective scalar shear strains, b is the Burgers vector modulus and $\boldsymbol{M}^{(i)}$ is the symmetrized projection tensor. The driving stress for each slip system $\tau^{(i)}$, called the resolved shear stress, is obtained as the inner product of the stress tensor $\boldsymbol{\sigma}$ and $\boldsymbol{M}^{(i)}$:

$$\tau^{(i)} = \boldsymbol{M}^{(i)} \cdot \boldsymbol{\sigma}. \tag{0.3.2}$$

What has to be added to the above framework for treating a general elastic-plastic problem is information characterizing the material's behavior. Such equations, which define relations between stress and strains or strain rates, are called constitutive equations[1]. Their soundness eventually determines our ability to model a given problem. In other words, our need for a good model for plastic deformation behavior transforms into a need for a good constitutive law.

0.3.2 Constitutive modelling

In the following we discuss, in sequence of increasing complexity, a number of commonly used constitutive laws. In each case, these laws contain one or more material-specific parameters which, in the context of phenomenological constitutive modelling, must be determined from deformation experiments. In this context it is important to keep in mind that the constitutive laws used in traditional engineering mechanics do not express fundamental physical concepts (this makes them different from, say, the equation of state of an ideal or real gas) but are simply mathematical expressions used to fit an observed material behavior, and to extrapolate it to more complicated deformation geometries. Different deformation paths, or deformation histories, may require different constitutive laws for obtaining reasonable predictions.

Linear plasticity. This is the simplest possible constitutive law we can implement. In its most basic form, commonly called ideal plasticity, it assumes that the solid body starts to flow like an ideal liquid as soon as the applied stress reaches a critical value τ_{y}. Upon unloading the elastic

[1]Regarding the material element as being at constant temperature on the time scale for which the behavior is described, the material response becomes principally a relation between the stress and the rate of strain increment.

properties are restored but the body remains with an irreversible deformation. The interesting phenomena of strength hardening and softening can be captured if this law is generalized by assuming that the flow becomes a linear function, increasing or decreasing respectively, of the strain. Furthermore this linear function can be replaced by any non-linear expression, which provides us with an even more flexible frame.

Linear viscoplasticity. This is the evident step to provide a simple constitutive law with rate dependency. In the spirit of the previous simple case, the flow stress now becomes a function of the applied strain rate (cf. [1, 2]):

$$\dot{\gamma} = \frac{1}{\mu} \begin{cases} (|\tau| - \tau_{\mathrm{y}})\mathrm{sign}(\tau) & , \ |\tau| > \tau_{\mathrm{y}} \\ 0 \quad else \end{cases} . \tag{0.3.3}$$

This equation states that the velocity of deformation scales with the excess of the driving over the yield stress and that the direction of deformation is dictated by the sign of the driving stress. μ is the viscoplastic rate coefficient. Such a solid after yielding behaves like a Newtonian fluid ('yield-stress fluid'). Again generalizations regarding the form of the strain rate function are feasible which use non-linear expressions for relating the stress and strain rate, and produce this way a greater family of models.

Phenomenological constitutive models were in many instances quite successful in characterizing macroscopically homogeneous deformation behavior. All of them share, however, the attribute that they originate from empirical observations and do not express any deeper physical insight. It is hence natural that sometimes the results deriving from such models, if extrapolated to altering conditions, do not show high accuracy or, even worse, cannot provide any adequate representation of the real phenomena. This problem is most pronounced once the scale of the deforming body reached the mesoscopic scale where the discrete nature of the elementary deformation processes becomes manifest. This leads to fluctuations of the deformation process, and to dependence of basic deformation properties on the size of the deforming body.

Part I

Size effects in constrained plastic flow

Chapter I.1
Introductory remarks

In view of the remarkable applications associated with the emerging areas of micro and nanotechnologies, plasticity researchers are performing mechanical tests of various specification on smaller and smaller scales. These experimental investigations indicate that the deformation behavior and the apparent material properties change as the size of the deforming sample approaches the micron range. The present chapter focuses on size-dependent changes in the measured material strength and investigates how these size effects can be modelled in terms of dislocation-based constitutive laws.

I.1.1 Internal length scales, deformation patterning, and size effects

Classical plasticity envisages the deforming body as a structure-free continuum. As a consequence, the deformation behavior described by classical plasticity theory is size independent. Real bodies, however, possess complicated and generally inhomogeneous microstructures. The characteristic scales of microstructural inhomogeneity define internal length scales of the deforming body, which in deforming crystals range from the 'elementary' length scale defined by the dislocation spacing over the scale of dislocation cells and sub-grains to the macroscopic scale of deformation bands [4, 5]. Classical plasticity is bound to break down once the characteristic scale of variation of the plastic strain field reaches one of these internal length scales. This was first recognized in the context of deformation instabilities in macroscopic samples, such as strain softening or strain rate softening behavior in unidirectional or cyclic plastic deformation [6] . In unstable plastic flow, deformation spontaneously localizes. As a consequence, inhomogeneous deformation patterns develop and deformation gradients become significant on the scale of the material microstructure. On the theoretical side, the mathematical formulation of classical plasticity becomes ill-posed in these situations and internal length scales associated with the microstructure must be taken explicitly into account in the constitutive models to restore the situation [7, 8].

Even in the absence of deformation instabilities, internal length scales become always relevant if the size of the deforming body is small enough. In this case, the interplay of internal and external length scales leads to a dependence of mechanical response on the structure size, usually in the sense that the smaller the size the stronger the response. Over the last years, size effects were observed in a wide range of deformation experiments performed on the micron and sub micron scale. A short synopsis of these experimental investigations is given in the following.

I.1.2 Experimental evidence

Some of the first experimental investigations of size effects were related to particle strengthening of materials: In alloys strengthened by the precipitation of hard second-phase particles it was found that small particles are more efficient in introducing enhanced strength properties than larger ones of the same volume fraction [9, 10]. Another early observation of a size effect is the finding that fine-grained metals are stronger than those with coarse grains (see for example [11]); the so-called Hall-Petch behavior.

The most influential and significant works for the understanding of size-effects came some years later with the implementation of experiments where the mode of loading introduces quantifiable heterogeneities of the deformation field in the form of strain gradients. Such experiments include bending of thin beams where the strain has a finite surface value that becomes zero when reaching the neutral axis, torsion of thin wires where again the strain distributes so as to attain a zero value along the twist axis, and indentation where the plastic zone expands over a limited region.

Fleck et al. performed torsion and uniaxial tension experiments on thin polycrystalline copper (99.99% purity) wires with diameters ranging from 12 to 170 $\mu\mathrm{m}$. For deformation in torsion they observed an apparent strengthening with diminishing diameter as shown in Figure I.1.1 (left). For uniaxial tension, on the other hand, no pronounced size effect was noted and the small strength scatter, which never exceeded 10% (as shown in Figure I.1.1 right), was attributed to grain size effects.

The latter argument was rigorously re-examined in a recent elaborate treatise of Uchic et al [12] where size effects of the overall physical sample dimensions were studied in the absence of any gradient induced heterogeneities. It was noticeably identified that for simple compression experiments on metallic single crystals the interplay between the intrinsic deformation

mechanisms and the geometric characteristics of the sample can bring upon striking size effected behavior which up to now was totally ignored. The treatise outlines for various metals the transition from bulk to whisker-like behavior and clarifies the extreme, unexplained up to now, differences in the intermediate size regime which is of highest interest for practical applications.

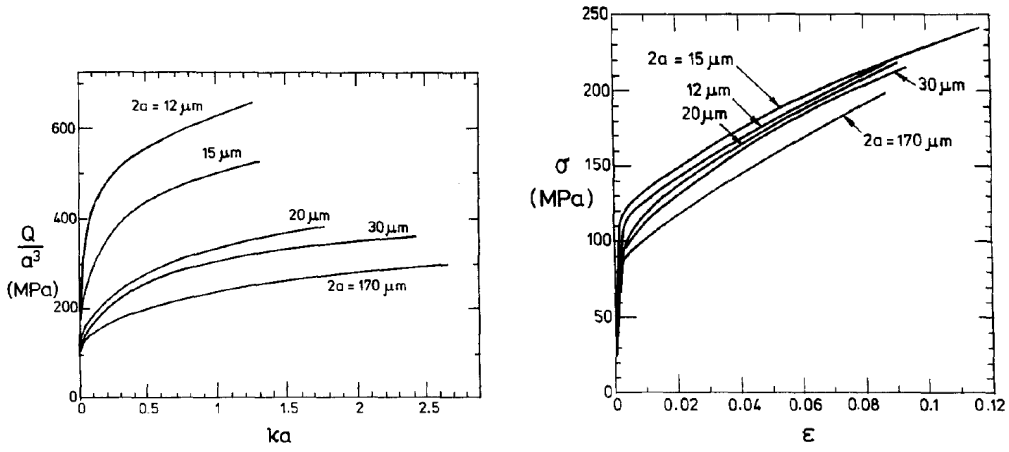

Figure I.1.1: *Right: Tension stress-strain curves for copper wires of diameter* $2a$ *in the range of* 12-170 μm*. There is only a small effect of wire diameter on the behavior. Left: Torsional response; Plots of normalized torque* $\frac{Q}{a^3}$ *vs. twist* ka*. There is a very strong size effect. After Fleck et al. [13]*

Analogous results were recorded by Stölken and Evans [14] for microbending where again the deformation mode imposes a strain gradient on the specimen scale. Their course of testing included again a series of uniaxial tension tests as well as bending tests for thin nickel (of high purity 99.99%) strips with thickness 12-50 μm. For bending a very distinct size effect as illustrated in Figure I.1.2 is found, indicating that that strength can become two to three times greater when the size is reduced by a factor of 4. The same experimental layout was later followed in a series of tests by Shrotriya [15]. The results were in agreement with the earlier work although the specimens were prepared with a different fabrication method.

A modified method was used by Motz et al. [16] in extracting microbending results. They used a micron-sized copper single crystal cantilever with thickness t between 1 and 7.5 μm to quantify the magnitude of size effect. The outcome produced out of this course was a bending response where the flow stress increased with decreasing thickness as $t^{-1.14}$, as depicted in Figure I.1.3. This situation roughly corresponds to an 'enhanced' Orowan mechanism (flow stress proportional to $\propto t^{-1}$) which is in agreement with our findings detailed in the following. Generally , although the mechanical setup may differ, the qualitative trend is captured by our

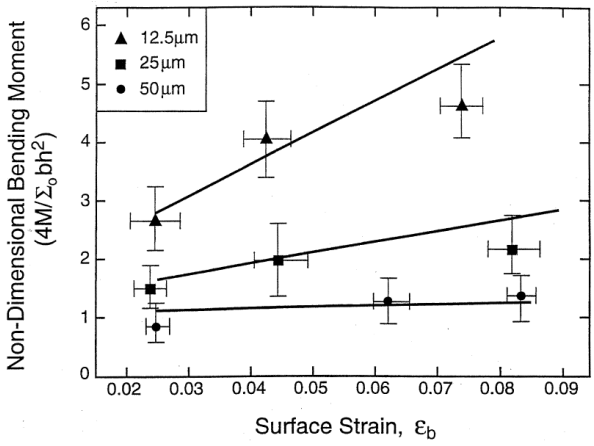

Figure I.1.2: *Plots of bending moment against the surface strain for* 12-$50\ \mu\mathrm{m}$ *foil thicknesses. The non-dimensional moment,* $M/\Sigma_o bh^2$*, is used for comparison to be more clear. Scaling with the tension yield strength* Σ_o *is carried out to reduce the grain size influence. Taken after Stölken and Evans [14]*

modelling in all cases, yielding a close match with experimental work.

An additional work worth referring is definitely that of Haque and Saif [17]. Their field of investigation was extended to nanosized aluminum samples and MEMS based techniques were used for fabrication purposes. Their results demonstrate that the physical mechanisms governing plasticity change with decreasing size and that a threshold size exists where even dislocation based models break down.

In the following we present briefly the main strategies that have been used for theoretically modelling the size dependent mechanical performance observed in micron-scale samples.

I.1.3 Gradient-dependent constitutive models

In a formal manner, size dependence can be modelled by using constitutive models which relate the stress not only to strain and strain rate, but also to gradients of these quantities. For dimensional reasons, the corresponding terms must contain pre-factors with the dimension of a length, which may be related to some physical length scale in the microstructure of the deforming solid. Evidently, the deformation response predicted by such models will depend on the ratio of the external and internal length scales. Following this idea, numerous phenomenological models have been proposed which incorporate strain gradient terms into constitutive laws for continuum plasticity [13, 18–22].

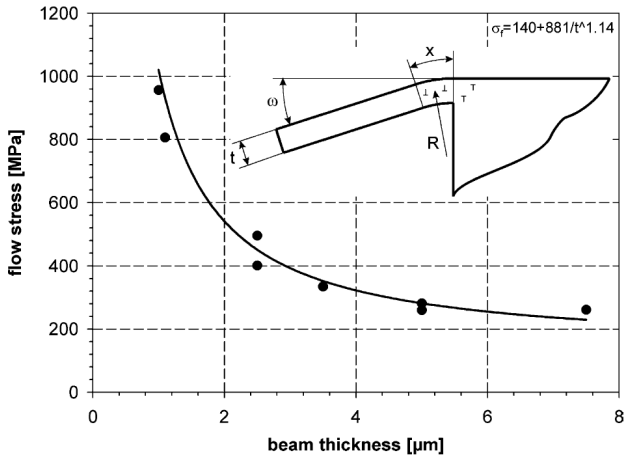

Figure I.1.3: *Dependence of the flow stress on micro-beam thickness. Flow stress can increase up to five times. The fit of the data points (solid line) shows a* $\propto t^{-1.14}$ *dependence of the flow stress.Taken after Motz et al. [16]*

The main problem of these phenomenological models is that there is simply too much freedom in the ways gradient terms might be added to a constitutive law. The freedom not only concerns the terms in the constitutive equations, but also the higher-order boundary conditions required to make the problem mathematically well-posed. This has led to a bewildering variety of models. Some authors have tried to motivate their models through arguments invoking geometrically necessary dislocations (e.g. [18, 19], for an overview see [23]) but even these 'physically based' gradient theories rely on several ad-hoc assumptions. (For a critical discussion, see Zaiser and Aifantis [24].) The traditional approach of engineering mechanics is to base constitutive models on extensive and systematic experimentation. On the micro scale, this is difficult for several reasons. Specimen preparation and experimentation are much more difficult and time consuming. Furthermore, the differences between the predictions of different gradient-dependent models may depend strongly on deformation geometry, with some models performing better in certain geometries and other models better in others. As a consequence, it is difficult to agree upon benchmark experiments. There are obvious limitations to a purely phenomenological approach when not even the basic mathematical structure of the constitutive equations is a matter of consent. An obvious, but far from easy, remedy is to base the constitutive equations in the physical processes that underly plasticity.

I.1.4 Dislocation - based models

A natural approach towards resolving the problems of size dependence and deformation patterning is to formulate constitutive models that explicitly account for the physical processes of dislocation motion which are are at the microscopic origin of plasticity. Length scales in this case enter the formulation in terms of the dislocation spacing, or in terms of some characteristic 'wavelength' of the dislocation pattern. Boundary conditions at surfaces and interfaces reflect the physical mechanisms i.e., the blocking, transmission or even emission of dislocations at the boundaries of the deforming body.

To formulate dislocation-based plasticity models, two main approaches have been pursued so far: Discrete Dislocation Dynamics (DDD) and Continuum Density-based Dislocation Dynamics (CDDD).

I.1.4.1 Discrete Dislocation Dynamics (DDD)

DDD traces the evolution of the dislocation systems on a 'microscopic' scale where discrete dislocations can be resolved - either by investigating the motion of discrete lines, which may be discretized into segments [25, 26] or treated as continuous lines [27–29], or by tracing the evolution of strain [30, 31] or dislocation fields [32, 33] with high enough resolution such that the individual dislocations are visible. Irrespective of the formulation used, this approach has the advantage, but also the drawback, that the complete information about the microscopic stress and deformation state is retained. This has obvious advantages in terms of conceptual simplicity, and equally obvious disadvantages in terms of computational cost. Indeed, because of the huge computational cost there has been, for instance, no large-scale discrete simulation of dislocation cell patterning despite 15 years of dedicated effort. In addition, simulation approaches based on discrete lines fit badly into the traditional conceptual framework of continuum plasticity and to 'interface' them with averaged continuum descriptions of the stress and strain states is a formidable problem of multiscale materials modelling.

I.1.4.2 Continuum Density-based Dislocation Dynamics (CDDD)

CDDD describes the evolution of the dislocation microstructure in terms of continuous field variables for which evolution equations are formulated. Historically this approach has three roots:

- simple internal-variable models as first advocated by Gilman and later elaborated by Kocks, Mecking, and their school (see e.g. [34, 35]). In these, the microstructure is described in terms of internal variables ('dislocation densities') which evolve with strain but do not possess any spatial degrees of freedom (i.e., they do not undergo transport);

- quasi-thermodynamic models which derive the transport dislocations and their spatial organization into cells and clusters from internal energy minimization [36, 37];

- the complex and geometrically rigorous Kröner-type theories of continuous distributions of dislocations [38–41] (for overwiews, see [42, 43]) which, however, were never truly elaborated into a theory of the dynamic evolution of dislocation systems except on the level of discrete dislocation lines [32].

Dislocation transport was introduced into CDDD by Aifantis and co-workers [7, 44–49]. The primary purpose of introducing transport terms was to model dislocation patterning phenomena, in particular the emergence of periodically ordered persistent slip band and matrix patterns in cyclic deformation. Drawing on phenomenological analogies with pattern formation in other reaction-diffusion systems, evolution equations of the reaction-diffusion and reaction-diffusion-transport type were formulated for different dislocation 'species' or 'families' distinguished by their geometrical and dynamical properties (positive vs. negative, mobile vs. immobile dislocations, moving dislocations vs. immobile dipoles). Internal length scales appear in this type of theories in terms of diffusion-like transport terms which have been linked to the cyclic mean free path of dislocations [50] or, more generally, to their characteristic transport length before collisions (dislocation reactions). This approach was later also applied to understand the spatial organization of deformation on macroscopic scales during plastic instabilities where multiplication and diffusion-like propagation of dislocations may lead to the emergence of propagating deformation bands [51–53].

I.1.5 Statistical Approaches

Recently, attempts have been made to go beyond phenomenological evolution equations and to formulate the evolution of dislocation densities within a more rigorous mathematical framework. In particular, Groma, Zaiser and co-workers have addressed the evolution of systems of parallel straight dislocations in terms of concepts borrowed from the statistical mechanics

of interacting many-particle systems, which allow to derive equations of evolution for dislocation density fields from the dynamics of discrete dislocations through systematic averaging procedures.

For systems of straight parallel dislocation lines, Groma, Zaiser and co-workers have developed a formalism to represent both the kinematics and interactions of dislocations in a continuum framework [54]. Averaging the discrete equations of motion of the dislocation lines leads to a hierarchy of equations for many-dislocation densities which is truncated at second order, i.e., the interaction of a dislocation with others in its vicinity is represented in terms of pair correlation functions. Owing to the short-range nature of these correlations [55, 56], the interaction can be approximately described in terms of a density dependent flow stress plus a strain-gradient dependent 'back stress' term, whereas the interactions between distant dislocations are appropriately characterized in terms of a long-range stress field which is a functional of the dislocation density pattern. This approach has been tested against numerous benchmark problems and, in general, yields excellent agreement between 2D discrete simulations and continuum calculations [57, 58].

In 3D, the problem is more complicated since the kinematic description of systems of moving lines (as opposed to point particles in 2D) is not straightforward. Different kinematic formulations have been proposed in the literature [59, 60] while a general analysis which allows to recover these formulations as special cases has been provided by Hochrainer [61]. In the next sections we use Hochrainer's work as a starting point for formulating a density-based theory of the kinematics, dynamics and interactions of systems of directed and connected dislocation segments moving on a single slip system. We then discuss several examples where this is applied to size effects in constrained plastic flow (channel slip, shearing of thin films) and in microbending. Particular attention is devoted to assessing the respective influences of dislocation self-interactions (line tension) and interactions between different dislocations on the size-dependent yielding and hardening behavior. We also use these examples to emphasize the importance of initial and boundary conditions for the evolution of the dislocation system, and their possibly crucial influence on the plastic response of a material. We demonstrate the strength of the approach by comparing with experimental observations as well as the results of 3D dislocation dynamics simulations of microbending experiments.

Chapter I.2
Kinematics and dynamics of dislocation densities

I.2.1 Continuum theories of dislocation systems

I.2.1.1 Classical approach

Crystal plasticity as discussed in the introductory chapter is a continuum theory which, at least superficially, does not account for any kind of material defects. For constructing a dislocation-based theory, one may ask how the existence of dislocations can be mathematically expressed in such a continuum theory. Already many years ago, this was attempted through the notion of incompatibility [43].

We envisage a body undergoing compatible deformations that do not produce discontinuities in the body structure (i.e., no cracking). The mathematical expression for this would be that the corresponding distortion tensor derives from the gradient of a displacement field,

$$\boldsymbol{\beta}^{\mathrm{tot}} = \nabla \boldsymbol{u}^{\mathrm{tot}} \quad or \quad \mathrm{curl}\boldsymbol{\beta}^{\mathrm{tot}} = 0. \tag{I.2.1}$$

Further for small deformations we can adopt a linear decomposition of the total distortion to its elastic and plastic components:

$$\boldsymbol{\beta}^{\mathrm{tot}} = \boldsymbol{\beta} + \boldsymbol{\beta}^{\mathrm{pl}}, \tag{I.2.2}$$

and evidently

$$\mathrm{curl}\boldsymbol{\beta} = -\mathrm{curl}\boldsymbol{\beta}^{\mathrm{pl}}. \tag{I.2.3}$$

Deformation by dislocation motion generally implies discontinuities in the plastic displacement

field (a dislocation can be envisaged as a boundary of a slipped area over which two adjacent lattice planes have been mutually displaced by one Burgers vector). For such discontinuous displacement fields the expression $\mathrm{curl}\boldsymbol{\beta}^{\mathrm{pl}}$ is in general non-zero. Consequentially there is no unique plastic displacement field $\boldsymbol{u}^{\mathrm{pl}}$ for which the compatibility condition given above holds true and thus the compatible deformation results from two incompatible, elastic and plastic, parts. We can then write

$$\mathrm{curl}\boldsymbol{\beta} = -\mathrm{curl}\boldsymbol{\beta}^{\mathrm{pl}} = \boldsymbol{\alpha} \tag{I.2.4}$$

To understand the meaning of $\boldsymbol{\alpha}$ we consider the surface integral

$$\int_S \mathrm{curl}\boldsymbol{\beta} d\boldsymbol{S} = \oint_C \boldsymbol{\beta} d\boldsymbol{x} = \oint_C d\boldsymbol{u} = \boldsymbol{b}_{\mathrm{tot}}, \tag{I.2.5}$$

where S is a surface inside the medium, C the boundary of S, and $\boldsymbol{b}_{\mathrm{tot}}$ the total Burgers vector contained within this boundary. By substitution we see that

$$\int_S \boldsymbol{\alpha} dS = \boldsymbol{b}. \tag{I.2.6}$$

Therefore $\boldsymbol{\alpha}$ describes a Burgers vector density and can be interpreted as a dislocation density tensor. From its definition it follows that $\mathrm{div}\boldsymbol{\alpha} = 0$.

The dislocation density tensor $\boldsymbol{\alpha}(\boldsymbol{r})$ yields a complete description of the dislocation system if the spatial resolution is sufficiently high such that the individual dislocation lines are resolved in detail. If $\boldsymbol{\alpha}$ is understood as an average over many dislocation lines, however, a significant limitation in the above representation is that $\boldsymbol{\alpha}$ measures only the resulting Burgers vector. This means that positive and negative dislocations may cancel to a large degree. For instance, the resulting Burgers vector turns out to be zero if an equal number of positive and negative dislocations pierce through S, irrespective of the fact that their number can be very large. This case is met in simple tensile or shear deformation, where due to symmetry reasons equal numbers of dislocations of both signs are produced. Materials may undergo significant hardening or softening during such deformation processes, which means that the internal mechanical state changes although the macroscopically averaged dislocation density $\boldsymbol{\alpha}$ remains identically zero.

In other cases where strain gradients are present, e.g. bending and torsion, excess dislocations of one sign are created but comparatively the change they bring upon the mechanical state is less than that due to the large amount of simultaneously produced dislocations of both signs.

I.2.1.2 Modified dislocation density measures

The problem addressed above arises from a loss of essential information on the dislocation network and its evolution that occurs as soon as the dislocation density tensor is averaged. One may therefore look for modified dislocation density measures which retain the essential kinematic information about the evolution of the dislocation system. There are four essential elements that such a dislocation kinematic formulation should be able to supply:

- It should above all keep track of the dislocation motions, as dislocation motion is equivalent to plastic straining. For doing so all the crucial variables that can reconstruct the dislocation lines, their activity and their connections need to be retained.
- It should capture the increase of dislocation length associated with the expansion of curved dislocation segments and loops.
- The above two requirements should still be fulfilled after averaging.
- There should be as little redundant information as possible.

Complying with all the above requirements is not an easy task. If we look at the problem from the viewpoint of an assembly of discrete lines, no other information than the spatial line configuration $\boldsymbol{r}(s)$ and the Burgers vector of the individual lines is needed, i.e., we may work with space-dependent discrete densities $\rho(\boldsymbol{r})_i = \int \delta(\boldsymbol{r} - \boldsymbol{r}(s))ds$ where the integral runs over all dislocation lines of Burgers vector $\boldsymbol{b}_i$. However, as soon as we average to define a continuum density $\rho_i(\boldsymbol{r}) = \langle \rho_i(\boldsymbol{r}) \rangle$, we lose relevant kinematic information: The glide motion of a dislocation line segment occurs in its glide plane, in the direction perpendicular to the segment. By averaging we can no longer keep track of the line direction of different segments and thereby of their direction of motion. This problem occurs irrespective of whether we understand the average in the sense of spatial coarse graining or ensemble averaging. To keep track of the directions of motion we have to introduce as another phase-space variable the angle ϕ enclosed, in the glide plane, between the line direction and the Burgers vector of a segment. The discrete density is now $\rho(\boldsymbol{r}, \phi) = \int \delta(\boldsymbol{r} - \boldsymbol{r}(s))\delta(\phi - \phi(s))ds$, and the averaged density function

$\rho(\boldsymbol{r}, \phi)$ allows us to consider the dislocation fluxes separately for each orientation ϕ. (Alternatively, one may think of defining the director angle $\phi = \phi(\boldsymbol{r})$ as a space-dependent field as done by Sedlacek et al. [60]. This works well if dislocations form bundles of similar orientation, but leads to trouble as soon as segments of multiple orientations appear within the same mesoscopic volume element, such that a director field can no longer defined.) The classical dislocation density tensor is recovered from the angle-dependent dislocation density measure by multiplying $\rho(\boldsymbol{r}, \phi)$ with the outer product of the Burgers vector $\boldsymbol{b}$ and the unit tangent vector $\boldsymbol{e}_{\mathrm{t}}(\phi)$, and integrating over all ϕ:

$$\boldsymbol{\alpha} = \int \rho(\boldsymbol{r}, \phi) \boldsymbol{b} \otimes \boldsymbol{e}_{\mathrm{t}}(\phi) d\phi. \tag{I.2.7}$$

The angle-dependent dislocation density measure allows us to keep track of the directions of motion of the dislocations. However, another problem arises from the fact that the continuum density function $\rho(\boldsymbol{r}, \phi)$ does not distinguish between dislocations of different curvature. This is easily seen by considering distributions of circular loops with identical radius R, randomly located centers of volume density ρ_0/R, and line length per unit volume ρ_0. Irrespective of R, all such distributions are characterized by the same average density function $\rho(\boldsymbol{r}, \phi) = \rho_0/2\pi$, even in the limit $R \to \infty$ which corresponds to a homogeneous pattern of straight lines with random orientation. Assume now the loops expand at an average velocity υ. This leads to a R-dependent change in the average dislocation density given by $d\rho/dt = \rho\upsilon/2\pi R$. Since the kinematics depend on the radius of curvature, one has to keep track of this variable or distinguish expanding from non-expanding configurations in some other way. Hence, we may again expand our phase space by including the local curvature $k = 1/R$ (or the radius of curvature R) as another independent variable, or – with the same caveat as above for the line direction – we may define the curvature $k(\boldsymbol{r})$ as a space dependent field. Finally, the evolution of curvature may depend on the change of curvature along the dislocation line, i.e., on higher-order curvature, and so on [62].

I.2.2 Kinematics and dynamics of the dislocation system

In the following we adopt the kinematic framework developed by Hochrainer [61–63] and briefly sketched above, i.e.we use a dislocation density measure ρ which is defined on a configuration space which consists of the positions and orientations of dislocation segments, and

treat the dislocation line curvature k as an independent field. We specify our formulation to dislocations moving by glide on a given slip system, such that the dislocation orientation is fully characterized by the angle ϕ between the dislocation line direction and the Burgers vector. (Situations with dislocations moving on multiple slip systems can be treated straightforwardly by defining separate measures ρ^i for each slip system i; in the following we drop the subscript i for the simplicity of presentation.)

For a given orientation, there exists a set of orthogonal unit vectors $\boldsymbol{n}$ in the direction of the glide plane normal, $\boldsymbol{e}_{\mathrm{t}}(\phi)$ in the direction tangential to the dislocation line, and $\boldsymbol{e}_{\mathrm{g}}(\phi) = \boldsymbol{n} \times \boldsymbol{e}_{\mathrm{t}}(\phi)$ in the dislocation glide direction. Assuming that dislocations move by glide only, the evolution of the density measure ρ is then given by the continuity equation (cf. [62])

$$\partial_t \rho = -\partial_\phi [\rho v_\phi] - \nabla \cdot [\rho \boldsymbol{v}] + \rho v k \ . \tag{I.2.8}$$

Here, $\boldsymbol{v} = \boldsymbol{e}_{\mathrm{g}} v$ is the vectorial and v the pseudo-scalar velocity of the dislocation segments, and the rotation velocity of the dislocation lines is given by

$$v_\phi = \boldsymbol{e}_{\mathrm{t}} \cdot \nabla v + k \partial_\phi [v] \ . \tag{I.2.9}$$

It is noted that the conservation law given by Eq.(I.2.8) is a generalization of previously formulated continuity equations for straight parallel dislocations (e.g., [5, 54]). The curvature-dependent term contained in the above continuity equation accounts for the expansion or shrinkage of dislocation loops as well as, in an implicit manner, for dislocation reaction (generation / annihilation) terms as introduced e.g. by Aifantis [5, 20, 50]. The dislocation curvature is understood as an additional field variable. The theory is exact if all dislocations of a given orientation in a given volume element have the same curvature [62]. The local values of the curvature field pertaining to a given orientation then obey the differential equation

$$\partial_t k = -k^2 v + k(\boldsymbol{e}_{\mathrm{g}} \cdot \nabla v) - \boldsymbol{e}_{\mathrm{t}} \cdot \nabla [v_\phi] - k \partial_\phi [v_\phi] - \boldsymbol{v} \cdot \nabla [k] - v_\phi \partial_\phi [k] \ . \tag{I.2.10}$$

The equations for the curvature field may be solved alongside with those for the dislocation density measure. Alternatively, in the present work we use later on a line tension approximation to evaluate the dislocation behavior under quasi-static conditions. In this approximation, the

curvature ceases to be an independent field and simply becomes a function of the shear stress acting on the dislocation, and thereby a functional of the dislocation density measure.

The plastic strain rate can be recovered from the dislocation density measure as the modulus of the total dislocation flux times the Burgers vector modulus:

$$\partial_t \gamma(\boldsymbol{r}) = \int (\rho b v)\, \mathrm{d}\phi \,, \tag{I.2.11}$$

where the integral is extended over all orientations $\phi \in [0, 2\pi]$. This relation may be integrated alongside with the evolution of the dislocation density measure to yield the plastic strain field at a given moment in time.

To pass from dislocation kinematics to dynamics, we have to specify the dislocation velocity v. We neglect dislocation inertia and assume that the dislocation velocity is controlled by drag forces. In this case, the velocity becomes a function of the local stress $\tau(\boldsymbol{r})$ acting on a dislocation at $\boldsymbol{r}$,

$$\frac{v}{B(\phi)} = \tau(\boldsymbol{r}) b \,, \tag{I.2.12}$$

where B is the (in general direction-dependent) dislocation mobility. The key problem is now how to evaluate the stress $\tau(\boldsymbol{r})$ which, in order to obtain a closed theory of plastic flow, must be expressed as a functional of the plastic strain and/or the dislocation density measure.

I.2.3 Internal stresses and dislocation interactions

As already mentioned, by integrating Eq. (I.2.11), we can obtain the plastic strain field at a given moment in time. It is then a standard problem of continuum mechanics to determine the corresponding stress field for a given set of boundary conditions. In the following we use a terminology where we split this stress field into a field τ_{ext} ('external stress') that is due to the tractions applied from outside to the deforming body, and a mesoscopic internal-stress field τ_{mf} which arises from the in general inhomogeneous strain field $\gamma(\boldsymbol{r})$ [1]. In a small-strain

[1] The notion of a 'mesoscopic' internal-stress field is motivated by the fact that this stress field is defined on the same scale as the dislocation density measure ρ and the plastic strain γ. If ρ and γ are considered as smooth averages over volume elements containing many dislocations, the same holds for τ_{mf}.

approximation (and only then) the two contributions are additive because of the linearity of the problem. In an infinite crystal, the mesoscopic stress τ_{mf} can be expressed as a functional of the dislocation density pattern via

$$\tau_{\mathrm{mf}}(\boldsymbol{r}) = \int_V \rho(\boldsymbol{r}', \phi')\tau_{\mathrm{seg}}(\boldsymbol{r} - \boldsymbol{r}', \phi')\mathrm{d}\boldsymbol{r}'\mathrm{d}\phi' \ , \tag{I.2.13}$$

where τ_{seg} is the shear stress created at $\boldsymbol{r}$ by a segment of orientation ϕ' located at $\boldsymbol{r}'$. Explicit expressions for segment stresses have been given by Devincre and Condat [25]. We note, however, that instead of evaluating the expression given by Eq. (I.2.13) it is often more convenient to solve the elastic problem directly; in cases where surface boundary conditions are imposed this may indeed be the only feasible method of solution, and such a scheme is also adopted in the subsequent examples.

The mesoscopic stress field, Eq. (I.2.13), varies on the same length scale as the dislocation density pattern described by the dislocation density measure ρ. In principle, ρ can be considered with a spatial resolution sufficient such that individual dislocations can be resolved; in this case the complete information about the internal stresses is contained in Eq. (I.2.13), and our theory is just a complicated way of expressing the evolution of a discrete dislocation system. However, the main point of a density-based description is to describe dislocation dynamics on a mesoscopic scale where the 'elementary size' of a volume element may be above the mean dislocation spacing. In this case, any fluctuations of the stress field on the scale of individual dislocations are averaged out. A straightforward proposition might be to describe, within the framework of such a mesoscopic theory, the local stress state in terms of $\tau(\boldsymbol{r}) = \tau_{\mathrm{ext}} + \tau_{\mathrm{mf}}$ and to evaluate τ_{mf} – which in this case has the character of a mean stress field – from the (mesoscopically averaged) dislocation density measure, or the (also mesoscopically averaged) strain field. This amounts to a mean-field dislocation theory of plasticity as discussed by Hochrainer et al. [62], and also (in different versions) by other authors in the past (e.g. Aifantis [51]).

It is, however, emphasized that such a mean-field theory, which from a statistical viewpoint corresponds to neglecting any correlations between dislocation segments and/or dislocation lines, in general does *not* provide a full description of the stresses acting locally *on the dislocations*. This can be seen immediately by considering an infinite body deforming (on mesoscopic scales) in homogeneous simple shear. In this case, the mesoscopic shear strain is a constant, and accordingly the mesoscopic stress τ_{mf} is zero. Since in a mean-field theory τ_{mf} is the only

term which accounts for dislocation interactions, such a theory predicts for mesoscopically homogeneous dislocation arrangements that, irrespective of the dislocation arrangement within the elementary volume, the flow stress is zero unless obstacles other than dislocations are introduced in some way into the stress-velocity law. It can be seen from dislocation dynamics simulations but also from experiment (consider hardening Stage I of pure fcc metals) that this assertion is incorrect.

A straightforward extension of the mean-field approach, which is particularly well-adapted to the formulation used in the present work, is to include into the theory stresses associated with the large-scale curvature of the dislocations. In a line-tension approximation, such stresses can be expressed as $\tau_{\mathrm{lt}} = Tk/b$ where $T \approx Gb^2$ is the dislocation line tension. Note, however, that k in the present formulation is considered as a mesoscopic field, and therefore τ_{lt} does not account for stresses due to fluctuations of the lineshape on the 'microscopic' scale below the average dislocation spacing. Such stresses, which arise from bowing out of dislocations between junctions and other localized obstacles, form in a mesoscopic description part of the flow stress. This is discussed in the next paragraph.

In general, dislocations during plastic flow arrange themselves in such a way as to mutually obstruct their motion. These 'jammed' dislocation configurations [64] may consist of dislocation dipoles and multipoles, or of dislocation junctions and locks. In either case, such configurations have an extension of one or at maximum a few dislocation spacings, i.e. they pertain to a 'microscopic' length scale *below* the averaging scale of a mesoscopic theory. Formally, such configurations and the associated 'microscopic' stresses can be included into a mesoscopic theory by considering dislocation-dislocation correlation functions. This has been discussed for 2D dislocation systems (systems of parallel edge dislocations) by Zaiser, Groma and co-workers [54, 55], and a similar procedure for 3D dislocation systems was outlined in [63, 65]. The basic idea is that dislocation pair correlations are short-ranged with a range of the order of one dislocation spacing. Therefore, the dislocation interactions which are associated with them can, on a mesoscopic scale, be expressed as *local* functions of the averaged dislocation densities and their gradients (local density approximation). The short-range nature of the correlation functions allows for a systematic expansion into dislocation density gradients of increasing order. The assertion that dislocation pair correlations are short-ranged has recently been confirmed for systems of straight parallel dislocations in a study by Groma et al. [56]. They derive an analytical expression for the pair correlation function and demonstrate quantitative agreement

with discrete dislocation dynamics simulations.

In the following we shall not analyse dislocation-dislocation correlations in detail (for such an analysis, see the papers of Groma and co-workers [56] and of El-Azab and co-workers [66]). Rather, we adopt a phenomenological approach where we describe the 'microscopic' stress state in terms of a dislocation-density dependent friction stress τ_{f} and a 'back stress' τ_{b} which depends on the dislocation density gradient (see also the introduction of similar expressions in [67]). These are assumed in the form

$$\tau_{\mathrm{f}} = \alpha G b \sqrt{\rho_{\mathrm{t}}} \ , \ \tau_{\mathrm{b}} = \frac{DGb}{\rho_{\mathrm{t}}} \int (\boldsymbol{e}_{\mathrm{g}} \cdot \nabla \rho) \mathrm{d}\phi \ . \tag{I.2.14}$$

Here $\rho_{\mathrm{t}} = \int \rho \mathrm{d}\phi$ denotes the total dislocation density in a given point and G is the shear modulus of the material. The constants α and D may in general depend on the line orientation ϕ and/or on the 'composition' of the dislocation arrangement (the distribution of dislocations over the different directions). However, the basic structure of the 'flow stress' and 'friction stress' terms is dictated by scaling properties as discussed in [54, 55] for two- and in [63, 65] for three-dimensional dislocation systems. In particular, for a 2D dislocation arrangement consisting of straight parallel edge dislocations these terms reduce to expressions derived by Groma and co-workers using both statistical averaging techniques [54] and extremal principles ([56]). In passing, we note that the 'flow stress' expression is simply Taylor's well-established relation for the dissipative friction stress that has to be overcome when deforming a dislocation arrangement, whereas the 'back stress' is a 3D generalization of the 2D 'pile-up stress' derived by Groma and Zaiser, which has been proven in numerous studies of size-dependent plasticity to yield a correct continuum representation of short-range dislocation repulsion in 2D dislocation dynamics and the associated size effects.

In the following we use Eq. (I.2.14) with isotropic (direction-independent) coefficients α and D to describe the 'microscopic' stress state and combine this with a continuum approach to calculate the external and mesoscopic internal stresses. Before applying the formalism to concrete examples, however, it is convenient to re-formulate the kinetic equations in a form that is suitable for an analytic treatment of the simple example problems we are going to discuss.

I.2.4 Edge-Screw Representation

A practical hindrance to numerical implementation of the continuum dislocation dynamics formulated above is that a reasonable resolution in angular space requires a large number of dislocation fields $\rho(\boldsymbol{r}, \phi_i)$. Since this obviously increases the numerical cost, one may ask whether it is possible to use only a coarse discretization, such as the edge-screw model proposed by Arsenlis et al. [68]. However, a 'naive' edge-screw approach which allows for only 4 values of ϕ ($\phi \in [0, \pi/2, \pi, 3\pi/2]$) is problematic since line-tension effects and dislocation multiplication are badly represented (one effectively deals with rectangular dislocation loops). None of the subsequent examples can be adequately treated in this too-simplistic approximation.

We therefore use a different approach where we start out from the kinematic formulation outlined in Section I.2.1, but then represent the dislocation orientation in terms of the edge and screw components of mixed dislocation segments. We first consider the density measure ρ on a 'microscopic' scale where individual dislocation lines can be resolved, and associate it with the screw and edge segment densities R_s and R_e. On the microscopic scale, the screw, edge, and total densities fulfil the geometrical relation $\rho^2 = R_\mathrm{s}^2 + R_\mathrm{e}^2$, and the local dislocation orientation is $\tan\phi = R_\mathrm{e}/R_\mathrm{s}$. Assuming that the Burgers vector points in the x direction and considering a direction-independent mobility B, we obtain from Eqs. (I.2.8), (I.2.9) the following equations of evolution for the screw and edge densities (for details of the derivation see Appendix A):

$$\partial_t R_\mathrm{e} = \left[-\frac{R_\mathrm{e}^2}{\rho^2}\partial_x(\rho v) + \frac{R_\mathrm{e}R_\mathrm{s}}{\rho^2}\partial_y(\rho v)\right] + R_\mathrm{s}\left[\frac{R_\mathrm{s}}{\rho}\partial_x v + \frac{R_\mathrm{e}}{\rho}\partial_y v\right] + R_\mathrm{e} v k \;, \qquad \text{(I.2.15)}$$

$$\partial_t R_\mathrm{s} = \left[-\frac{R_\mathrm{e}R_\mathrm{s}}{\rho^2}\partial_x(\rho v) + \frac{R_\mathrm{s}^2}{\rho^2}\partial_y(\rho v)\right] - R_\mathrm{e}\left[\frac{R_\mathrm{s}}{\rho}\partial_x v + \frac{R_\mathrm{e}}{\rho}\partial_y v\right] + R_\mathrm{s} v k \;. \qquad \text{(I.2.16)}$$

It is important to note that in this model edge and screw segments move together in the glide direction determined by the local 'composition' of the dislocation line and not separately in 'edge' and 'screw' directions.

In the following we are interested in a statistical description of the dislocation system. We therefore proceed to average these equations. We introduce the notations $\kappa_\mathrm{s} := \langle R_\mathrm{s}\rangle, \kappa_\mathrm{e} := \langle R_\mathrm{e}\rangle, \rho := \langle\rho\rangle, \rho_\mathrm{s}^2 := \langle R_\mathrm{s}^2\rangle, \rho_\mathrm{e}^2 := \langle R_\mathrm{e}^2\rangle$ and $\rho_\mathrm{se}^2 := \langle R_\mathrm{s}R_\mathrm{e}\rangle$, where the averages are understood as both spatial and directional. We obtain

$$\partial_t \kappa_\mathrm{e} = \left[-\frac{\rho_\mathrm{e}^2}{\rho^2} \partial_x (\rho v) + \frac{\rho_\mathrm{se}^2}{\rho^2} \partial_y (\rho v) \right] + \rho \left[\frac{\rho_\mathrm{s}^2}{\rho^2} \partial_x v + \frac{\rho_\mathrm{se}^2}{\rho^2} \partial_y v \right] + \kappa_\mathrm{e} v k \ , \tag{I.2.17}$$

$$\partial_t \kappa_\mathrm{s} = \left[-\frac{\rho_\mathrm{se}^2}{\rho^2} \partial_x (\rho v) + \frac{\rho_\mathrm{s}^2}{\rho^2} \partial_y (\rho v) \right] - \rho \left[\frac{\rho_\mathrm{se}^2}{\rho^2} \partial_x v + \frac{\rho_\mathrm{e}^2}{\rho^2} \partial_y v \right] + \kappa_\mathrm{s} v k \tag{I.2.18}$$

for the average sign densities. In deriving these equations we have used the relations $\langle R_\mathrm{e}^2/\rho \rangle = \langle R_\mathrm{e}^2 \rangle \langle \rho \rangle / \langle \rho^2 \rangle$ and similarly for R_s, which are proven in the Appendix A. As we assumed that the dislocation velocity is independent of the segment orientation, there is no correlation between $(R_\mathrm{e}/\rho), (R_\mathrm{s}/\rho), (R_\mathrm{e}^2/\rho^2)$, or (R_s^2/ρ^2), and v. We note that, for a system of parallel edge dislocations where $R_\mathrm{s} = 0$ and hence $\rho_\mathrm{se} = \rho_\mathrm{s}^2 = 0, \rho_\mathrm{e}^2 = \rho^2$, Eq. (I.2.17) reduces to the simple relation

$$\partial_t \kappa_\mathrm{e} = -\partial_x (\rho v) \ , \tag{I.2.19}$$

which is one of the two equations describing the kinetics of such a system as discussed by Groma et al. [54]. Comparison with that work also demonstrates that a closed description requires a second equation for the total density ρ (or, equivalently, the density square ρ^2). In the edge-screw case, we need in general three additional equations as Eqs. (I.2.18) and (I.2.17) contain the product densities ρ_s^2, ρ_e^2 and ρ_se^2. For these, evolution equations can be obtained by averaging the evolution of the products $R_\mathrm{s}^2, R_\mathrm{e}^2$, and $R_\mathrm{s} R_\mathrm{e}$. In the examples discussed in the present work, however, it is in fact sufficient to consider Eq. (I.2.17) only, as will become evident in the following.

Chapter I.3
Application to constrained plastic flow

In the following we consider some examples of plane-strain deformation of thin films under different boundary conditions, *viz,* the shearing of a thin film tethered to a non-deformable substrate and containing either one single or two symmetrically inclined slip systems, and the bending of a free-standing thin film containing two symmetrically inclined slip systems. The respective deformation geometries are illustrated in Figures I.3.1 and I.3.2.

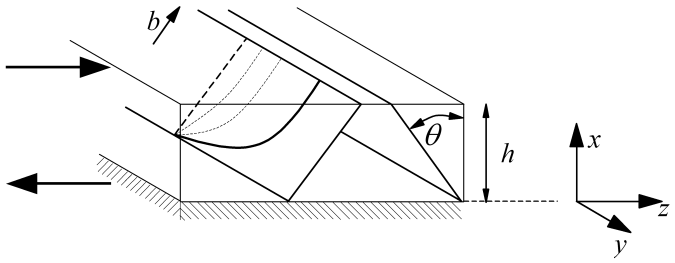

Figure I.3.1: *Illustration of the free surface thin film shearing case.*

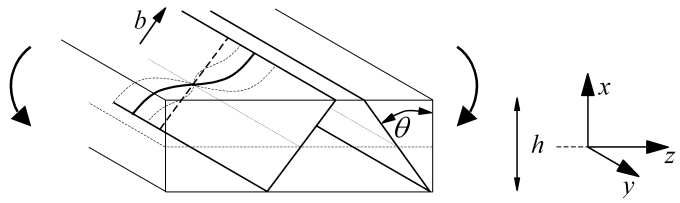

Figure I.3.2: *Illustration of the free standing thin film bending case.*

Instead of the slip system specific coordinate system used to formulate the dislocation dynamics equations, we use in the following a Cartesian coordinate system where the x axis is normal

to the plane of the film. We consider a homogeneous thin film of thickness h with infinite extension in the y and z directions. The Burgers vectors of the active slip system(s) are contained in the xz plane and form an angle θ with the x direction (two angles $\pm\theta$ in case of symmetrical double slip). The whole problem can be easily identified as a plane strain one. Since all variables depend on the x coordinate only (the problem is homogeneous in y and z), the formulation effectively becomes one-dimensional.

The elastic-plastic deformation problem can be separated into two sub-problems. We first assume a generic plastic strain distribution and solve the corresponding elastic boundary value problem. This gives us the stress state corresponding to a given plastic strain distribution and given externally applied tractions. In a second step, we deduce the evolution of the plastic strain and the dislocation distribution from the dislocation dynamics framework defined in the previous chapter.

I.3.1 Solution of the elastic problem

To find the elastic solutions required in the examples we assume an isotropic linear-elastic solid and use a small-strain approximation. The stress is related to the elastic and plastic strain tensors by $\boldsymbol{\sigma} = \boldsymbol{C}(\boldsymbol{\varepsilon}^{\mathrm{tot}} - \boldsymbol{\varepsilon}^{\mathrm{pl}})$. The total strain tensor $\boldsymbol{\varepsilon}^{\mathrm{tot}}$ is the symmetrical part of the total distortion tensor $\boldsymbol{\beta}^{\mathrm{tot}} = \nabla \boldsymbol{u}^{\mathrm{tot}}$ where $\boldsymbol{u}^{\mathrm{tot}} = [u_x, u_y, u_z]$ is the displacement field, and $\boldsymbol{\varepsilon}^{\mathrm{pl}}$ is the symmetrical part of the plastic distortion tensor $\boldsymbol{\beta}^{\mathrm{pl}}$. The latter is determined from the crystal plasticity relation $\boldsymbol{\beta}^{\mathrm{pl}} = \sum_i \gamma_i \boldsymbol{e}_{\mathrm{g}}^i \otimes \boldsymbol{n}^i$ (the sum runs over all active slip systems).

Using the coordinate system in Figures I.3.1 and I.3.2, we find that the slip and slip plane normal vectors in the case of symmetrical double slip are given by

$$\boldsymbol{e}_{\mathrm{g}}^1 = \begin{bmatrix} \cos\theta & 0 & \sin\theta \end{bmatrix}, \quad \boldsymbol{e}_{\mathrm{g}}^2 = \begin{bmatrix} \cos\theta & 0 & -\sin\theta \end{bmatrix},$$

$$\boldsymbol{n}^1 = \begin{bmatrix} \sin\theta & 0 & -\cos\theta \end{bmatrix}, \quad \boldsymbol{n}^2 = \begin{bmatrix} \sin\theta & 0 & \cos\theta \end{bmatrix}, \tag{I.3.1}$$

and the elastic strain tensor follows as

$$(\boldsymbol{\varepsilon}^{\mathrm{tot}} - \boldsymbol{\varepsilon}^{\mathrm{pl}}) = \frac{1}{2}\begin{bmatrix} 2u_x' - (\gamma_1+\gamma_2)\sin 2\theta & 0 & u_z' + (\gamma_1-\gamma_2)\cos 2\theta \\ 0 & 0 & 0 \\ u_z' + (\gamma_1-\gamma_2)\cos 2\theta & 0 & (\gamma_1+\gamma_2)\sin 2\theta \end{bmatrix} . \tag{I.3.2}$$

The prime denotes derivative with respect to the x coordinate (all other derivatives vanish). The resolved shear stresses for each slip system are obtained via $\tau^i(\boldsymbol{r}) = \boldsymbol{n}^i \cdot [\boldsymbol{\sigma}\boldsymbol{e}^i_{\mathrm{g}}]$, and the case of single slip is simply recovered by setting $\gamma_2 = 0$.

Due to the superposition principle, the stress state can be considered as a superposition of a 'mesoscopic' internal stress related to the shear strain fields γ_1 and γ_2 on the two active slip systems ($\gamma_2 = 0$ for single slip), which is evaluated for a body with traction-free surfaces, and an 'external stress' which corresponds to the stress state of the same body under the prescribed boundary conditions but without plastic distortions. Both fields separately fulfill the stress equilibrium condition $\mathrm{div}\boldsymbol{\sigma} = 0$. We first determine the internal stresses. The shear stress for each slip plane for both of the states discussed is given by

$$\tau^1 = \frac{\sigma_{xx} - \sigma_{zz}}{2}\sin 2\theta - \sigma_{xz}\cos 2\theta \, , \tag{I.3.3}$$

$$\tau^2 = \frac{\sigma_{xx} - \sigma_{zz}}{2}\sin 2\theta + \sigma_{xz}\cos 2\theta \, . \tag{I.3.4}$$

Use of equilibrium conditions $\partial_x\sigma_{xz} = 0$, $\partial_x\sigma_{xx} = 0$ together with the traction-free requirement provides us with $\sigma_{xz} = 0$ and $\sigma_{xx} = 0$. Thus for shear deformation in single slip the shear stress reduces to $\tau = -\sigma_{zz}\sin 2\theta/2$. By replacements from Hooke's law

$$\begin{aligned} \sigma_{xx} &= \frac{2G(1-\nu)}{(1-2\nu)}(\varepsilon_{xx} + \frac{\nu}{(1-\nu)}\varepsilon_{zz}) \, , \\ \sigma_{zz} &= \frac{2G(1-\nu)}{(1-2\nu)}(\varepsilon_{zz} + \frac{\nu}{(1-\nu)}\varepsilon_{xx}) \, , \\ \sigma_{xz} &= 2G\varepsilon_{xz} \, . \end{aligned} \tag{I.3.5}$$

we eventually obtain

$$\tau_{\rm mf} = -\frac{\sin^2 2\theta}{2(1-\nu)} G(\gamma_1 + \gamma_2) \; . \tag{I.3.6}$$

For shear deformation in symmetrical double slip, $\gamma_1 = -\gamma_2$ and, hence, $\tau_{\rm mf} = 0$. For bending in symmetrical double slip, on the other hand, $\gamma_1 = \gamma_2 =: \gamma/2$, and we similarly find for either of the slip systems

$$\tau_{\rm mf} = -\frac{\sin^2 2\theta}{2(1-\nu)} G\gamma \; . \tag{I.3.7}$$

In the most general case of arbitrary deformations on two generically inclined slip systems, finally, one obtains

$$\begin{aligned} \tau^1_{\rm mf} &= -\frac{\gamma_1 \sin^2 2\theta_1 + \gamma_2 \sin 2\theta_1 \sin 2\theta_2}{2(1-\nu)} G \; , \\ \tau^2_{\rm mf} &= -\frac{\gamma_2 \sin^2 2\theta_2 + \gamma_1 \sin 2\theta_1 \sin 2\theta_2}{2(1-\nu)} G \; . \end{aligned} \tag{I.3.8}$$

Stresses due to externally applied tractions superimpose on the internal stresses evaluated above. These stresses can be evaluated for a plastically undeformed body and then simply added to the internal stresses. For shearing, we assume that a constant traction σ_{xz} is applied to the free surface of the film and all other surface stress components are zero. The conditions $\partial_x \sigma_{xz} = 0$ and $\partial_x \sigma_{xx} = 0$ then simply yield a constant external stress

$$\tau_{\rm ext} = -\sigma_{xz} \cos 2\theta \; . \tag{I.3.9}$$

For bending the imposed loading consists of a pair of moments as illustrated in Figure I.3.2 and zero surface tractions. For geometrical reasons the elastic strain distribution over the thickness follows a linear law (keep in mind that, in evaluating the 'external' stress, we envisage a body free of plastic distortions).

$$\varepsilon_{zz} = \frac{x}{R} \; , \tag{I.3.10}$$

where R is an arbitrary constant. From the one-dimensional nature of the problem, the boundary conditions at the upper and lower surfaces of the film (the surfaces are traction-free) and the equilibrium conditions $\partial_x \sigma_{xx} = 0$ and $\partial_x \sigma_{xz} = 0$, it follows that $\sigma_{xz} = \sigma_{xx} = 0$. Thus the only non-zero in-plane stress component is σ_{zz}. This evaluates (cf. Eq.(I.3.5)) as

$$\sigma_{zz} = \frac{2G}{1-\nu}\varepsilon_{zz} = \frac{2G}{1-\nu}\frac{x}{R} \,. \tag{I.3.11}$$

We can further relate the constant R to the externally applied moment M by the simple relation $M = 2\int_0^{h/2} \sigma_{zz} x dx$. Note that working on an infinitely extended body M is understood as the moment per unit length. Substitution in Eqs. (I.3.3),(I.3.4) results in

$$\tau_{\text{ext}} = -\frac{\sin 2\theta}{1-\nu} G \frac{x}{R} = -6 \sin 2\theta \frac{Mx}{h^3} \,. \tag{I.3.12}$$

This concludes our discussion of the elastic problems, which for the simple geometries envisaged is straightforward. The much more complicated task of evaluating the plastic deformation state is addressed in the next section.

I.3.2 Constitutive equations and solutions

The plastic problem is solved by determining the evolution of the dislocation system. To this end, initial and boundary conditions need to be specified. As an initial condition, we will assume in all cases that, on each active slip system, equal densities $\rho_0/2$ of screw dislocations of both signs, but no edge segments, are present. Owing to the plane-strain geometry, the density of screw segments is conserved for this initial condition. Consequently, we may use in Eq. (I.2.17) the closure approximation $\rho_{\text{e}}^2 = \kappa_{\text{e}}^2$ and $\rho_{\text{s}}^2 = \rho_0^2$, while ρ_{se}^2 and κ_{s} are zero at all times. Furthermore we note that, owing to the symmetrical configuration of the slip systems, the dislocation densities on both systems are equal such that in the following only one of them needs to be considered.

On free surfaces, dislocation densities must fulfil the boundary condition $\kappa_{\text{e}}(x) = 0$ [69]. For the interface with the elastic substrate, the requirement of zero dislocation flux through the interface ($\dot{\gamma}(0) = 0$ for all times) imposes the boundary condition $\gamma(0) = 0$ for the plastic strain.

For the chosen geometry, the variable $\kappa_{\rm e}$, as all other variables, is a function of the x coordinate only. This leads to the equation

$$\partial_t \kappa_{\rm e} = -\cos\theta \frac{\kappa_{\rm e}^2}{\rho^2}\partial_x(\rho v) + \cos\theta\rho\frac{\rho_0^2}{\rho^2}\partial_x v + \kappa_{\rm e} v k \;, \tag{I.3.13}$$

where $\rho^2 = \rho_0^2 + \kappa_{\rm e}^2$ and the projection term $\cos\theta$ stems from the fact that the x coordinate now refers to the film normal direction instead of the slip direction as in Eq. (I.2.17). We further note that, for the plane-strain configurations under consideration, $\kappa_{\rm e} = -\cos\theta(1/b)\partial_x\gamma$. In view of the relationship $\dot\gamma = \rho b v$ between the shear strain rate and the dislocation flux, this leads to

$$\frac{\rho_0^2}{\rho^2}\partial_t \kappa_{\rm e} = \cos\theta\rho\frac{\rho_0^2}{\rho^2}\partial_x v + \kappa_{\rm e} v k \;, \tag{I.3.14}$$

The dynamic formulation is completed by specifying how the pseudo-scalar dislocation velocity v relates to the local stress. As stated above, we use a linear stress-velocity relationship with a direction-independent dislocation mobility B. The local stress is considered as a sum of four contributions: (i) the mesoscopic stress $\tau(\boldsymbol{r})$ which derives from solving the elastic problem in a continuum setting using the strain field $\gamma(\boldsymbol{r})$ (see previous section). For the plane-strain geometries and initial conditions as specified above, this strain field can be simply obtained from the density $\kappa_{\rm e}$ and the boundary conditions, since $\kappa_{\rm e} = -\cos\theta(1/b)\partial_x\gamma$; (ii) the line-tension stress Tk/b; (iii) the flow stress $\tau_{\rm f}$. In the present situation this is related to interactions with forest dislocations, as well as interactions between screw (but not edge) segments of opposite signs. Since both the density of screw dislocations and the planar density of forest dislocations intersecting the glide plane are conserved, $\tau_{\rm f} = \alpha G b\sqrt{\rho_0}$ is considered constant (a similar approximation of constant flow stress was made in [70, 71]); (iv) the back stress $\tau_{\rm b}$, which from Eq. (I.2.14) is evaluated as

$$\tau_{\rm b} = \cos\theta\frac{DGb}{\rho^2}\kappa_{\rm e}\partial_x\rho \;, \tag{I.3.15}$$

where we have used that the glide vectors of both dislocation orientations that may occur at a given point have the same x component and the system is homogeneous in the y direction.

Since the flow stress has the character of a friction stress, whereas the other stresses are conser-

vative in nature and may recover upon unloading, it is convenient to define the local stress as $\tau_{\rm loc} = \tau(\boldsymbol{r}) - \tau_{\rm b} - Tk/b$. The dislocation velocity is then given by

$$\frac{1}{bB}v = \begin{cases} \tau_{\rm loc} - \tau_{\rm f} & , \quad \tau_{\rm loc} > \tau_{\rm f} \ , \\ \tau_{\rm loc} + \tau_{\rm f} & , \quad \tau_{\rm loc} < -\tau_{\rm f} \ , \\ 0 \qquad \text{otherwise} \ . \end{cases} \tag{I.3.16}$$

In the following we focus on the quasi-static limit $B \to \infty$, which gives in general a good representation of the situation in weakly rate-dependent fcc crystals. In this case, we find that

$$\begin{aligned} k &= \frac{(\tau(\boldsymbol{r}) - \tau_{\rm f})b}{T} - \cos\theta \frac{DGb^2}{T}\frac{\kappa_{\rm e}}{\rho^2}\partial_x \rho \quad , \quad \tau_{\rm loc} > 0 \ , \\ k &= \frac{(\tau(\boldsymbol{r}) + \tau_{\rm f})b}{T} - \cos\theta \frac{DGb^2}{T}\frac{\kappa_{\rm e}}{\rho^2}\partial_x \rho \quad , \quad \tau_{\rm loc} < 0 \ . \end{aligned} \tag{I.3.17}$$

In the quasi-static limit, equation (I.3.14) reduces to a balance equation between segment multiplication and segment rotation terms:

$$0 = \cos\theta \frac{\rho_0^2}{\rho}\partial_x v + \kappa_{\rm e} v k \ , \tag{I.3.18}$$

where $v = {\rm const}/\rho$. Combining Eqs. (I.3.17) and (I.3.18) we arrive at the differential equation

$$\cos\theta \frac{\rho_0^2 + D\kappa_{\rm e}^2}{\rho^2}\partial_x \rho = \frac{\kappa_{\rm e}}{Gb}(\tau(\boldsymbol{r}) - \tau_{\rm f}) \ . \tag{I.3.19}$$

In the following, it is convenient to use non-dimensional variables defined by $\tilde{x} = x\sqrt{\rho_0}$ where $1/\sqrt{\rho_0}$ is the characteristic length of the dislocation system, $\tilde{\kappa_{\rm e}} = \kappa_{\rm e}/\rho_0$, $\tilde{\rho} = \rho/\rho_0$, and $\tilde{\tau} = \tau/Gb\sqrt{\rho_0}$. This gives the nondimensional equation

$$\cos\theta \frac{1 + D\tilde{\kappa_{\rm e}}^2}{\tilde{\rho}^2}\partial_{\tilde{x}}\tilde{\rho} = \tilde{\kappa_{\rm e}}(\tilde{\tau}(\boldsymbol{r}) - \alpha) \ . \tag{I.3.20}$$

From now on we will always refer to Equation (I.3.20) for describing the dislocation density pattern. Accordingly, in the following all variables are understood as scaled, and tildes are

omitted.

I.3.3 Shearing of a thin film on an elastic substrate

Using the continuum dislocation representation formulated above, we examine the size-dependent deformation behavior of this system separately in single and symmetrical double slip, and investigate similarities and differences with previous theoretical approaches. It may be noted that the problem under consideration is equivalent to the shear deformation of a constrained channel with elastic walls on both sides; the free surface of the thin film simply corresponds to the symmetry plane in the middle of the channel [69]. Hence, our considerations not only apply to thin film deformation but also to channel slip as encountered, for instance, in the microstructure of Ni-based superalloys.

I.3.3.1 Symmetrical double slip

For deformation in symmetrical double slip, the resolved shear stress in each slip system is constant and given by $|\tau| = \tau_{\mathrm{ext}} = -\sigma_{xz}\cos 2\theta$ as shown before. For each of the two slip systems, Eq. (I.3.20) transforms to

$$\frac{\cos\theta(1+D\kappa_{\mathrm{e}}^2)}{\rho^2}\partial_x\rho = -\kappa_{\mathrm{e}}(\tau_{\mathrm{ext}}-\alpha)\ . \tag{I.3.21}$$

Solution of Eq. (I.3.20) is quite straightforward, namely

$$x = h - \frac{\cos\theta}{\tau_{\mathrm{ext}}-\alpha}\left[(1-D)\frac{\kappa_{\mathrm{e}}}{\rho} + D\,\mathrm{arcsinh}\,\kappa_{\mathrm{e}}\right]\ , \tag{I.3.22}$$

where h is the scaled film height.

In the following we measure γ in units of $(b\sqrt{\rho_0})/\cos\theta$ so that $\partial_x\gamma = -\kappa_{\mathrm{e}}$ in scaled variables. The relation between γ and the dislocation density ρ from substitution into Eq. (I.3.22) becomes

$$\gamma = \frac{\cos\theta}{\tau_{\mathrm{ext}}-\alpha}\left(\frac{(D-1)+D\rho^2}{\rho}\right) + c_1\ , \tag{I.3.23}$$

where the constant c_1 is determined from the boundary condition $\gamma(0) = 0$.

Figure I.3.3 shows the size-dependent hardening behavior observed in the cases $D = 0$ (only line tension) and $D = 1$ (line tension and back stress). In the former case, one observes an Orowan behavior with an initial transient (bowing out of dislocations) and then perfect plasticity at a critical stress which scales in inverse proportion with the film thickness. The behavior for $D = 1$ is very different, as the system displays sustained hardening with a flow stress that increases, at large strains, approximately as the logarithm of strain.

To further elucidate this behavior, it is useful to have a look at the strain profiles shown in Figure I.3.4. For $D = 0$ these are segments of ellipses and, at the critical stress, $\partial_x\gamma$ diverges at the interface with the elastic substrate, indicating the onset of sustained dislocation motion at a constant stress level. (We note that for $D = 0$ and at the critical stress, the boundary condition $\gamma = 0$ at the interface need no longer be fulfilled. For $D > 0$, on the other hand, $\gamma = 0$ at the interface for all stresses). For $D = 1$ the initial behavior is similar. At larger strains, however, a roughly flat strain profile develops and a boundary layer emerges at the film-substrate interface. The width of this layer is inversely proportional to the applied stress, and the strain and dislocation density profiles are roughly exponential. This can be seen immediately by noting that the boundary layer is characterized by a large density of dislocations in near-edge orientations such that $|\kappa_{\mathrm{e}}| \approx \rho \gg 1$ in Eq. (I.3.21). The density of edge dislocations piled up against the interface increases with increasing strain, and the ever increasing back stress of these dislocations leads to the observed hardening behavior.

I.3.3.2 Single Slip

In the case of single slip, the local stress is reduced by an amount $\tau_{\mathrm{mf}} = -\Theta\gamma$ which is proportional to the local strain as shown above. In non-dimensional variables, the coefficient Θ is given by $\Theta = (\sin 2\theta)^2/(2(1-\nu)cos\theta)$. Hence our governing equation is

$$\frac{\cos\theta(1 + D\kappa_{\mathrm{e}}^2)}{\rho^2}\partial_x\rho = \kappa_{\mathrm{e}}(\tau_{\mathrm{ext}} - \alpha - \Theta\gamma) \ . \tag{I.3.24}$$

Differentiating with respect to x and using $\partial_x\gamma = -\kappa_{\mathrm{e}}$ and $\rho^2 = 1 + \kappa_{\mathrm{e}}^2$ yields

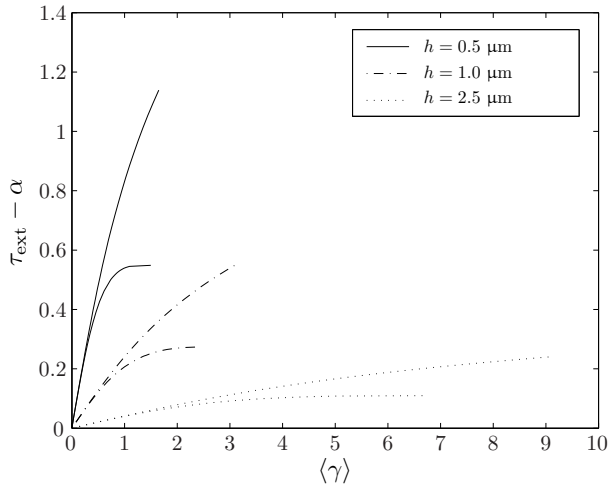

Figure I.3.3: *Stress-strain curves for films of different thickness deforming in symmetrical multiple slip; parameters:* $\rho_0 = 10^{13}\ \mathrm{m}^{-2}$, $\theta = \pi/6$, *and* $b = 2.5 \cdot 10^{-10}\ \mathrm{m}$. *In each case the lower curve refers to* $D = 0$ *and the upper curve to* $D = 1$.

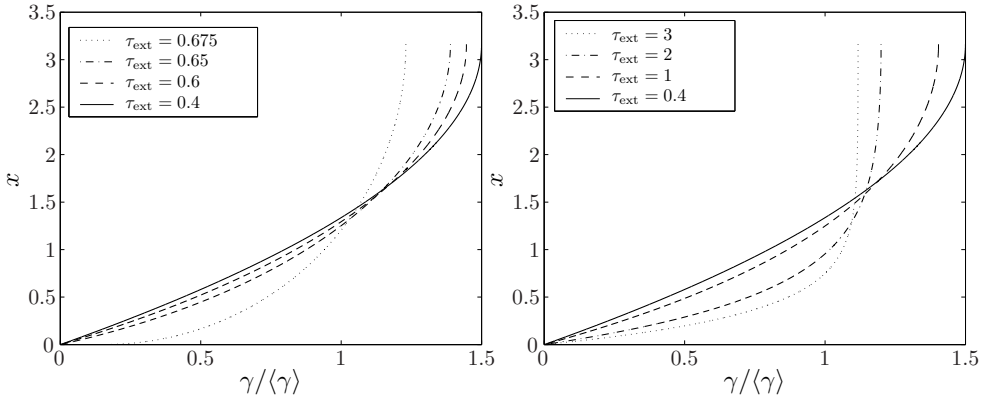

Figure I.3.4: *Plastic strain profiles for the cases* $D = 0$ *(left) and* $D = 1$ *(right), thin film shearing in symmetrical double slip. In both cases the film thickness is* $h = 1\ \mu\mathrm{m}$, *and the other parameters are as in Figure I.3.3. Stress values have been chosen to cover the full behavior range from bowing initiation to advanced hardening.*

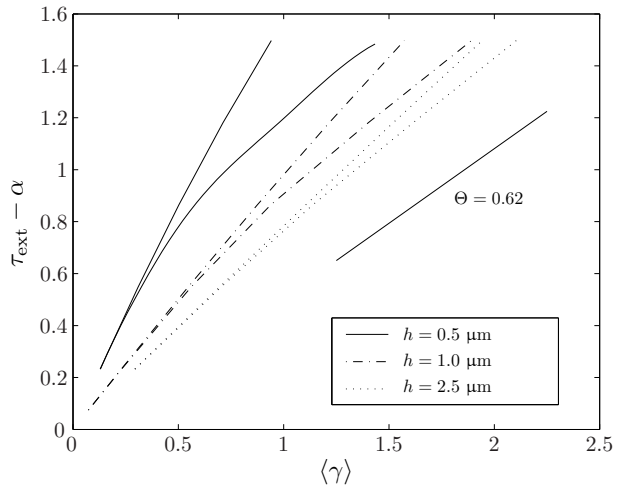

Figure I.3.5: *Stress-strain curves for films of different thickness deforming in single slip; parameters as in Figure I.3.3. In each case the lower curve refers to $D = 0$ and the upper curve to $D = 1$.*

$$\frac{1 + D\kappa_{\rm e}^2}{\rho^3}\partial_{xx}\kappa_{\rm e} + \partial_{\kappa_{\rm e}}(\frac{1 + D\kappa_{\rm e}^2}{\rho^3})(\partial_x\kappa_{\rm e})^2 = (\Theta/\cos\theta)\kappa_{\rm e} \ . \tag{I.3.25}$$

Using the substitution $w = \frac{1+D\kappa_{\rm e}^2}{\rho^3}\partial_x\kappa_{\rm e}$ into Eq.(I.3.25) we obtain an Abel equation of the form

$$w\frac{\partial w}{\partial\kappa_{\rm e}} = \frac{\Theta}{\cos\theta}\kappa_{\rm e}\frac{1 + D\kappa_{\rm e}^2}{\rho^3} \ , \tag{I.3.26}$$

from which we find that

$$\partial_x\kappa_{\rm e} = \pm\frac{\rho^3}{1 + D\kappa_{\rm e}^2}\sqrt{c + 2\frac{\Theta}{\cos\theta}(\frac{D-1}{\rho} + D\rho)} \ . \tag{I.3.27}$$

In order to determine the value of the integration constant we adopt an iterative procedure since the imposed boundary conditions do not allow for direct evaluation. Starting from the condition $\kappa_{\rm e}(h) = 0$ we seek c values that eventually satisfy the prescribed relation $\gamma(0) = 0$. Alternatively, a purely numerical solution based on a forward difference has been used and was found to produce equally accurate and less cumbersome results.

The deformation behavior at first glance differs significantly from that in symmetrical double slip. The reason for this is that a mesoscopic 'fibre stress' is building up in the film.

This stress is proportional to the strain and counteracts the externally applied stress. As a consequence, one observes an apparent hardening even in the $D = 0$ case. In this case, after an initial transient which depends on specimen size, an asymptotically linear stress-strain relationship with size-independent slope Θ is approached (see Figure I.3.5). For $D = 1$, on the other hand, the presence of an additional 'back stress' due to dislocations piling up against the film-substrate interface leads to an enhanced hardening which becomes more pronounced as the specimen size decreases.

The presence of the strain dependent 'fibre stress' diminishes the visible differences in strain profile between the $D = 0$ and $D = 1$ cases (Figure I.3.6). However, the asymptotic characteristics of the profiles in the large-strain limit remain similar to the double slip case, *viz*, a semi-elliptical profile with vertical slope near the film-substrate interface for $D = 0$, and two boundary layers of diminishing thickness for $D = 1$. This indicates that, in spite of the apparent hardening associated with the build-up of a 'fibre stress' in the film during single-slip deformation, the basic deformation mechanisms in either case are the same as for symmetrical double slip.

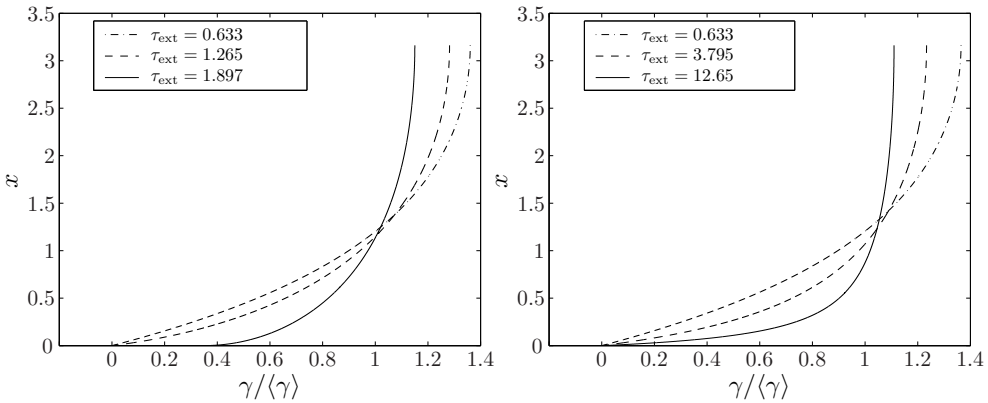

Figure I.3.6: *Plastic strain profiles for $D = 0$ (left) and $D = 1$ (right), thin film shearing in single slip. Parameters as in Figure I.3.4.*

I.3.4 Bending of a free-standing thin film

For the bending of a free-standing thin film, the elastic and plastic strains are zero along the neutral axis $x = 0$, $\gamma(0) = 0$. Because of symmetry reasons, it is sufficient to solve the problem on the interval $x \in [0, h/2]$. At the free surface of the film, the boundary condition is again $\kappa_{\rm e}(h/2) = 0$. No other boundary conditions are imposed. We note in passing that Sedlacek [70] treated the same problem by imposing that the strain be zero within an 'elastic core' of the strip. This assumption necessarily introduces discontinuities in the derivative of the strain γ, corresponding to points of infinite curvature of the dislocation lines. We find it difficult to see how this can be reconciled with the use of a line-tension approximation for describing the dislocation self-interactions.

The governing equation for this problem is similar to the previous ones, with the difference that the 'external' stress now is a linear function of the x coordinate,

$$\frac{\cos\theta(1+D\kappa_{\rm e}^2)}{\rho^2}\partial_x\rho = \kappa_{\rm e}(mx - \Theta\gamma - \alpha) = \kappa_{\rm e}(\tau_{\rm ext}(x) - \tau_{\rm mf}(\gamma, x) - \alpha)\ , \qquad \text{(I.3.28)}$$

where the constant m depends on the applied bending moment (cf. above).

Again, there is a mesoscopic internal stress in the film which is a function of the strain in either of the slip systems. Going through the same steps as in the previous sections, we finally obtain

$$\frac{1+D\kappa_{\rm e}^2}{\rho^3}\partial_x\kappa_{\rm e} = \pm\sqrt{c + 2\frac{m[(1-D)\kappa_{\rm e} + D\,\rho\,\mathrm{arcsinh}\,\kappa_{\rm e}] + \Theta(D-1+D\rho^2)}{\rho\cos\theta}}\ . \qquad \text{(I.3.29)}$$

Again, we use an iterative procedure to obtain a solution which is consistent with the assumed boundary conditions. To this end, we chose a value of m and then adjust the integration constant c to satisfy the boundary condition $\kappa_{\rm e} = 0$ at the free surface $x = h/2$. We then evaluate the strain profile, using $\partial_x\gamma = -\kappa_{\rm e}$ with the boundary condition $\gamma(0) = 0$, and determine the average strain and the scaled bending moment M defined by

$$M = \frac{4}{\sin 2\theta}\int_0^{h/2}(\tau_{\rm ext} + \tau_{\rm mf})x\,dx = \frac{4}{\sin 2\theta}\int_0^{h/2}(mx - \Theta\gamma)x\,dx\ . \qquad \text{(I.3.30)}$$

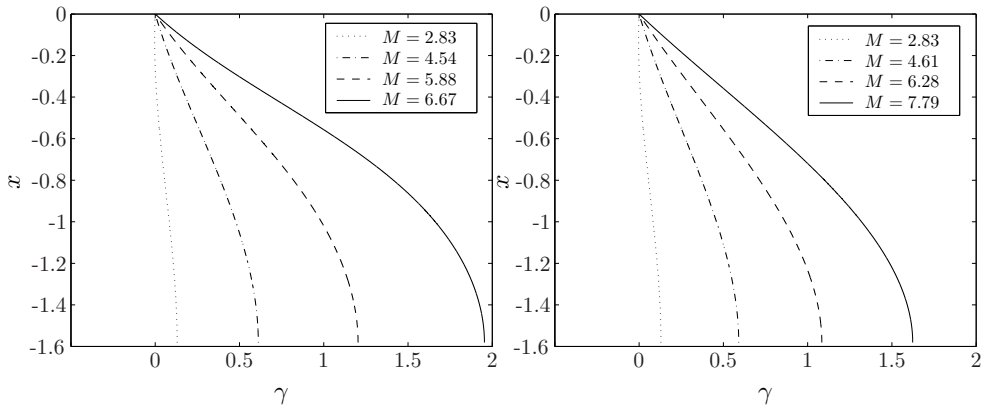

Figure I.3.7: *Inhomogeneous plastic strain distribution in bending for $D = 0$ (left) and $D = 1$ (right). Both figures are produced for film thickness $h = 1$ μm, other parameters as in Figure I.3.3*

An investigation of strain profiles obtained in this manner (Figure I.3.7) demonstrates significant differences with the shearing problem. Strain profiles for $D = 0$ and $D = 1$ are very similar, with strain fields that go smoothly to zero at $x = 0$. No boundary layer effects are observed, and there is no evidence of an 'elastic core' as imposed by Seldacek [70] through a corresponding boundary condition. A comparison with the results of Sedlacek shows that, in the present model, strains may become negative in the vicinity of the neutral axis, i.e., dislocations there bow in a direction opposite to that imposed by the applied bending moment. (An explicit comparison of strain profiles obtained with our and with Sedlacek's boundary condition has been given by Sedlacek in the appendix to [70].) Generally speaking, our theory yields larger strains for small stresses (the system is softer), however, for large bending moments our $D = 0$ results approach those of Sedlacek, since in this limit the boundary conditions become asymptotically similar (zero strain at or near $x = 0$).

In spite of the apparent similarity in the strain profiles the hardening behavior in the $D = 0$ and $D = 1$ cases is quite different. This can bee seen in Figure I.3.8 which shows for different film thicknesses h plots of the normalized bending moment M/h^2 versus the average strain in a half-strip, $\langle\gamma\rangle = \int_0^{h/2} \gamma(x)\mathrm{d}x$.

In the absence of the 'back stress' term ($D = 0$), the normalized bending moment M/h^2 approaches a constant value which for large h is proportional to the flow stress constant α. For smaller h, one observes an initial transient and an asymptotically constant level of M/h^2 which is roughly in inverse proportion with h, indicating an Orowan-type size effect. If the

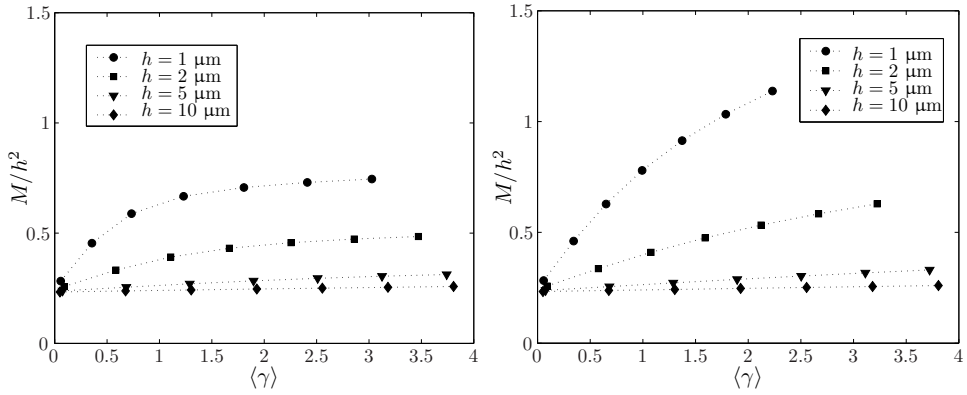

Figure I.3.8: *Size dependence of the bending response (Strain average over half-strip vs. normalized bending moment) for $D = 0$ (left) and $D = 1$ (right). Parameters as in previous figures.*

back stress term is taken into account $(D = 1)$, on the other hand, the deformation behavior changes significantly. Owing to the condition $\gamma(0) = 0$, dislocations increasingly bend into edge orientations and the accumulation of edge dislocations of the same sign in either half-strip leads to an ever increasing back stress which gives rise to sustained hardening, with a hardening rate that increases strongly with decreasing film thickness.

Chapter I.4
Synopsis & Discussion

We have presented a framework which generalizes previous approaches towards density-based dislocation dynamics in order to describe the kinematics and interactions of curved dislocation lines. We subsequently utilized the theory to solve a series of reference problems with simple plane-strain deformation geometries. In conclusion of our study, we assess the predictive power of the approach by comparing the obtained results with recent experimental data on bending of micron-sized samples as well as with three-dimensional discrete dislocation dynamics (3DDD) simulations of microbending. Finally, we briefly discuss the relationship of our approach with other density-based models and assess its performance in view of the general state-of-the art in modelling of dislocation systems.

I.4.1 Side by side with experimental observation

The ultimate criterion for evaluating a theoretical approach is its ability to reproduce and predict experimental observations. For mesoscopic and continuum models, a second method of validation consists in comparing their performance with the results of more elaborate computational models which retain the full microscopic information. In the following, we validate our model by comparing our results with recent microbending experiments by Motz et al. [16], as well as with the results of 3DDD simulations of microbending by Weygand, Motz and co-workers [72, 73].

I.4.1.1 Microbending experiments

Our investigation of the bending deformation of a free standing homogeneous thin film revealed a strongly size dependent behavior which was brought up by a controlling mechanism distinct from those assumed in classical continuum theories. Microbending experiments have been performed on various materials, prepared with various methods and referring to either single crystals or polycrystals. As the plastic response of polycrystals may be significantly altered by

the presence of grain boundaries, we mainly refer to the experiments performed by Motz et al. [16] who investigate the bending behavior of monocrystalline beams with thicknesses down to about one micron. In line with the results of the present theoretical study, these experiments indicate that an Orowan mechanism enhanced by pile-up stresses governs the bending response in the micron-sized regime.

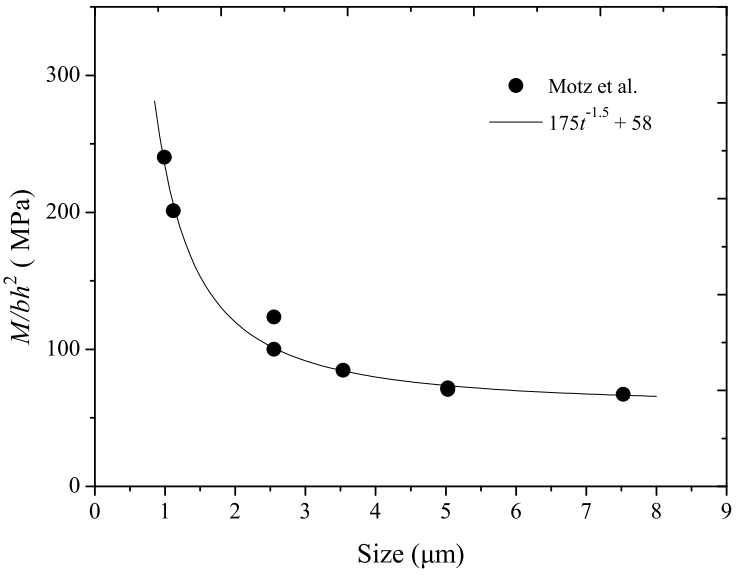

Figure I.4.1: *Experimental bending strength of Cu single crystals, after Motz et al. [16]. Full line: fitted power law. Size corresponds to thickness of the bended beam and the moment stress M/bh^2 to the ultimate load sustained.*

Motz et al. evaluate the bending strength in terms of the ultimate load acting on the beam by assuming a stress distribution characteristic of a perfectly plastic material. As depicted in Figure I.4.1 the size-strength relation obtained in this manner is well fitted by a power law with an exponent of about -1.5. This is below the exponent of -1 which characterizes the Orowan mechanism of dislocation bowing, and thus the contribution of line tension to the dislocation stress field. Motz et al. interpret this finding by assuming excess pile up stresses originating from a family of dislocation sources. Still, their results seem to underestimate the strengthening process which takes place for decreasing sample sizes. It is noticeable that the proposed power law should trivially converge to a constant stress value matching the size insensitive limit.

From the preceding chapters we expect that the description of dislocation interactions used in the present study, which assumes a constant flow stress 'background' and combines line

tension with a collective pile-up stress that develops in the dislocation ensemble, might yield an appropriate characterization of this size-dependent deformation behavior. This claim needs to be validated by quantifying the size-dependent strength predicted by the model and comparing this with experimental observations.

For determining flow stresses from the theoretical deformation curves, we use the engineering concept of defining the flow stress as the stress value corresponding to a fixed small value of the plastic strain. In bending where strain is not constant along the specimen thickness, we use a threshold value of the surface strain for this purpose. As shown in Figure I.4.2, the thus defined flow stresses exhibit a strong size effect which follows a power law with an exponent -1.5, in agreement with various experimental results. The values used in the calculations were $\alpha = 1$, $\rho_0 = 2 \cdot 10^{13}$ m^{-2}, $D = 0.7$ and $\theta = 40°$, together with Al material parameters. Increasing the threshold strain value used for defining the flow stress leaves the size exponent unchanged, but shifts the absolute values of the flow stresses upwards towards the experimental data that refer to ultimate loads.

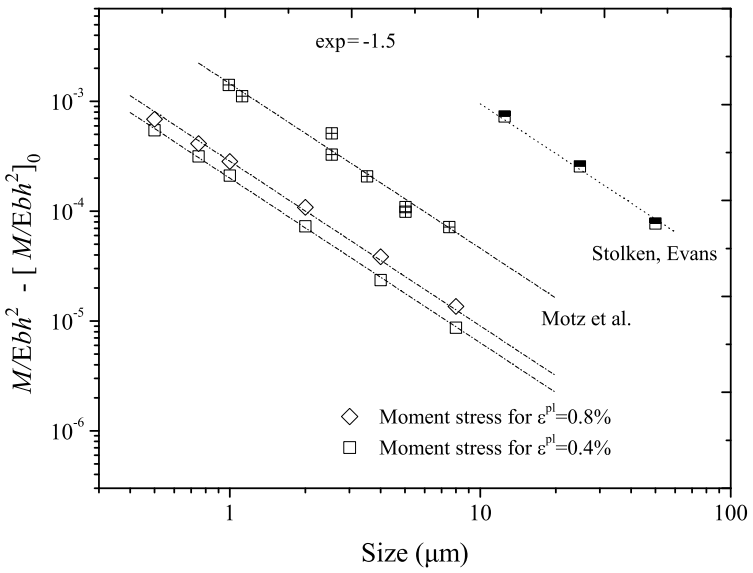

Figure I.4.2: *Comparison between size-dependent flow stresses (normalized bending moments minus their asymptotic values) obtained from our calculated bending curves and experimental data. Both theoretical and experimental data are well described by a power law relation with exponent* -1.5

I.4.1.2 Dislocation dynamics simulations

Besides comparison with experimental data, a second method of validating mesoscopic or macroscopic models is their comparison with the results of computations that operate on a more microscopic scale and thus may give a more faithful representation of the physical processes. This validation approach is particularly useful if the microscale model operates on the basis of first principles, rather than depending on a large amount of phenomenological input. To a certain extent this is true for 3DDD simulations which give a complete and relatively accurate description of the interactions of discrete dislocation lines which depends on no other input than the use of well established results from elasticity theory. A comparison of our results with those of 3DDD simulations is particularly desirable as our theory is supposed to provide an coarse-grained representation of the dynamics of discrete dislocation systems. Hence, the physical reality described and even the phenomenological 'input' of the theories are very similar, the main difference being a coarse graining step involved in the transition from dynamics of discrete lines to dynamics of continuous densities. By comparing results of both approaches, it should be possible to assess the impact of the inevitable approximations involved in our coarse graining procedure, which represents the actual interactions of discrete lines by semi-phenomenological 'flow stress' and 'back stress' terms.

From the dislocation dynamics simulations carried out by Weygand and co-workers [72, 73], various interesting conclusions emerged. Most of them concern the burst-like nature of deformation on small scales, which appears as a sequence of discrete bursts rather than a lamellar flow. This behavior will be examined in Part II of this thesis. The present theory, which does not allow for fluctuation phenomena, can be considered a representation of the discrete dynamics in terms of statistical averages; accordingly, we compare in the following with the data that are obtained after averaging the strongly fluctuating bending response in the 3DDD simulations over many simulation runs.

In the 3DDD simulations, the simulated system was a monocrystalline beam consisting of a fcc metal (parameters of Al were used) and oriented along a [100] axis, which was deformed in pure bending. The initial dislocation arrangement was defined by a random distribution of dislocation sources of fixed length $l_0 = 0.22\ \mu\mathrm{m}$, representing an initial dislocation density of $\rho_0 = 2 \times 10^{13}\ \mathrm{m}^{-2}$. These sources were distributed evenly in space and over the available slip systems, with the additional condition that sources were not allowed to intersect the specimen surface. A bending moment was applied by appropriately displacing the end faces of short

beams with aspect ratio 3:1:1 and various thicknesses. The simulations record the positions of all dislocation lines in the deformed samples, as well as the applied bending moment and the total bending strain.

To compare our calculations with the 3DDD simulation results, we have to adjust the parameters of our continuum model to match the situation in the simulations. The continuum model contains four parameters: (i) the initial dislocation density ρ_0, (ii) the inclination angle θ of the slip systems, (iii) the flow stress parameter α, (iv) the back stress coefficient D:

(i) The initial dislocation density is chosen to be the same as in the 3DDD simulations, $\rho_0 = 2 \times 10^{13}$ m^{-2}. (ii) At sufficiently large strains, the dislocation density increase in bending is almost exclusively due to the accumulation of geometrically necessary dislocations (GND), and the parameter θ determines the ratio of the actual dislocation density increase to the minimum increase in GND density that would be required if the dislocation Burgers vector were parallel to the z direction. Owing to the somewhat different slip geometries in the 3DDD simulation and the continuum model, we treat θ as an adjustable parameter which we chose such as to correctly represent the observed dislocation density increase in the plastic regime (Figure I.4.3).

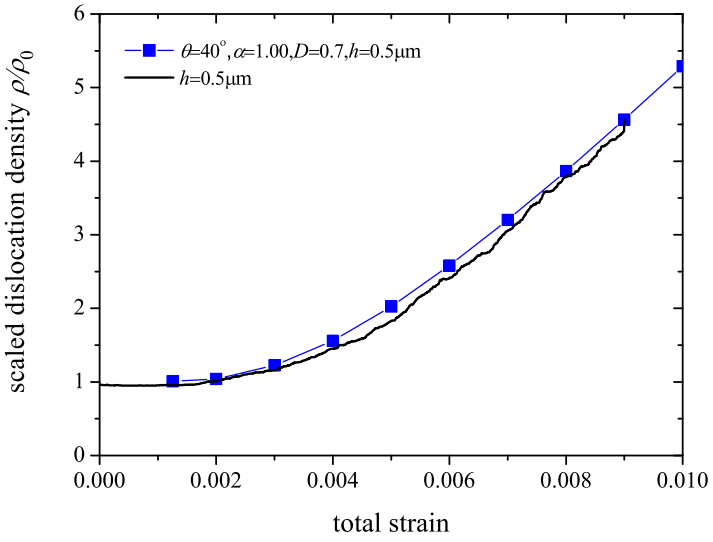

Figure I.4.3: *Evolution of the total dislocation density with increasing strain. The geometrical parameter θ is determined by fitting to the linear increase of the dislocation density at large strains.*

(iii) The flow stress parameter α in our model characterizes the contribution of short-range dislocation interactions to the flow stress, and determines the initial point of yielding of the material. In the 3DDD simulations, the yield stress is governed by the source length - it is essentially the Orowan stress of the sources. We therefore adjust α such as to represent this yield-stress controlling mechanism. Yielding occurs first at the surface where the stress is highest. Since, in the 3DDD simulations, sources are separated from the surface by a distance of at least their half-length $l_0/2$, and the stress profile is linear prior to yielding, this happens when the surface stress (resolved shear stress in the active slip systems) meets the condition $\tau_{\text{surf}}(h - l_0)/h = C_{\text{LT}}Gb/l_0$ where C_{LT} is a constant of the order of one which characterizes the line energy of the dislocations. In our continuum model, on the other hand, yielding occurs at the surface once the surface stress meets the flow stress, $\tau_{\text{surf}} = \alpha Gb\sqrt{\rho_0}$. Equating both relations, we obtain $\alpha = C_{\text{LT}}h/[(h - l_0)l_0\sqrt{\rho_0}$. The constant C_{LT} is treated as a fit parameter, and an adequate fit of the stress-strain curves is obtained by adjusting C_{LT} such that $\alpha \approx 1$ for $h = 0.5$ µm. α values for other thicknesses are then obtained from $\alpha_h = \alpha_{0.5}(h/0.5) \cdot (0.5 - 0.22)/(h - 0.22)$. (iv) The back stress parameter D governs the hardening behavior and is determined by fitting to the stress-strain curves in the plastic regime.

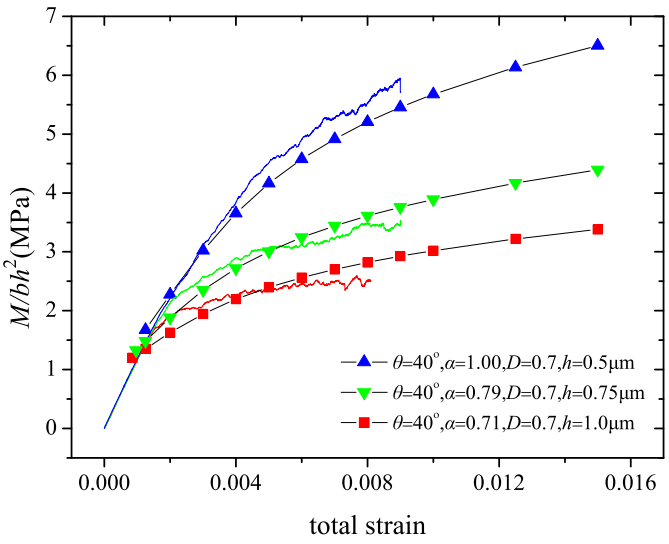

Figure I.4.4: *The figure shows fits of our continuum results to the 3DDD simulations. The legend shows the parameters used.*

It is seen that, in spite of the significant differences in the initial dislocation configuration, the

discrete and continuum models provide a good match as seen on Figure I.4.4 for all the range of thickness tested, once the flow stress parameter α is adjusted to match the different flow stress controlling mechanisms, leaving only D as a fitting parameter to be estimated. It is notable that with no change of D fittings were consistent throughout the studied regime of sizes.

Both the continuum and discrete dislocation dynamics models give access to the spatial patterns of dislocations and to the plastic strain profiles which characterize the inhomogeneous deformation process. Profiles of the dislocation density tensor α_{ij} were extracted from the simulations by cutting the bending beam into slices perpendicular to the x axis and evaluating the dislocation density tensor as

$$\alpha_{ij}(x_k) = \frac{1}{V_k} \sum_{n \in V_k} l_{n,i} b_{n,j} \tag{I.4.1}$$

where the sum runs over all dislocation segments contained in the slice of volume V_k centered around x_k, $l_{n,i}$ is the projection of the nth segment on the x_i axis, and $b_{n,j}$ the projection of its Burgers vector on x_j. Dislocation density tensor profiles were averaged over several simulations and strain profiles $\varepsilon_{zz}(x)$ were obtained by integration, using the relation $\alpha_{yz} = \partial_x \varepsilon_{zz}^{\mathrm{pl}}(x)$. Results are shown in Figure I.4.5 together with strain profiles obtained from the continuum model, using the same parameterization as above.

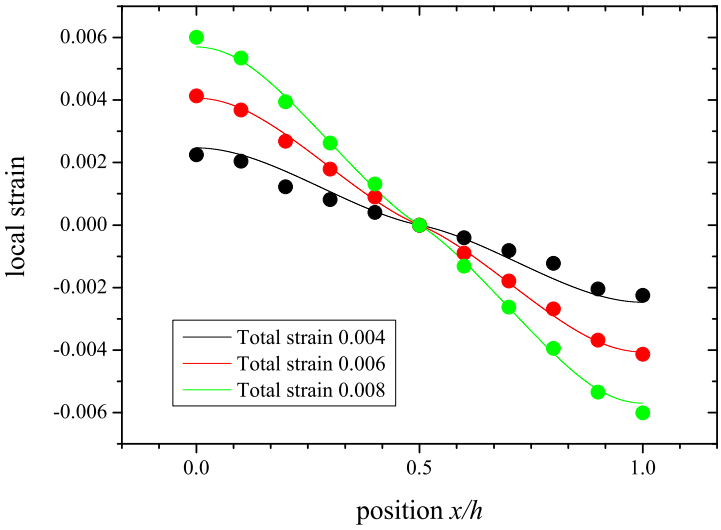

Figure I.4.5: *Local distribution of the plastic strain across the specimen thickness for a specimen of thickness $h = 1.5$ µm and various values of the bending strain (total surface strain).*

It is seen that the strain profiles produced by the discrete and continuum dislocation dynamics models are very similar. Notable is the complete absence of the central elastic zone predicted by classical plasticity theory. Instead, at small total strains we find that the strain profiles exhibit three inflection points. At larger strains, the profiles straighten out and become almost linear in the central part of the sample, curving to horizontal near the surfaces. The agreement between discrete and continuum models is achieved despite the striking differences in the initial dislocation configuration (straight threading dislocations of uniform orientation vs. randomly oriented and distributed sources). This can be interpreted to imply a relative independence of the response from many details of the initial dislocation distribution, flow mechanism and even deformation geometry. In particular it is important that the evolution of the geometrically necessary dislocation arrangement, or equivalently the strain profile, virtually coincides in the discrete and continuum models. This is a strong indication that the present modelling approach holds a strong physical foundation and is not just another nice phenomenological fitting of limited use. The dislocation state is captured in a precise manner and this is of key importance for any investigation to follow.

I.4.2 General discussion and conclusions

To put our work into context, we focus on other investigations related to the formulation of statistical averages and the incorporation of 'microscopic' dislocation interactions into dislocation density-based theories of plasticity. A mathematical discussion of the formal relations between different density-based approaches that have been proposed for describing systems of curved dislocations [42, 59, 60] can be found elsewhere [61, 62].

The different theories proposed in the literature differ in the density measures used. Accordingly, the evolution equations have at first glance different formal structure. For systems of discrete dislocation lines, however, any sensible theory reduces to the classical kinematic evolution equation of the dislocation density tensor, and therefore for this case all density-based theories tend to be equivalent. The same is true for continuously distributed bundles of parallel dislocations, where it is possible to uniquely assign a dislocation orientation to each point in space. As far as the kinematics of such problems is concerned, the choice of any particular theory seems to be largely a matter of taste.

Problems arise, however, as soon as one leaves the discrete-dislocation scale and proceeds to

do averages. In general, dislocation arrangements consist of segments of multiple orientations within one and the same mesoscopic volume element. This leads to two problems: (i) Relevant kinematic information is lost if one uses the average dislocation density tensor only. This problem is well-known: The rotation-free plastic distortion which results from the motion of 'statistically stored' dislocations with zero net Burgers vector cannot be captured in terms of the averaged dislocation density tensor, which depends only on the *excess* Burgers vector contained within the averaging volume. (ii) A second problem is less commonly addressed. The dynamics of dislocation segments depends on the stresses acting *on the segments*. It is therefore inadequate to describe the local stress state in terms of a simple volume average over some mesoscopic volume – rather, one has to take conditional averages over only those positions within the mesoscopic volume element which are actually occupied by the type of dislocations under consideration. Speaking in physical terms, one has to find a way of keeping track of the relative orientation of dislocation segments and the topological structure of the dislocation network, as these are the parameters which determine the local flow stress.

In the present work, we used a semi-phenomenological model which describes 'microscopic' dislocation interactions in terms of a local flow stress fulfilling Taylor's relation, plus two nonlocal terms related to dislocation curvature ('line tension' stress) and to repulsive stresses between individual dislocations of the same sign ('back stress'). In particular, we have shown for different constrained deformation geometries (shearing of a thin film (or equivalently a slip channel), microbending) that the first of these terms leads to an Orowan-type size effect on the flow stress. Inclusion of the second term leads to sustained size-dependent hardening as dislocations in near-edge orientations with increasing strain pile up against the intrinsic boundaries (the film-substrate interface in case of thin film shearing and the neutral fiber in the case of bending). In the thin film case, the 'back stress' term gives rise to the formation of a boundary layer with an excess dislocation density that decreases exponentially from the boundary, and a corresponding increase of the strain. Similar exponential boundary layers have been reported in experiments (deformation of bicrystals [74]) as well as in discrete simulations of deformation of thin films or, equivalently, slip channels [75]. In the case of microbending, the 'back stress' leads to a stronger dependence of the flow stress on size than expected for pure Orowan behavior, in agreement with experimental observations. For microbending, the calculated stress-strain curves and strain profiles are in good agreement with the results of 3DDD simulations, indicating that our approach succeeds in adequately capturing essential features of the interactions of discrete dislocation lines within a continuum setting.

Further investigations are required to validate the present or similar continuum approaches by comparing the results with discrete dislocation dynamics simulations for other deformation setups. We have seen that the present theory is capable of reproducing some key features of discrete simulations - it allows to understand size effects on flow stress and hardening, as well as the formation of boundary layers in constrained plasticity. However, there is still scope for improvement. In particular, none of the presently available continuum models has yet managed to include in a consistent manner the operation of localized sources (as opposed to the bowing of dislocations which thread the entire system). At the same time, systematic investigations of size effects in various geometries by 3DDD simulation are still missing. Owing to the inherently stochastic character of microplasticity, such simulations, to be useful, have to be carried out as statistical ensemble simulations rather than 'one-off' runs - a requirement which obviously greatly increases the computational effort. In conclusion, we think it necessary to include dislocation multiplication and sources into the present, or related, continuum theories and to provide 3D benchmark simulations for assessing the validity of such generalizations.

From a continuum mechanics viewpoint it is interesting to note that both the 'back stress' and 'line tension' terms can be understood as stresses which relate to second-order gradients of the plastic strain: The line tension is a second gradient of the plastic shear strain in the dislocation line direction, and the back stress (or 'pile-up stress', cf. [54]) is a second gradient of the plastic shear strain in the direction normal to the dislocation line. This suggests that, in the spirit of Aifantis' proposition to introduce second-order strain gradients into macroscopic plastic flow rules (see e.g. [21, 52]), it might be possible to unify both terms to yield a generic formalism of gradient-dependent dislocation dynamics. This is another issue to be explored in the future.

Part II

Fluctuation phenomena in micro-plasticity

Chapter II.1
Introductory Remarks

The images of metals being rolled into sheets, being forged by blacksmiths or the simple everyday bending of a paperclip are at the root of the common perception that plasticity is in its essence a smooth and steady flow of material. However, recent experimental findings ranging from compression tests on micron-sized specimens to acoustic emission measurements on macroscopic crystals demonstrate that deformation on microscopic and mesoscopic scales proceeds through an intermittent series of bursts ('slip avalanches') with power-law size distribution – attribute which indicate a collective organization to a critical-like state. Such characteristics seem to match well the framework of Self Organized Criticality (SOC) [76–78] and a number of its concepts were utilized in the explanation of the underlying dislocation dynamics that control the evolution of plastic deformation.

These new discoveries question the validity of our long used mean field approaches where fluctuations – however conspicuous they may be – are neglected by definition. In this chapter we present an overview of experimental and theoretical investigations exploring the intermittent and heterogeneous nature of plasticity which motivate the questions that we address in our subsequent analysis.

II.1.1 Avalanches in plasticity: Experimental observations

Localization of deformation on macroscopic scales has been a major challenge for the development of appropriate constitutive models for many years. Macroscopic localization commonly initiates and subsequently evolves in the material softening regime where the ensuing plastic instabilities can give rise to various kinds of interesting phenomena. The necessity to formulate constitutive equations capable of capturing the phenomenon of spontaneous deformation localization in a mathematically well-posed manner led to the development of gradient plasticity models as introduced by Aifantis and co-workers [50, 51, 79] and a vast number of other researchers. In many physical situations the inclusion of gradient terms proved to be a mathe-

matically sound and physically motivated means for dealing with the problem of heterogeneous deformation in unstable plastic flow.

However, deformation heterogeneity and slip localization are not necessarily associated with macroscopic deformation instabilities. On the microscopic scale, slip localization is a trivial consequence of the discreteness of defects. In crystalline solids the Burgers vectors of dislocations, which carry the plastic deformation, evidently define discrete 'quanta' of slip. Slip localization phenomena which take place in spite of macroscopically stable deformation may also be observed on mesoscopic scales where they involve the collective dynamics of very large numbers of elementary defects. A classical example is the formation of slip lines or slip bands in crystalline solids deforming by planar slip (for an extensive report of experimental observations see [80]). The slip steps on the surface of these materials manifest the collective motion of large numbers of dislocations, leading to an intense deformation that is highly localized on the sub-micron scale while macroscopic deformation is smooth and homogeneous. It has been shown by different authors that slip patterns exhibit long-range spatial correlations which can be described in terms of fractal statistics. The relationship between the fractal nature of slip and the surface morphology of plastically deformed crystals has been discussed by Zaiser et al. [81], who demonstrated that the surface of plastically deformed Cu samples develops self-affine roughness over several orders of magnitude in scale.

Heterogeneity of slip in spite of macroscopically stable deformation is illustrated in Figures II.1.1-II.1.2. Figure II.1.1 shows surface profiles of a Cu polycrystal with an initially flat surface (rms roughness < 2 nm as determined by atomic force microscopy over an area of 6×6 $\mu\mathrm{m}^2$) after deformation to 9.6% tensile strain. The statistically self-affine nature of the profiles can be inferred by comparing profiles taken on different scales: here by atomic force microscopy (AFM, profile length 25 μm) and scanning white-light interferometry (SWLI, profile length 2 mm). A quantitative measure of self-affinity is the so-called Hurst exponent H: For a self-affine profile $y(x)$ the average height difference $|y(x) - y(x + L)|$ increases like L^H (see Figure II.1.2). Zaiser et al. [81] find that the Hurst exponent of surface profiles from tensile Cu samples decreases within the first few percent of strain and then saturates at $H \approx 0.75$. Such a result of $H > 0.5$ emphasizes the existence of long range correlations and collective action of dislocations.

Recent compression experiments on micrometer sized Ni single crystals performed by Dimiduk et al. [82] revealed even more remarkable features of the mechanisms underlying plasticity (as

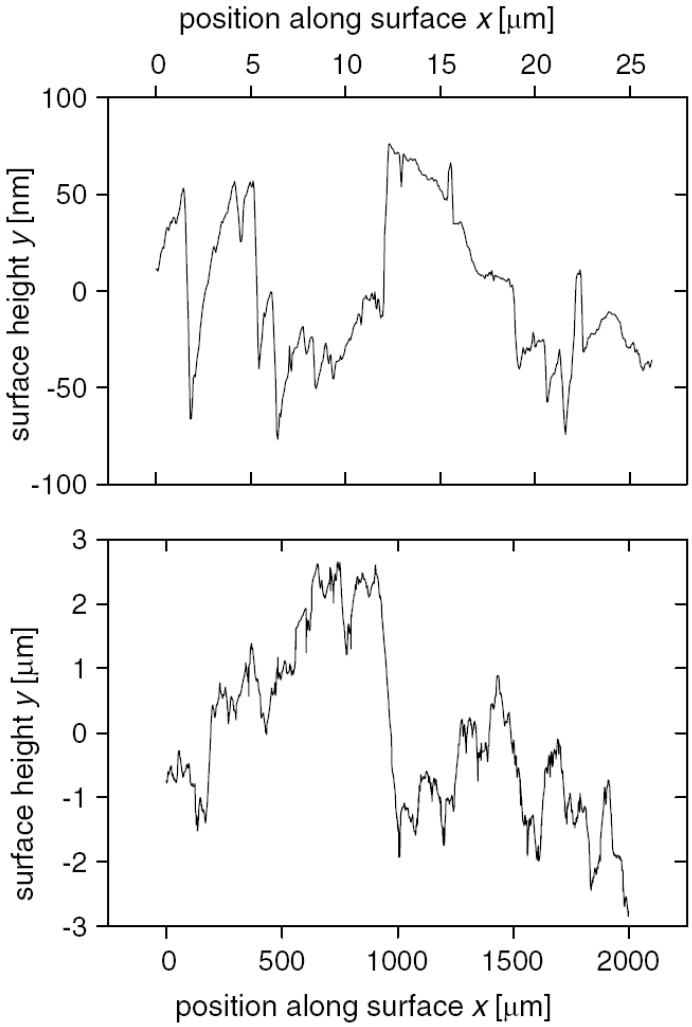

Figure II.1.1: *Surface profiles of a Cu polycrystal deformed in tension to a total strain* $\varepsilon^{\mathrm{tot}} = 9.6\%$. *Top: AFM profile; bottom: SWLI profile. The x direction is parallel to the direction of the tensile axis. After Zaiser et al. [81]*

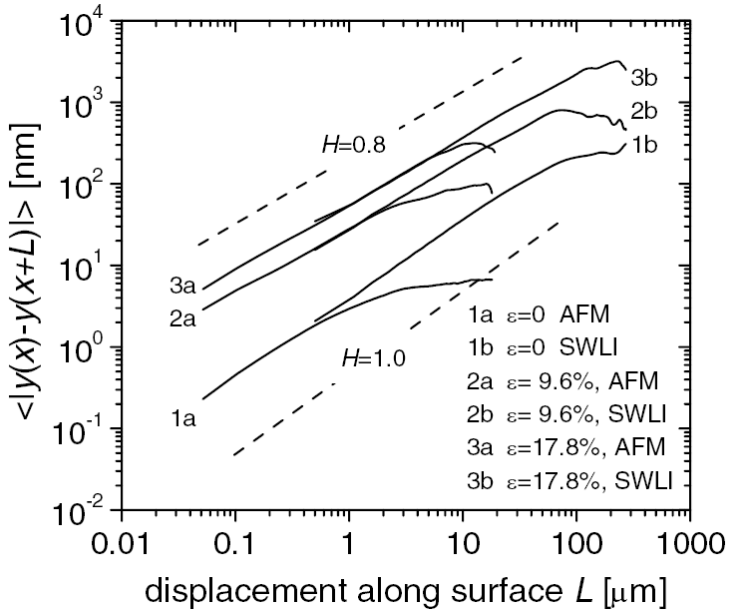

Figure II.1.2: *Roughness plots (mean height difference versus distance along the profile) for AFM and SWLI profiles obtained at strains of* 9.6 *and* 17.8%*. The corresponding profiles for* $\varepsilon^{\mathrm{tot}} = 9.6\%$ *are shown in Figure II.1.1. After Zaiser et al. [81].*

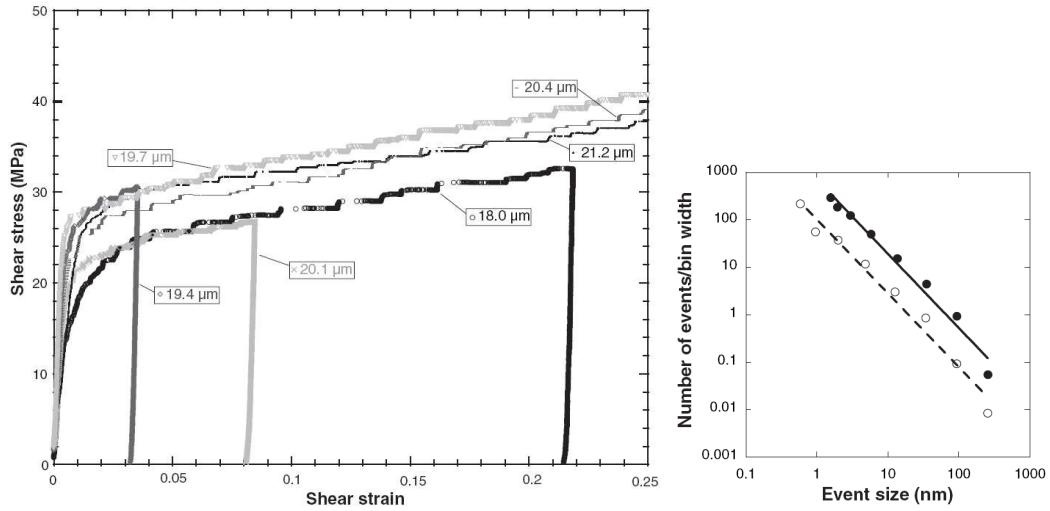

Figure II.1.3: *Left: Selected shear-stress versus shear-strain curves for Ni samples with* $\langle 2, 6, 9\rangle$ *orientation,* $\approx 20\ \mu\mathrm{m}$ *in diameter, showing intermittency of strain and stress. Right: Event frequency distribution showing the number of slip events of a certain size versus event size, plotted on logarithmic scales. Power law scaling over more than two orders of magnitude is exhibited for both a single sample* $\approx 20\ \mu\mathrm{m}$ *in diameter (open circles and dashed line fit) and the aggregate data from several samples (solid circles and solid line fit). After Dimiduk et al. [82].*

illustrated in Figure II.1.3). Dimiduk et al. were able to identify discrete events which lead to a step-like, strongly size-dependent material response. Analysis of the frequency of large events indicates power law scaling analogous to the frequency distribution of earthquake magnitudes where shock and aftershock action seem to obey very consistent power law distributions (for additional details see [83]).

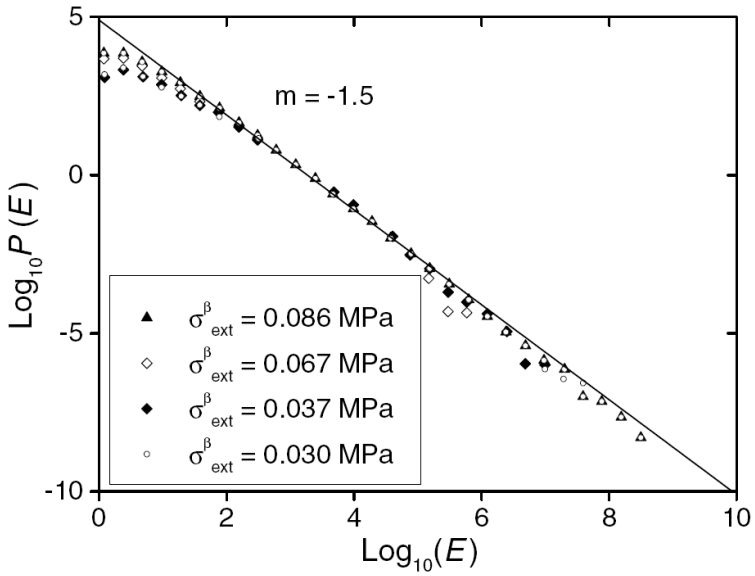

Figure II.1.4: *Distribution of energy releases in acoustic emission during creep deformation of ice single crystals; temperature* $263\ \mathrm{K}$*, resolved shear stresses on the basal plane as indicated in the inset. After Miguel et al. [84].*

Information about the temporal dynamics of plastic flow can also be acquired from acoustic emission measurements. Measurements on ice single crystals reported by Miguel et al. [84] and Weiss and Grasso [85] indicate an intermittent acoustic signal composed of discrete 'events' with a scale-free size distribution extending over more than 8 orders of magnitude without any apparent cut-off. The probability density to observe events with energy release E decreases according to $p(E) \propto E^{-1.6}$ (Figure II.1.4). All these observations indicate that plastic deformation proceeds in avalanches with a power-law size distribution reminiscent of the power-law distributions observed in many systems close to critical points.

II.1.2 Theoretical approaches

Although accurate in many aspects, deterministic continuum models like those formulated in Part I of the present thesis are incapable of accounting for spatio-temporally fluctuating behav-

ior since fluctuations are eliminated almost by definition through the averaging steps required to arrive at a continuum density-based formulation. Therefore, such models may give access to the *average* deformation behavior that emerges if the sample is large or the deformation response is averaged over many small samples. They can, however, not account for the fluctuations of plastic flow that are conspicuous in the deformation of individual micron- and submicron sized samples. Therefore, alternative modelling techniques that are able of capturing the avalanche dynamics in plasticity were pursued in a number of theoretical approaches. These approaches differ in the way the deformation state is represented; however, the main results obtained from all of these fit themselves into a consistent picture of plastic yielding as a non-equilibrium phase transition. Not going into further details, the three major models that may be employed are: (i) models which describe plastic flow in terms of the deterministic motion of discrete lattice dislocations (discrete dislocation dynamics) with random initial distribution [72]; (ii) phenomenological models which describe plastic deformation in terms of the evolution of shear strain on crystallographic slip systems [86, 87], and account for the influence of the underlying dislocation dynamics in terms of fluctuations in the local stressstrain relationship (stochastic continuum models); (iii) phase-field models which take an intermediate position as they describe plasticity in terms of shear strain on crystallographic slip systems, but resolve the strain on a scale where individual dislocations can be identified as localized gradients of the strain field [88]. Each of these models is capable of describing heterogeneity and avalanche phenomena in plastic flow, and the available results appear to be mutually consistent.

II.1.3 Scale free or near scale-free?

As we have seen in Section II.1.1, plastic strain increments $\Delta\varepsilon$ [1] produced by slip avalanches are power-law distributed, $p(\Delta\varepsilon) \propto \Delta\varepsilon^{-\kappa}$ where the exponent κ is found to be approximately 1.5 [82, 84, 86, 89].

This raises an intriguing problem: If we consider a deformation curve (stress vs. strain in case of strain-controlled testing, stress vs. time in case of creep testing), then this curve will consist of a sequence of N avalanches such that the total plastic strain is given by $\varepsilon_{\rm tot} = N\langle\Delta\varepsilon\rangle_N$ where $\langle\Delta\varepsilon\rangle_N$ is the average strain increment produced by each of the N events. Most of the avalanches will of course be very small. However, if we evaluate the contribution $\Delta\varepsilon^{(N)}_{\rm max}/\varepsilon_{\rm tot}$

[1] For brevity of presentation from hereon we use ε instead of $\varepsilon^{\rm pl}$ to symbolize plastic strain, which is the only strain we will be referring to.

of the largest event (of size $\Delta\varepsilon_{\max}^{(N)}$) to the total deformation, then we find a surprising result: For $p(\Delta\varepsilon) \propto \Delta\varepsilon^{-\kappa}$ with $1 < \kappa < 2$ we find that in the limit $N \to \infty$ this ratio tends towards a finite value less than 1 (see e.g. [90] where a similar calculation was performed for the area occupied by the largest cell in a cell structure with power-law distribution of the cell sizes). In other words, whatever the specimen size, the largest avalanche should always be directly visible on the macroscopic deformation curves. Experimentally, however, smooth behavior is observed on macroscopic scales and deformation bursts become apparent only when the specimen dimensions are reduced down to the micron scale.

Different explanations have been proposed to resolve this paradox. Zaiser and Moretti [86] proposed that the avalanche size may be limited by intrinsic hardening. Along similar lines, Richeton et al. [91] argued that the avalanche size in ice polycrystals may be limited by strong, grain-size dependent kinematic hardening induced by the strong plastic anisotropy of the material. Another possible explanation is that the avalanches might exhibit lamellar geometry (fractal dimension close to 2). Owing to the small volume involved in the deformation process, such avalanches would produce only a small macroscopic strain even if their magnitude is limited by the system size only. This idea is in agreement with traditional ideas about deformation localization in slip lines and slip bands [80], but also with recent experimental observations which indicate that deformation localizes in lamellar regions with local strains distributed according to a power law with exponent close to 1.5 [89]. Unlike the conjecture of Zaiser and Moretti, this proposition predicts an *extrinsic* limit to the avalanche size, in line with the idea of self-organized criticality.

In the following investigation we use a time-continuous generalization of the cellular automaton model of Zaiser and Moretti [86] to clarify the respective influences of intrinsic (hardening) and extrinsic (specimen shape and size, driving mode) parameters on the size of deformation bursts in crystal plasticity. The model formulation is also extended to include driving by an external 'machine' of variable stiffness. We then use the model to investigate avalanche size distributions and establish scaling relations which allow to estimate the size of the largest avalanches under various experimental conditions.

Chapter II.2
Description of the Model

In order to model the distinctive attributes of plastic flow associated with fluctuating behavior, we use a phenomenological constitutive model which builds on previous work by Zaiser and Moretti [86] and Zaiser and Aifantis [87, 92]. The model uses concepts of the dynamics of random media by assuming that plastic deformation of a given volume element involves a random sequence of hardening and softening processes. This idea provides a rather generic framework that covers a broad range of phenomena where heterogeneity and intermittency emerge. In this sense the model is not limited to dislocation-based crystal plasticity but can equally well be applied to the deformation of amorphous materials or even the rheology of yield-stress fluids. In the present work, however, we shall always try to relate the local hardening and softening processes to dislocation motions. By estimating the model parameters in a way that is consistent with the scaling properties of dislocation systems, we arrive at predictions that can be directly compared with experimental observations or simulations of dislocation plasticity. The model that is presented in the following preserves the basic structure of [86, 87] but improves and further develops the existing model by introducing various generalizations concerning the driving mode and the local resistance evolution in the system.

II.2.1 Basic structure of the model

We adopt as our starting point a rate-dependent crystal plasticity model including isotropic and kinematic hardening [3] on each slip system, as commonly used in engineering models of crystal plasticity. The basic idea of the model is to generalize the simple viscoplastic relation already presented in introductory Part 0 (Eq. (0.3.3)) to obtain the activation condition

$$|\tau^{(i)} - \tau_{\mathrm{b}}^{(i)}| > \tau_{\mathrm{f}}^{(i)} \tag{II.2.1}$$

and the evolution equation

$$\dot{\gamma}^{(i)} = \left\{ \frac{|\tau^{(i)} - \tau_{\mathrm{b}}^{(i)}| - \tau_{\mathrm{f}}^{(i)}}{\mu} \right\}^{m} \mathrm{sign}(\tau^{(i)} - \tau_{\mathrm{b}}^{(i)}) \,, \tag{II.2.2}$$

where m and μ are material parameters and the plastic shear strain rate $\dot{\gamma}^{(i)}$ equals 0 for the activation condition in Eq. (II.2.1) not being valid. $\tau^{(i)}$ is the local stress resolved in the respective slip system i and is obtained in the standard manner by solving the elastic problem. The stresses $\tau_{\mathrm{f}}^{(i)}$ ('flow stress') and $\tau_{\mathrm{b}}^{(i)}$ ('back stress') relate to isotropic and kinematic hardening, respectively. The constitutive model is complemented by phenomenological evolution equations which give all stresses as functions of the shear strains on the different slip systems, or relate them to the evolution of dislocation densities.

II.2.1.1 Evolution of the local flow stress

The flow stress in the constitutive equation Eq. (II.2.2) represents both lattice friction and the resistance that stems from the interactions of defects. Neglecting the constant contribution of lattice friction, we may say that the isotropic flow stress mimics, on a macroscopic scale, the action of 'microscopic' internal stresses (e.g., the stress fields of other dislocations). As we decrease the scale of our description, it is evident that the notion of a constant and isotropic flow stress cannot be sustained. Instead, the irregular fluctuations of the internal stress field on the scale of the individual defects become more and more apparent. Accordingly, we envisage τ_{f} as a fluctuating stress which we describe in a phenomenological manner taking into account the following observations:

- The work done locally by the internal stress along any sufficiently long strain path should be close to zero. (The internal stresses, on average, neither store nor dissipate energy.) In other words, the strain average of the fluctuating stress, $\langle \tau_{\mathrm{f}}(\boldsymbol{r}) \rangle_{\Delta\gamma} = (1/\Delta\gamma) \int_{\Delta\gamma} \tau_{\mathrm{f}}(\boldsymbol{r}, \gamma) \mathrm{d}\gamma$ should be zero for sufficiently large strain intervals $\Delta\gamma$.

  This requirement can be motivated by two observations: (i) Internal stresses by their very nature cannot dissipate energy, and this property should be retained in a phenomenological model. (ii) Energy can, in principle, be stored in the form of internal elastic stress fields. However, the amount of mechanical work stored, during plastic deformation of most metals, in the form of internal stress fields is often quite small (typically $< 10\%$) and decreases with increasing deformation, see [93]. As a consequence, it is a reason-

able approximation to set this fraction equal to zero. (Materials with strong kinematic hardening may be an exception to this rule.)

- The fluctuating stress field exhibits strong variations in space. As correlations in the arrangement of individual dislocation lines are restricted to a few dislocation spacings (Zaiser et al. [55, 93]), the same holds true for variations in the fluctuating stress field. Hence, flow stresses at locations separated by more than $\xi \approx 1/\sqrt{\rho}$ are statistically independent.

- Changes in the local value of the fluctuating stress correspond to changes in the local dislocation configuration. Such changes require a characteristic local strain increment $\gamma_{\mathrm{corr}} \approx \boldsymbol{b}\sqrt{\rho}$. Changes in the statistical properties of the fluctuating stress field, on the other hand, occur on the much larger strain scale characteristic of strain hardening.

- As we refrain from tracing the dislocation positions within each volume element, the high-dimensional dynamics of dislocation segments is mapped on a stochastic term in the stress evolution. Consequentially, the fluctuating stress is to be considered a stochastic variable. Its characteristic range of variation can be estimated by the mean passing stress between two dislocations.

As a phenomenological model which is in line with these observations, we assume that the evolution of the fluctuating stresses is governed by a simple Ornstein-Uhlenbeck process defined by the stochastic differential equation

$$\gamma_{\mathrm{corr}}\partial_\gamma \tau_{\mathrm{f}}(\boldsymbol{r},\gamma) = -\tau_{\mathrm{f}}(\boldsymbol{r},\gamma) + Qw(\boldsymbol{r},\gamma) \tag{II.2.3}$$

where $w(\boldsymbol{r},\gamma)$ is a Gaussian white-noise process with correlation function $\langle w(\boldsymbol{r},\gamma)w(\boldsymbol{r}',\gamma')\rangle = \xi f(|\boldsymbol{r}-\boldsymbol{r}'|)\delta(\gamma-\gamma')$ where the function f with the properties $f(0)=1$ and $\int f(u)\mathrm{d}u = \xi$ is a short-range function dropping to zero over the characteristic range ξ. The long-time solution of Eq. (II.2.3), $\tau_{\mathrm{f}}(\gamma,\boldsymbol{r})$ is a Gaussian stochastic process with the correlation function

$$\langle \tau_{\mathrm{f}}(\boldsymbol{r},\gamma)\tau_{\mathrm{f}}(\boldsymbol{r}',\gamma')\rangle = Q^2 \exp\left(-\frac{|\gamma-\gamma'|}{\gamma_{\mathrm{corr}}}\right) f(|\boldsymbol{r}-\boldsymbol{r}'|)\ . \tag{II.2.4}$$

Hardening implies an increase of the dislocation density and, concomitantly, of the internal-stress fluctuations. This is modelled in terms of a slow parametric evolution of the amplitude

$Q = \sqrt{\langle \tau_{\mathrm{f}}^2 \rangle}$ with strain:

$$\partial_t Q = q|\partial_t \gamma| \quad , \quad Q(0) = Q_0, \tag{II.2.5}$$

where $Q/q \gg \gamma_{\mathrm{corr}}$ (i.e. the relative rate of change of the stress fluctuation amplitude is small over the characteristic correlation strain γ_{corr}). The parameter q defines the hardening coefficient as we will see below.

II.2.1.2 Representation of the local back stress

Presence of strain gradients leads to accumulation of dislocations of the same sign. Thus an additional stress contribution emerges. The short-range repulsive interactions between dislocations have been shown to give rise to a back stress which, as deduced in the previous Part I, scales like the second gradient of strain (see also Groma et al. [54]). In the most general sense, this can be written as

$$\tau_{\mathrm{b}} = \nabla \boldsymbol{D} \nabla \gamma \tag{II.2.6}$$

where $\boldsymbol{D}$ is a tensor which, in the case of dislocation back stresses, scales like the inverse dislocation density.

II.2.1.3 Evaluation of the mesoscopic stress state

The final step consists of evaluating the shear stress τ on the active slip system. It is worth mentioning that due to the prescribed fluctuations in the local flow stress, different volume elements may exhibit different degrees of plastic deformation, i.e. the plastic shear strain field $\gamma(\boldsymbol{r})$ may be spatially inhomogeneous on the 'mesoscopic' scale of variation of $\gamma(\boldsymbol{r})$ even if the macroscopic deformation state might be spatially homogeneous. This case should be visualized as that of a dislocated body where stresses due to the applied surface tractions superimpose on internal stress fields created by the dislocation arrangement. Accordingly, we adopt a standard method for solving the boundary value problem at hand [94] by splitting the problem into three parts. In a first step, we consider the body under consideration as embedded into an infinite reference body and solve the problem of the internal stress state arising from the inhomogeneous shear strain field $\gamma(\boldsymbol{r})$ in the infinite body. In a second step, we restore free-surface boundary conditions by applying appropriate tractions on the actual surface of the deforming body. Finally, we account for the stresses arising from tractions and/or displacements that are prescribed on the surface.

We first consider the problem of evaluating the internal stress associated with an arbitrary inhomogeneous plastic distortion field created by crystallographic slip in an infinite body.

We consider a single slip system (situations with slip on multiple slip systems are simply treated by adding the respective stress contributions) and assume without loss of generality that the slip direction coincides with the x direction, and the y axis is normal to the slip plane. In this case, the plastic distortion field has the structure $\boldsymbol{\beta}^{\mathrm{pl}} = \gamma(\boldsymbol{r})\boldsymbol{e}_y \otimes \boldsymbol{e}_x$. The stresses associated with this distortion fields can be interpreted as arising from an arrangement of edge dislocations with density $\rho_{\mathrm{e}}(\boldsymbol{r}) = -\partial_x\gamma(\boldsymbol{r})$, and screw dislocations with density $\rho_{\mathrm{s}}(\boldsymbol{r}) = -\partial_z\gamma(\boldsymbol{r})$. Accordingly, the stress field can be written as

$$\boldsymbol{\sigma}_\infty(\boldsymbol{r}) = -\int \boldsymbol{\sigma}_{\mathrm{e}}(\boldsymbol{r}-\boldsymbol{r}')\partial_x\gamma(\boldsymbol{r}')\mathrm{d}^3r' - \int \boldsymbol{\sigma}_{\mathrm{s}}(\boldsymbol{r}-\boldsymbol{r}')\partial_z\gamma(\boldsymbol{r}')\mathrm{d}^3r' \,, \tag{II.2.7}$$

where $\boldsymbol{\sigma}_{\mathrm{e}}$ and $\boldsymbol{\sigma}_{\mathrm{s}}$ are the stress fields generated in an infinite medium by screw and edge dislocation segments of unit strength and unit length.

For plane-strain conditions, where γ depends on the x and y coordinates only, this simplifies to

$$\boldsymbol{\sigma}_\infty(\boldsymbol{r}) = -\int \boldsymbol{\sigma}_{\mathrm{e}}(\boldsymbol{r}-\boldsymbol{r}')\partial_x\gamma(\boldsymbol{r}')\mathrm{d}^2r' \,. \tag{II.2.8}$$

By partial integration, the stress field can alternatively be expressed as a functional of γ itself. In particular, by using the shear stress field of an edge dislocation we find that the resolved shear stress in the slip system under consideration can be written as

$$\tau_\infty(\boldsymbol{r}) = \int [\gamma(\boldsymbol{r}') - \bar{\gamma}]\Gamma(\boldsymbol{r}-\boldsymbol{r}')\mathrm{d}^2r' \,, \tag{II.2.9}$$

where $\bar{\gamma}$ is the strain at infinity (or the average strain along the infinite contour). The kernel Γ is given by

$$\begin{aligned} \Gamma(\boldsymbol{r}) &= \frac{G}{2\pi(1-\nu)}\left[\frac{1}{\boldsymbol{r}^2} - \frac{8x^2y^2}{\boldsymbol{r}^6}\right] \\ &- \frac{G}{4(1-\nu)}\delta(\boldsymbol{r}) \,. \end{aligned} \tag{II.2.10}$$

The first term contributing to Γ, which has zero angular average, leads to an anisotropic, nonlocal stress re-distribution. The second term, on then other hand, has mean-field character: According to this term, the local stress differs from the average stress by an amount that is

proportional to the difference between the local strain and the average strain in the infinite system.

For the case of a general three-dimensional strain field, the procedure of derivation is somewhat more involved. However, also in this case we can write the internal stress in an infinite body in the general form

$$\boldsymbol{\sigma_\infty}(\boldsymbol{r}) = \int \beta^{\mathrm{pl}}(\boldsymbol{r}')\boldsymbol{\Gamma}(\boldsymbol{r}-\boldsymbol{r}')\mathrm{d}^3 r' \; . \tag{II.2.11}$$

The problem of evaluating the Green's function $\boldsymbol{\Gamma}$ in the general case is discussed in detail by Zaiser and Moretti [86] as presented in Appendix B. Also in this case it can be shown that the internal stress state can be represented as a superposition of a mean-field contribution and a non-local anisotropic term.

Once the problem for the infinite body is solved, we prescribe tractions to offset the stress $\sigma_\infty(\boldsymbol{r})$ on the actual surface of the deforming body and restore free-surface conditions. Solving the corresponding elastic problem gives an additional stress contribution $\sigma_{\mathrm{surf}}(\boldsymbol{r})$. The sum $\sigma_\infty(\boldsymbol{r}) + \sigma_{\mathrm{surf}}(\boldsymbol{r})$ solves the internal-stress problem in the inhomogeneously deformed finite body with free surfaces.

Finally, we solve the elastic problem for the homogeneous finite body with imposed surface displacements and/or surface tractions. The resulting stress field $\sigma_{\mathrm{ext}}(\boldsymbol{r})$ is in the following termed the 'external' stress as it is related to the external action (as opposed to internal strain heterogeneity) on the deforming body.

II.2.2 Formulation for single slip

We consider plastic deformation by crystallographic slip on a single active slip system. Hence, the deformation state is completely characterized by the scalar shear strain field $\gamma(\boldsymbol{r})$. Gathering all the stress contributions described above and inserting them in Eq. (II.2.2) we obtain for the evolution of the shear strain the equation

$$\dot{\gamma} = \left\{ \frac{|\tau_{\mathrm{ext}} + \tau_\infty + \tau_{\mathrm{surf}} - \tau_{\mathrm{b}}| - \tau_{\mathrm{f}}}{\mu} \right\}^m \mathrm{sign}(\tau_{\mathrm{ext}} + \tau_\infty + \tau_{\mathrm{surf}} - \tau_{\mathrm{b}}) \; , \tag{II.2.12}$$

which for unidirectional deformation (no stress reversal) can be simplified by omitting the absolute value signs together with the $\mathrm{sign}(...)$ term. The first three stress terms in the expressions

on the right-hand side originate from solving the elastic problem for the (in general) inhomogeneously deformed body, whereas the second two terms describe the microscopic stresses that arise from defect interactions on a local scale. Without loss of generality, we assume that the slip direction corresponds to the x direction of a Cartesian coordinate system and the slip plane is the xz plane.

We assume plane-strain deformation (i.e. $\gamma = \gamma(x, y)$) and impose periodic boundary conditions to mimic a homogeneously sheared infinite body. Thus τ_{surf} is understood as the stress resulting from the periodic images of the simulation cell, and τ_{ext} is simply a constant. As noted by Zaiser and Moretti [86] for $m = 1$, Eq. (II.2.12) can be reshaped to become formally equivalent to the overdamped equation of motion of an elastic manifold:

$$\partial_t \gamma = \tau_{\mathrm{ext}} + \int \gamma(\boldsymbol{r}')\Gamma(\boldsymbol{r} - \boldsymbol{r}')\mathrm{d}\boldsymbol{r}' + D\gamma_{xx} + \tau_{\mathrm{f}}(\boldsymbol{r}, \gamma) \; . \tag{II.2.13}$$

This indicates that our model is in the universality class of elastic manifold depinning.

II.2.3 Numerical Implementation

We discuss the numerical implementation of our model for the linear-visoplastic case $m = 1$ (see also [95]). We discretize space by using a square lattice and identify the lattice constant with the characteristic correlation length $\xi \approx \rho^{-1/2}$ of the fluctuating flow stress field. Alternatively, we may view each lattice site as the characteristic volume occupied by a dislocation segment. Accordingly, ours is a 'minimal' discretization where deformation on each volume element occurs by movement of a single dislocation. Further, we assume $D = 0$ since, as far as the avalanche dynamics is concerned, the local interactions expressed by the gradient term are overshadowed by the effect of the long-range stress $\tau_\infty + \tau_{\mathrm{surf}}$. Because of the long-range character of this stress, deformation events usually occur at distant locations even though they pertain to the same slip avalanche. (We note that, on the other hand, the presence of the gradient term is essential for understanding the striated nature of the slip pattern, as discussed by Zaiser and Moretti [86].)

The strain field takes discrete values γ_{ij} at the lattice points. The long-range stress $\int \tau(\boldsymbol{r} - \boldsymbol{r}')\partial_x \gamma(\boldsymbol{r}')\mathrm{d}\boldsymbol{r}'$ is evaluated as the sum of the stresses of edge dislocations of strength $\gamma_{i+1,j} - \gamma_{ij}$ that are placed midway between the lattice points in the x direction. To conform with the

imposed periodic boundary conditions, the edge dislocation stress field must be considered as the stress field of a dislocation plus the Ewald sum over its infinitely many periodic images. This is evaluated in an approximate manner by first summing up analytically over the row of images in the direction perpendicular to the slip plane. This summation, which can be performed analytically (see Hirth-Lothe [96]), leads to an expression that decays exponentially in the slip direction, such that only a small number of images are needed in that direction in order to achieve good accuracy.

The stochastic fields $\tau_{\mathrm{f}ij} = \tau_{\mathrm{f}}(\boldsymbol{r}_{ij}, \gamma_{ij})$ are modelled as independent Ornstein-Uhlenbeck processes located at the respective lattice points. We allow positive strain increments only (rate-dependent implementations which allow the strain to locally decrease have been shown to yield similar results, see review by Zaiser [1]). In the simulations, the local strain at the lattice point (i, j) is increased by an amount $\Delta\gamma_{ij}$ proportional to the local driving stress according to the condition

$$\Delta\gamma_{ij} = \left(\tau_{\mathrm{ext}} - \int \tau(\boldsymbol{r}_{ij} - \boldsymbol{r}')\partial_x\gamma(\boldsymbol{r}')\mathrm{d}^2r' + \tau_{\mathrm{f}ij}(\gamma_{ij})\right)\Delta\gamma_0 > 0 \ , \tag{II.2.14}$$

where $\Delta\gamma_0$ is a small reference fixed amount. The strains are updated in parallel, and the new stresses are evaluated as detailed previously. The new deformation resistance is evaluated by using the finite-time solution of the Ornstein-Uhlenbeck process defined by Eq. (II.2.3):

$$\tau_{\mathrm{f}ij}(\gamma_{ij} + \Delta\gamma_{ij}) = a_{ij}\tau_{\mathrm{f}}(\gamma_{ij}) + \sqrt{1 - a_{ij}^2}Q^2 w_{ij} \ , \tag{II.2.15}$$

where $a_{ij} = \exp(-\Delta\gamma_{ij}/\gamma_{\mathrm{corr}})$, γ_{corr} is a correlation strain which characterizes the 'memory' of the stochastic process, $Q(= \langle\tau_{\mathrm{f}ij}^2\rangle)$ is the mean square amplitude of the pinning field, and the w_{ij} are statistically independent Gaussian variables of unit variance. For the process defined by Eq. (II.2.15), the two-point correlation function is $\langle\tau_{\mathrm{f}ij}(\gamma_{ij})\tau_{\mathrm{f}kl}(\gamma'_{kl})\rangle = \langle\tau_{\mathrm{f}ij}^2\rangle\delta_{ik}\delta_{jl}\exp[|\gamma_{ij} - \gamma'_{kl}|/\gamma_{\mathrm{corr}}]$.

II.2.3.1 External driving and strain hardening

Strain hardening means that the resistance of a material to deformation increases with increasing strain. In our case, the deformation resistance is a random field with zero mean. Strain hardening can be implemented by increasing the amplitude of this field. To this end, we increase the local amplitude in Eq. (II.2.15) in proportion with the local strain, $Q^2 = Q_0^2(1 + K\gamma_{ij})^2$

where $K(= q/Q_0)$ is a non-dimensional parameter that we use to adjust the average hardening rate.

In a strain-hardening system, sustained deformation requires a driving stress that on average increases with strain. In our simulations, we drive the system by using either stress control or displacement control with a machine of finite stiffness. In a stress-controlled simulation we simply increase the external stress $\tau_{\rm ext}$ from zero in small increments $\Delta\tau_{\rm ext}$. After each stress increment we check for all volume elements whether Eq. (II.2.14) is fulfilled. At the 'unstable' sites where this is the case, we increase the local strains and re-evaluate the local deformation resistances. After all sites are updated, we re-evaluate the local stresses everywhere in the system and perform another update. This is repeated until all sites are stable (Eq. (II.2.14) is no longer fulfilled for any site). Then we again increase the external stress, and so on.

In a displacement-controlled test, we impose the total deformation $\gamma_{\rm ext}$ and evaluate the stress according to

$$\tau_{\rm ext} = \Lambda[\gamma_{\rm ext} - \langle\gamma_{ij}\rangle] \,, \tag{II.2.16}$$

where Λ is called the 'machine stiffness'. In a quasi-static simulation we increase $\gamma_{\rm ext}$ (and thus the stress) at a small rate until at least one site fulfils Eq. (II.2.14) and becomes unstable. We then keep $\gamma_{\rm ext}$ fixed while we update in parallel the strains at all unstable sites as previously outlined. However, after each update we not only re-evaluate the local stresses and deformation resistances, but also the external stress which, owing to the increase of $\langle\gamma_{ij}\rangle$ during the update, is bound to decrease according to Eq. (II.2.16). Once all sites have stabilized, we again increase the imposed strain, and so on. The procedure can be visualized as 'pulling' the system with a spring of finite stiffness: As soon as the system yields, the spring is partly relaxed and the driving force decreases by an amount that is proportional to the spring stiffness.

II.2.3.2 Relation with physical parameters of dislocation systems

As discussed previously, our model can be applied to the shear deformation of any disordered material. In the present case, the disorder relates to the dislocation arrangement in a deforming crystal, and scaling relations link the model parameters to physical variables of the system: For a dislocation system of density ρ the characteristic correlation length of internal stress fluctuations in such systems is of the order of one dislocation spacing, $\xi \approx \rho^{-1/2}$ (for a detailed discussion, see Zaiser and Aifantis [87]). The volume occupied by one lattice site can be

identified with the characteristic volume occupied by a dislocation segment, $V_0 = \rho^{-3/2}$. The correlation strain $\gamma_{\rm corr}$ corresponds to the strain accomplished locally when such a dislocation segment crosses this elementary volume, $\gamma_{\rm corr} = b\sqrt{\rho}$ where b is the modulus of the Burgers vector of the dislocations. This also defines the natural unit of strain in a dislocation system. The deformation resistance $\tau_{\rm f}$, as all other stresses, scales like $Gb\sqrt{\rho}$ where G is the shear modulus. From the scaling of stress and strain it follows that the 'natural unit' of the hardening rate and the machine stiffness is simply the shear modulus G.

In the following all quantities will be given in these 'natural units'. The size s of a strain burst is defined as the sum of all strain increments that occur during a period of activity. The corresponding macroscopic strain is given by s/XY where the integers X and Y define the size of the lattice in the x and y directions.

Chapter II.3
Results

We use the model presented in the previous section to investigate the properties of strain bursts. To this end, we first discuss the qualitative features of the deformation response of our model and then proceed towards a quantitative characterization of the strain burst statistics. From this we finally deduce a general scaling law which governs the statistical properties of strain bursts under a wide range of deformation conditions.

II.3.1 General: Intermittent Plasticity

A typical stress-time signal obtained from a strain controlled simulation is shown in Figure II.3.1. This illustrates the burst-like nature in which deformation progresses. The serrated stress-strain curve results from the intermittent deformation bursts that are manifest on the strain rate vs. time curve shown in the inset. As the stress is given by $\tau_{\mathrm{ext}} = \Lambda(\gamma_{\mathrm{ext}} - \langle\gamma_{ij}\rangle)$, the observed strain bursts lead to irregular stress drops.

As discussed by Zaiser and Moretti [86], in the absence of hardening and under conditions of stress control, Eq. (II.2.13) shows a 'phase transition' between a pinned and a moving phase: Below a critical stress level which defines the yield stress of the system, the deformation rate asymptotically goes to zero, whereas above the critical stress, the deformation rate is asymptotically finite. It is noticeable that such a finite stress value exists even though the average τ_{f} (averaging at fixed $\boldsymbol{r}$ over all γ) is zero. This implies that our system with the inhomogeneous distribution of plastic strains is trapped in configurations which result in a negative average friction stress, with a magnitude that depends on the fluctuation amplitude Q_0. Thus in a stress-controlled simulation and in the absence of hardening, the external stress passes through an initial transient until it reaches the yield stress, at which point the strain increases indefinitely.

In our simulations, we choose the initial value of Q_0^2 in such a manner that the yield stress is about 0.3 (dimensional value $0.3Gb\sqrt{\rho}$), in line with typical experimental findings in fcc metals. The correlation strain γ_{corr} is set equal to unity, and the parameter K is used to tune

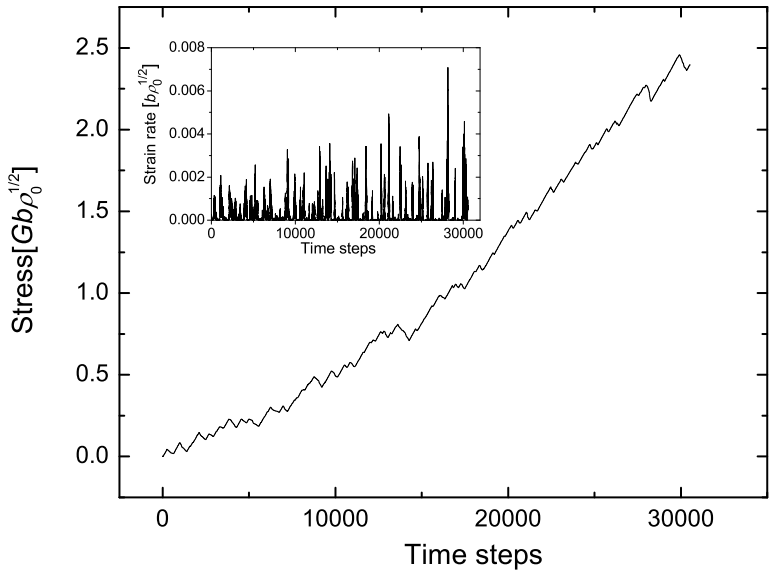

Figure II.3.1: *Stress-time signal as obtained from simulation of a system with* 32×32 *sites; Inset: cumulative strain rate vs. time. The serrated stress profile should be attributed to the intermittent strain response which owning to the finite driving stiffness results in relaxation stress drops.*

the hardening rate Θ. We also systematically vary the machine stiffness Λ and the system size. There are no other parameters in the model.

Figure II.3.2 shows three deformation curves (external stress vs. average strain) obtained for different values of the machine stiffness and hardening rate. In a displacement-controlled simulation we observe that the external stress fluctuates slightly below the yield-stress level: Close to the yield stress, slip avalanches are triggered which decrease the external stress, after an avalanche is terminated the external stress rises again, and so on. In the presence of hardening, the mean stress after the initial transient increases first slowly ('Stage I') and then at a higher, approximately constant rate ('Stage II'). Statistics of slip avalanches were determined in this constant-hardening stage (above a strain of approximately 40 in Figure II.3.2). The hardening rate Θ was defined as the average slope of the stress-strain curve in this regime, with the average either determined from the stress-strain curve of a very large system or from the average of many smaller systems. Both methods were found to yield similar results.

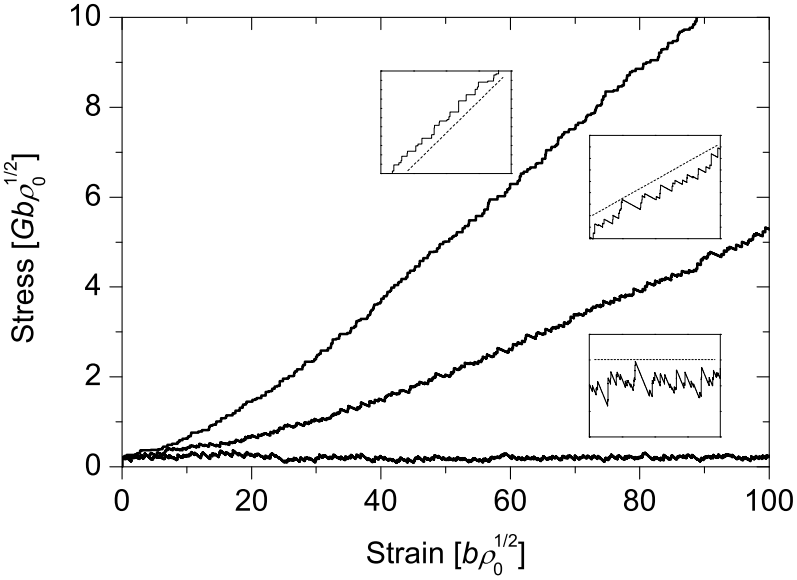

Figure II.3.2: *Stress-strain curves as obtained from simulation of a system with* 64×64 *sites; from top to bottom: hardening rate* $\Theta = 0.125$*, machine stiffness* $\Lambda = 0$*; hardening rate* $\Theta = 0.0625$*, machine stiffness* $\Lambda = 0.0625$*, hardening rate* $\Theta = 0$*, machine stiffness* $\Lambda = 0.125$*. Inserts show magnified the fluctuating behavior.*

II.3.2 Avalanche sizes and scaling characteristics

To determine avalanche statistics, several series of simulations were carried out (Table II.3.1). For a system driven in a quasi-static manner we envisage avalanches as the cumulative slip response succeeding a load increase. As soon as a stress step destabilizes a single position on the simulated grid, by means of imposing slip s adequate to relieve the local stress state, it triggers a mechanism that forces the whole system to a new stable position. This is due to interactions linking the system in a long range trend and hence activating through a single instability a network of slip incidents extending over the entire contour. Summing up slip events of of all activated regions for a single stress increment defines the size of the avalanche which spatially forms into patterns of intriguing complexity. Generally, the avalanche size distributions obey the scaling relation

$$p(s) \propto s^{-3/2} g(s/s_0) \tag{II.3.1}$$

where s_0 is the characteristic avalanche size and the function g can for our simulations be approximated by $g(s/s_0) \approx \exp[-\frac{1}{3}(s/s_0)^2 + (s/s_0)]$.

Series	Fixed parameters	Varied parameter	Variation range
1	$\Lambda = 1,\ \Theta = 0$	system size	$32 \times 32 \ldots 128 \times 128$
2	$\Lambda = 0.5,\ \Theta = 0$	system size	$16 \times 16 \ldots 128 \times 128$
3	$\Lambda = 0.25,\ \Theta = 0$	system size	$32 \times 32 \ldots 128 \times 128$
4	$\Lambda = 0.125,\ \Theta = 0$	system size	$64 \times 64 \ldots 128 \times 128$
5	$\Lambda = 0,\ \Theta = 0.0065$	system size	$32 \times 32 \ldots 128 \times 128$
6	$\Lambda = 0,\ \Theta = 0.013$	system size	$32 \times 32 \ldots 128 \times 128$
7	$\Lambda = 0,\ \Theta = 0.026$	system size	$32 \times 32 \ldots 256 \times 256$
8	$\Lambda + \Theta = 0.125$, $X = Y = 64$	stiffness Λ	$0 \ldots 0.125$
9	$\Lambda = 0.125$, $\Theta = 0$, X = 16	extension Y	$16 \ldots 128$
10	$\Lambda = 0.125$, $\Theta = 0$, Y = 16	extension X	$16 \ldots 128$

Table II.3.1: *Series of simulations carried out in this study. Scans over the variation ranges were performed by changing the respective parameters by a factor of two between two simulations in a series.*

Distributions corresponding to series 1-4 on Table II.3.1 are shown in Figure II.3.3. It can be seen that an increase in machine stiffness Λ leads to a decrease and an increase of system size to an increase in s_0. This is to be expected, since the machine decreases the driving stress, during an avalanche of size s, by an amount $\Lambda s/N$ where N is the number of lattice sites. This causes large avalanches to self-terminate. A more quantitative analysis can be performed by fitting Eq. (II.3.1) to the distributions to determine the characteristic size s_0 as a function of the simulation parameters. Interestingly, it turns out that s_0 scales as $s_0 \propto L/\Lambda$ where L is the linear dimension of the system, rather than $s_0 \propto N/\Lambda \propto L^d/\Lambda$ where d is the system dimension. This finding is consistent with the lamellar shape observed for plastic slip avalanches and it is crucial for the subsequent claims in our analysis.

II.3.3 Equivalence of hardening and machine-driving

Hardening locally increases the pinning strength of the system at those sites that are actually involved in a slip avalanche. Machine-induced stress relaxation decreases the global driving force on all sites. Both effects should have equivalent consequences for the avalanche statistics if the depinning transition of the system shows mean-field behavior.

Figure II.3.4 shows avalanche size distributions determined from an ensemble of simulations

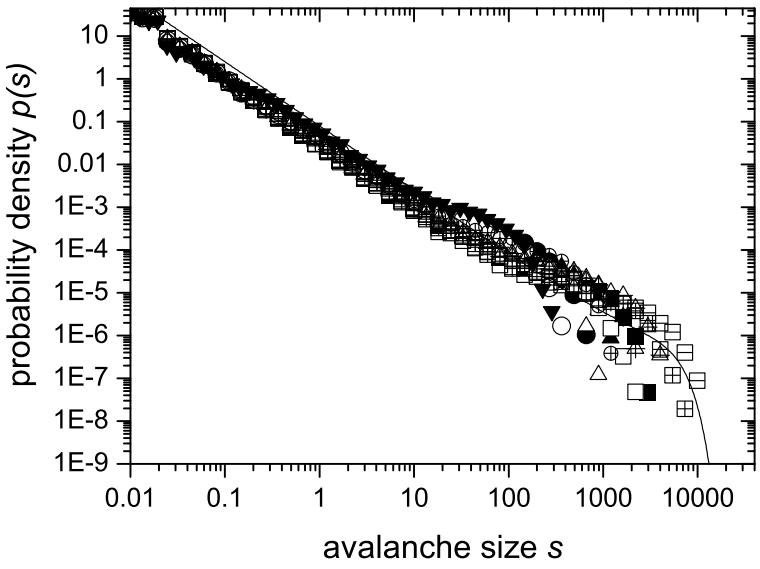

Figure II.3.3: *Avalanche size distributions corresponding to simulation series 1 (open symbols), series 2 (full symbols), series 3 (cross-centered symbols) and series 4 (bar-centered symbols). Symbol shape indicates system size: square* 128×128*, up triangle* 64×64*, circle* 32×32*, down triangle* 16×16*.*

similar to those shown in Figure II.3.2. Different machine stiffnesses and hardening rates were imposed such that the sum $\Lambda + \Theta$ was the same for all simulations. It can be seen that three sets of simulations ($\Lambda = 0, \Theta = 0.125$; $\Lambda = \Theta = 0.0625$; $\Lambda = 0.125, \Theta = 0$) yield exactly the same distribution of avalanche sizes, which is well described by the scaling form (II.3.1). This demonstrates that strain hardening and machine-induced stress relaxation indeed have similar effects on the avalanche dynamics. As a consequence, the avalanche cutoff s_0 must depend on the sum $\Theta + \Lambda$ of the hardening rate and machine stiffness, rather than on Θ and Λ separately.

II.3.4 Scaling law for the characteristic avalanche size

After performing several series of simulations at different hardening rates (series 5-7 in Table II.3.1) and determining the characteristic size s_0 for each set of parameters, it was found that the scaling of the cut-off can, over the entire parameter range investigated, be described by the

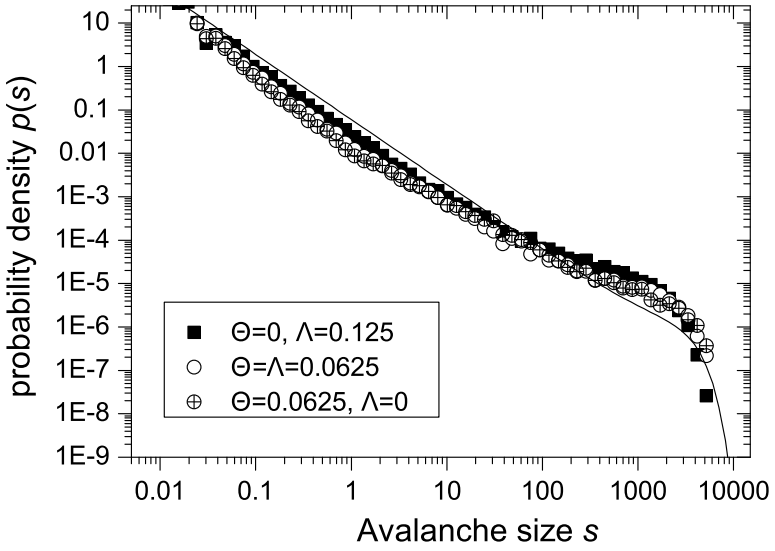

Figure II.3.4: *Avalanche size distributions for three different systems of size* 64×64*; Parameters* Λ *and* Θ *see inset; Full line: fit according to Eq. (II.3.1), with* $s_0 = 1700$*.*

general scaling law

$$s_0 = \frac{CL}{(\Lambda + \Theta)} \, . \tag{II.3.2}$$

A fit to all data yields $C \approx 3$ (Figure II.3.5). A number of simulations for anisotropic specimen shapes were also conducted. In this case we found approximately the same scaling law, with L defined as the square root of the number of lattice sites (Series 9 and 10 in Figure II.3.5).

The scaling law, Eq. (II.3.2), represents the main result of our analysis. Its validation by comparison with the results of discrete dislocation simulations and its consequences will be addressed in the next section.

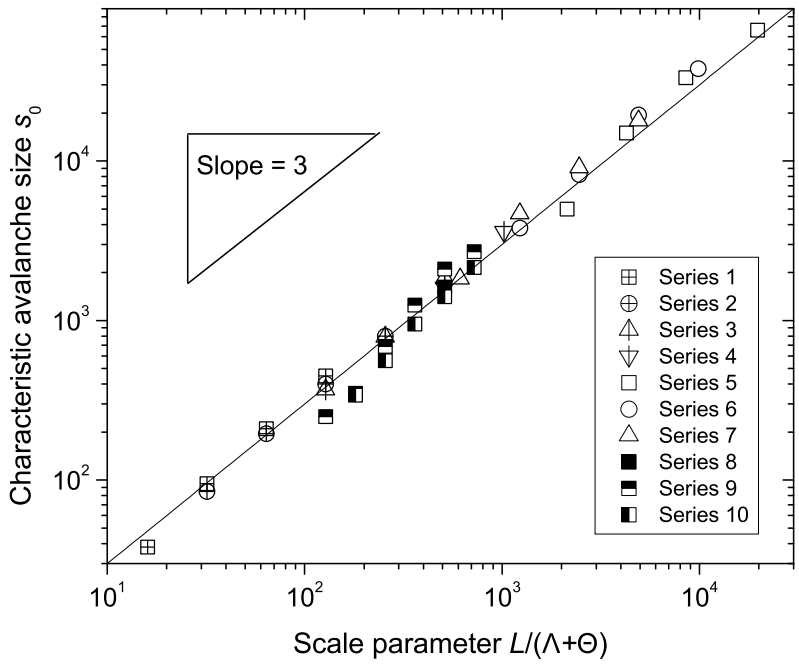

Figure II.3.5: *Scaling of the avalanche cutoff with hardening rate Θ, machine stiffness Λ, and linear system dimension L. Full line:* $s_0 = 3L/(\Lambda + \Theta)$.

Chapter II.4
Evaluation and Implications

In the current study we used a stochastic continuum model to capture the erratic microplastic response. Inevitably, this model relies on a number of phenomenological though physically motivated assumptions. The main target was to investigate the fluctuation properties and scaling characteristics of the microplastic response. Plastic strain bursts seem to be following a power law distribution consistently for a wide range of sizes but critical behavior is eventually hindered by a characteristic upper threshold controlled by both extrinsic and intrinsic parameters of the deformed system, which impose a limit on the size of the largest avalanches.

Thus we can intuitively hold responsible such internal and external barriers for the appearance of smooth and homogeneous plastic behavior on the macroscopic scale. However, we still have to demonstrate that the behavior of our model faithfully represents the behavior of dislocation systems. Additionally, as depicted in the introductory remarks, there is an apparent contradiction between the behavior of our model and the experimental observations based on AE monitoring of burst-like plastic deformation. The AE burst size distributions show no upper threshold and thus seem to indicate scale-free critical behavior. So is there a contradiction and what is the mechanism explaining fluctuating plasticity? Can this mechanism be accurately replicated through our simple model? The simple scaling relation deduced earlier allows us to address most of these questions. In the following we use a comparative approach when we put our findings into the context of results from 3DDD simulations [72, 73] and tension experiments on nickel micropilars [82] in order to illustrate the order that governs small scale plasticity.

II.4.1 Scaling considerations

In Figure II.4.1 we compare the typical intermittent and jerky-like evolution of stress and strain fields as obtained both from this modelling attempt and from more elaborate and time consuming 3DDD calculations. The two signals share common attributes in the sense that stress-strain curves are serrated and strain rate vs. time curves exhibit intermittent bursts of widely varying

magnitude. However, these qualitative attributes would be of little importance if the underlying statistics were different. Thus we try to convert the avalanche distributions obtained in the previous section, which characterized avalanches by the size s, into distributions of strain increments as obtained by Csikor et al.[72] from 3DDD simulations, in order to allow productive comparisons.

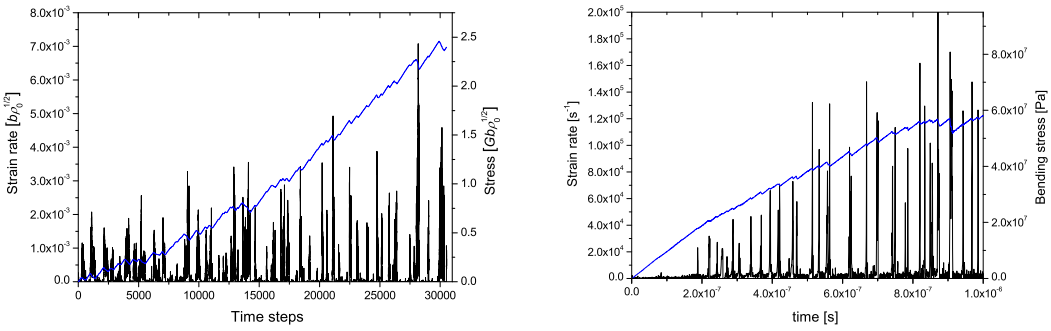

Figure II.4.1: *Stress-strain (blue lines) combined with strain rate vs. time signals. Left: Signal corresponding to the simulated homogeneous shearing of a system of size* 32×32 *with hardening and driven by a machine of finite stiffness. Right: Signal corresponding to the deformation response of a bending beam as obtained by 3DDD simulations. After Csikor et al. [72] and Motz and Weygand [73].*

We first revert to dimensional variables. The average shear strain increment produced by an avalanche of size s_0 is given by s_0/N. In dimensional units, this becomes $\Delta\gamma_{\max} = CbG/l(\Theta + \Lambda)$ where l is the (dimensional) specimen length. Using that the axial plastic strain ε is related to the shear strain by $\varepsilon = \Delta l/l = m\gamma$ where m is the Schmid factor, we find that

$$\Delta\varepsilon_{\max} = \frac{CbGm}{(\Lambda + \Theta)l} \,, \tag{II.4.1}$$

with $C = 3$ and $m \approx 0.4$. Csikor et. al. in [72] used the scaled variable $\epsilon = \Delta\varepsilon L(\Lambda_\varepsilon + \Theta_\varepsilon)/\mathrm{E}b$, where Λ_ε, Θ_ε are defined in terms of axial strains. To convert to this variable we use the relations $\mathrm{E} = 2G(1+\nu)$ and $\partial\tau/\partial\gamma = m^2\partial\sigma/\partial\varepsilon$. Eventually we can reformulate the previously deduced scaling law for $p(s)$ (cf. Eq. II.3.1) in terms of the scaled strain increment ϵ as $p(\epsilon) \propto \epsilon^{-3/2}\exp[-3\epsilon^2 + 3\epsilon]$.

Figure II.4.2 compares this relation with the results of 3DDD simulation and experimental data of Dimiduk et al. All data collapse in a very consistent way in the power law distribution pre-

dicted by our analysis. The strain cutoff size evaluated appears to be inversely proportional to the specimen size, which explains why transition to larger scales smears out the effect of fluctuations. In the elaborate treatise of Csikor et al. [72] a great number of possible modifications of the dislocation dynamics (multiple slip orientation, cross slip activation) were found to be irrelevant for the strain burst statistics. It is remarkable that simulations yield the scaling to be consistent even for the case of heterogeneous deformation modes such as bending where the existence of GNDs does not seem to alter the statistics of avalanches. Hence, it is rational to say that the avalanche characteristics we derive are generic and not dependent upon details other than the hardening, the driving and the system size.

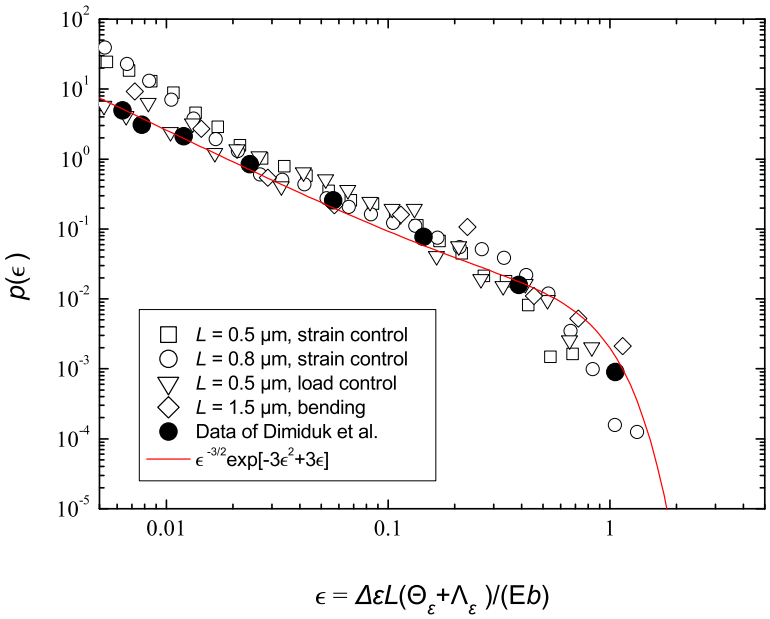

Figure II.4.2: *Collapse of the strain increment distribution to a single relation. The red line is the curve deduced from our continuum simulations. 3DDD data (after Csikor et al. [72]) correspond to varying deformation geometries, driving modes and specimen sizes. Experimental data from Dimiduk et al. are given in full dots.*

We can also note from Eq. (II.4.1) that the maximum axial deformation given by

$$\Delta l_{\max} = \frac{CbGm}{(\Lambda + \Theta)} \tag{II.4.2}$$

does not depend on specimen size. For typical values of the involved parameters $\Theta \approx G/1500$, $b = 2.5 \times 10^{-10}$ m we find that the length increments caused by the largest bursts are expected

to be about 0.5 microns. This compares very well with the maximum burst sizes observed by Dimiduk et al. and allows to have a feeling of when the interplay of scales starts to become apparent.

Moreover we can now provide a simple explanation unveiling the mystery of the absent cutoff in AE experiments: AE energies are proportional to the dissipated energy during an avalanche, hence they depend on the strain ε as $\sigma\varepsilon V$, where σ is the stress and V the volume. Such a quantity can experience sizing constraints with a cutoff roughly analogous to L^2 thus in macroscopic samples the upper limit of the scaling regime becomes very large and cannot be found in time series of limited duration.

Recapitulating our main arguments, the proposed scaling relation is nothing but a robust inclusion on the SOC idealization of plasticity of three fundamental parameters that exert strong influence on the deformation behavior yielding it eventually to be near critical but not actually critical. Namely the stress drop associated with hardening and machine stiffness prevents the emergence of avalanches of arbitrary size as required by critical behavior. Further the lamellar geometry which constrains the largest avalanches to a system-spanning shape implies that the average strain produced by these avalanches decreases in proportion with the linear dimension of the specimen, thing which follows naturally from the fact that each avalanche corresponds to the formation of a lamellar slip line or slip band. All these effects were systematically studied in the context of a 3DDD analysis [72, 73]. The outcomes produced totally match the proposed scaling.

II.4.2 Discussion and Outlook

The conjecture of an only near scale free plastic behavior is of high value for many practical purposes in modelling and understanding material deformation. If indeed present, SOC behavior would overturn all the long standing knowledge and experience on constitutive modelling by canceling the existence of a Representative Volume Element which is cornerstone for any homogenization-based continuum model. The evidence shows, however, that homogeneized continuum models work reasonably well in most macroscale applications. This motivates the quest for the scale limits below which models that incorporate randomness and heterogeneity can no longer be avoided. The simple scaling arguments presented here provide reliable estimates of the fluctuating response and allow to predict the cases where deterministic classical

models break down. Illustration of the transition to an anomalous and irregular response with decreasing size was vividly given by Csikor et al. [72]. As shown in Figure II.4.3 application of these stochastic findings to the bending of thin rods demonstrates that once the size of the deformed body becomes comparable to the largest event size, formability becomes problematic and unheralded.

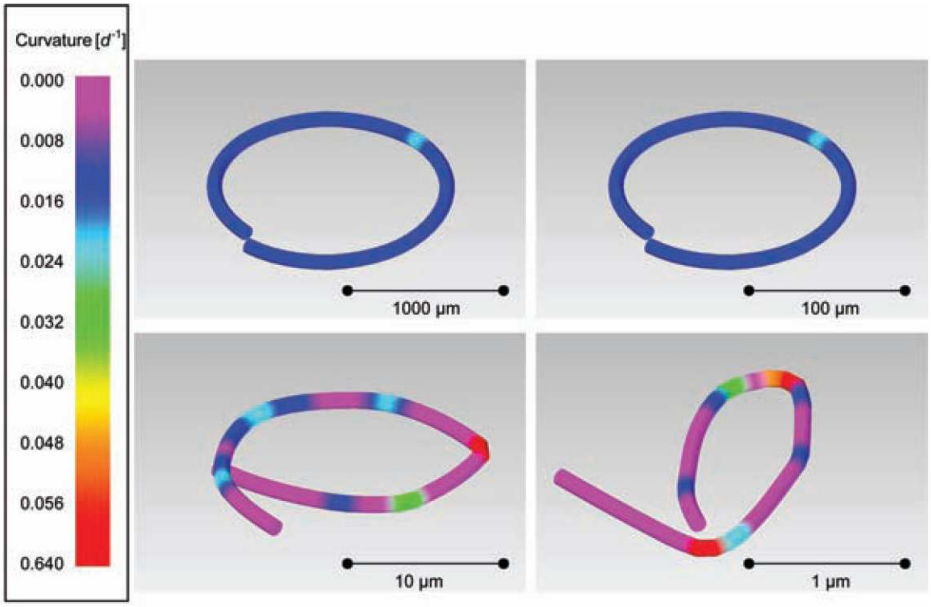

Figure II.4.3: *Shapes of rods (aspect ratio 1:50) after simulated bending; rod thickness t from top left to bottom right: $t = 100$ µm, $t = 10$ µm, $t = 1$ µm, $t = 0.1$ µm; $b = 2.8 \times 10^{-10}$ m, $\Lambda_\varepsilon = \mathrm{E}/1000$; the color code indicates the local bending angle over a segment of length t. In the last rod, the maximum avalanche size occurring in the simulations falls below the intrinsic cut-off of the distribution. After Csikor et al. [72].*

The current work provides a simple rule for assessing size influences on plasticity fluctuations. Although our model is restricted to a single slip geometry and a simple homogeneous driving mode it derives results that have a more or less generic applicability. Extension to polycrystalline aggregates [97] though doesn't seem viable. The random distribution of grains and the existence of intergranular forces seem to mask a similar relation (if any) and set the grain effect to be the variable dominating the power law exponent and the sizing of the cutoff.

Another issue that may raise questions, concerns the way we incorporate hardening into our stochastic continuum model. Although we explicitly account for a hardening related increase of the flow resistance in terms of an increasing fluctuation amplitude, we fail to account for the correlation length decrease which follows the corresponding dislocation density increase.

Thus the realism that emerges out of the patterning phenomena and the consequent dislocation clustering (for instance on cyclic deformation conditions) is disregarded. A straightforward generalization would be to implement on our coarse grained idealization the composite model of Mughrabi [98, 99] which can reveal some of the attributes of heterogeneous dislocation structures.

Conclusions

In the present work we tried to elucidate and understand some of the distinctive attributes that emerge in plastic deformation of crystalline materials on very small scales. We formally investigated the applicability of continuum descriptions to a problem that its nature resides on the individual dynamics of discrete and randomly distributed defects. In the context of our analysis we elaborated on two different strategies that can both produce concise idealizations of reality. Namely we adopted the stances first of deterministic and then of stochastic modelling in two seemingly disjunct parts. For both we demonstrated results that were in agreement both with experimental findings and with computational simulations based on three-dimensional discrete dislocation dynamics. In the present, concluding chapter we eventually attempt to illustrate the complementary rather than competitive perspective of the two approaches we used in the present work.

Initially we treated the long-standing problem of size-affected plastic response emerging in confined deformation geometries. It is well established that such a behavior is due to the competition of external with underlying characteristic internal length scales when these approach each other. Any physically motivated yet phenomenological continuum description is bound to start from quantifying such evolving internal length scales in a way consistent with the notion of a structureless continuous medium. We here invoke a framework combining a detailed characterisation of the average dislocation density evolution on a higher dimensional space together with latest findings of statistical physics of the average internal stress fields accompanying the dislocation existence. Analogous treatises, originally dating years back, failed because of the inadequacy of the average dislocation density description to replicate consistently the real state of deformation, as the effect of dislocations with zero average Burgers vector was not taken into account properly. The incorporation of the additional orientation and curvature parameters enabled us to deduce diffusion-like evolution equations which we proved to be excellent for capturing the deformation state development, in a mean field perspective, and concomitantly the size dependent response.

A key element for obtaining realistic results in line with experimental findings lies in taking into account the back stress contribution of dislocations with same sign which was hitherto ignored. We show that inclusion of line tension induced stresses on the local dynamics achieves to repro-

duce size dependent behavior, as shown in similar treatises which follow alternate derivations. However, we illustrate that sustained hardening and quantitative coherence with experiment are only obtained by including strain gradient terms stemming from dislocation correlations and nominally treated as an additional back stress. Such contributions, essentially phenomenologically scaled, in a way support the gradient additions to macroscopic constitutive laws that during the 80s and 90s dominated the field.

Our results for the case of a bended thin metal film revealed a power law dependence of the yield stress on thickness with a power exponent ≈ -1.5. Such a law seems to accurately represent experimental findings on bending of micron sized metallic films. Additionally outputs from an elaborate 3DDD series of simulations strikingly revealed a functioning resemblance through seizing not only the stress-strain response but also the dislocation density evolution and the local plastic strain distributions for the same set of fitted parameters. Of course such a similitude with 3DDD data can be recovered only on an average basis.

Typical stress-strain signals obtained from these simulations for a number of different initial conditions are pictured in Figure C1. The stress strain curves exhibit a serrated shape whereas the dislocation density vs. strain plots illustrated in Figure C2 display a staircase-like morphology. The nature of the random steps in both cases is the same. They originate from the strongly intermittent dynamics of interacting dislocation lines which are trapped at rest for long times before they relieve the stress in rapid, correlated motions which produce strain avalanches. In the bending geometry used in the simulations leading to Figures C1 and C2, each strain increment is associated with the storage of geometrically necessary dislocations, and each strain burst therefore leads to a step-like increase in dislocation density. Figure C3 illustrates the time evolution of dislocation density together with the instantaneous strain rate signal and the matching of the sharp irregular peaks to the discrete stress steps is clear. Analogous findings can be seen also in compression experiments of micropillars, Figure C4, though this time non-existence of geometrically necessary dislocations hinders the direct connection of activity bursts with dislocation density variations.

A complete treatise of plasticity needs to address this fluctuating behavior and the second part of this work attempts to do so. Investigations conducted on the size distribution of observed strain avalanches agree that these distributions are characterized as scale-free since power laws seem to hold for a wide range of scales. The concept of Self Organized Criticality already applied to similar crackling noise phenomena appears able to capture many features of the observed

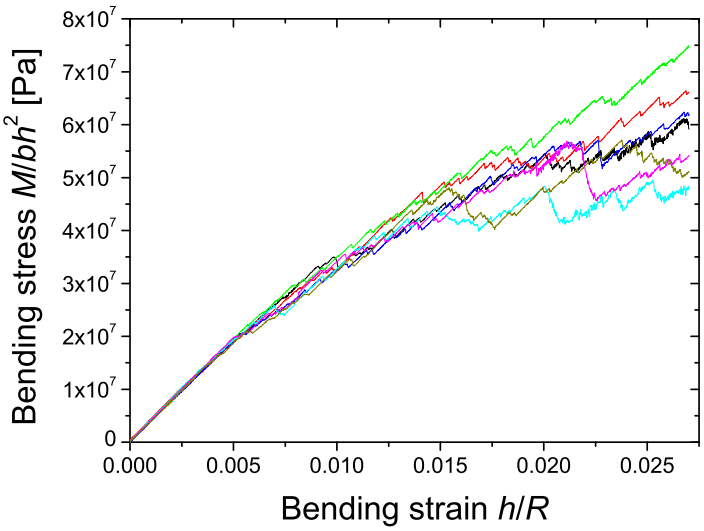

Figure C1: *Stress-strain behavior in 3DDD simulations of microbending with different but statistically equivalent initial dislocation configurations. Although the average behavior is smooth and accessible by deterministic modelling (see Figure I.4.4), individual curves have a serrated shape with stress drops corresponding to deformation avalanches. Data after Motz and Weygand [73].*

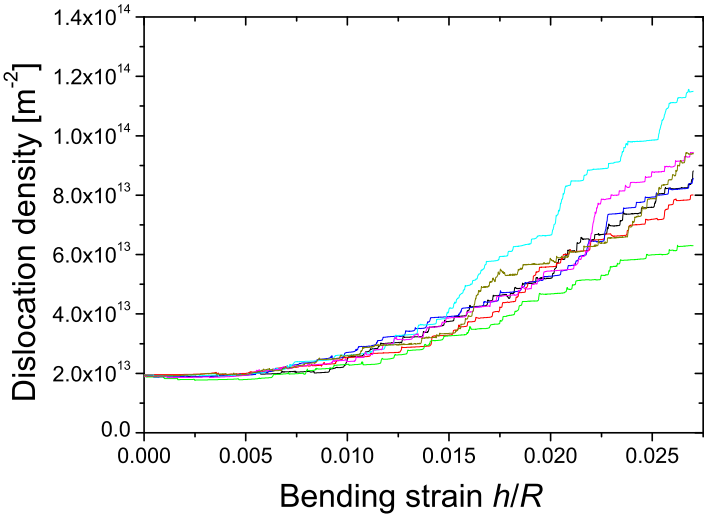

Figure C2: *Dislocation density vs. strain plots in 3DDD simulations of microbending. The staircase-like shape is again a signature of the avalanche induced deformation: during each avalanches the dislocation density jumps upwards. Data after Motz and Weygand [73].*

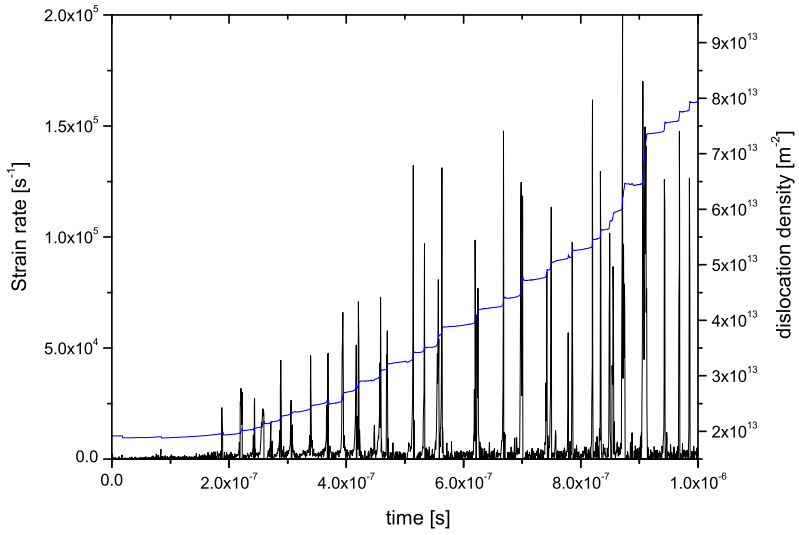

Figure C3: *Signals of strain rate and dislocation density (blue line) evolution in 3DDD simulations of microbending. Bursts of strain activity give rise to a stairway-like morphology for the density evolution, corresponding to GNDs accumulation, with step increments of varying size that again seem to be following a power law distribution. Data after Motz and Weygand [73]*

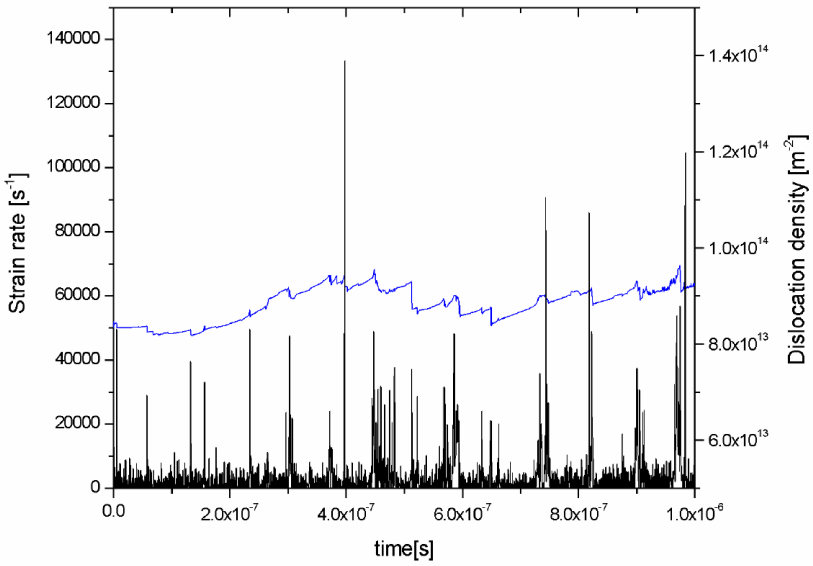

Figure C4: *Signals of strain rate and dislocation density (blue line) evolution in 3DDD simulations of uniaxial compression. Instantaneous fluctuations in the dislocation density should not contribute to any net change as in bending. Strain bursts of activity operate in a manner that cannot be directly ascribed to the short variations in the dislocation density value. Data after Csikor et al. [72].*

dynamics, though it cannot capture the decay of fluctuations on the transition to macroscale.

We address this problem by using a continuum model which allows to account for fluctuating deformation behavior by means of a random local flow stress. We relate all features of the model to the underlying dislocation dynamics and thus derive a model with no explicit dislocation reference but with a profound microstructural insight. In particular we show that in complete agreement with experiments, strain bursts of plastic activity are power law distributed with a power exponent ≈ 1.5 and a cut-off indicating the existence of some characteristic maximum size. We examine the effect of various system parameters on the formation of such a cutoff and eventually propose a scaling relation which infers the maximum burst size. Demonstrating that the maximum axial plastic strain scales in inverse proportion with the system size it becomes clearly comprehensible why fluctuations die out in the world our bare eyes witness. We prove that our scaling proposal accurately fits both the outcomes of Csikor et al. [72] and the experimental findings of Dimiduk et al. [82]. Moreover although we confine our analysis to a single slip geometry, 3DDD simulation outcomes suggest that our simple relation should be deemed as a universal plasticity attribute. It is shown that changing most details, for instance by allowing for multiple slip systems or enabling cross slip, leaves the observed scaling unchanged.

Summing up, this work illustrates that a holistic description of crystal plasticity by use of conventional continuum tools is not an impossible objective. We showed that an average response estimate is feasible and can be attained by use of the elaborate density-based dislocation dynamics framework formulated by Hochrainer and Zaiser. All size-dependent characteristics of crystal plasticity surface at this stage. Yet as always a mean value description of a parameter means nothing if we don't possess knowledge of its fluctuation behavior. We find that a simple stochastic description, in the spirit of earlier SOC modelling attempts, provides adequate scaling relations to capture the distribution of any deviations and hence fully define the plasticity problem in hand.

Probably the most interesting result of this analysis is a question for future investigations which if answered could provide the bridge between discrete dislocation simulation and dislocation-based continuum models. Inspecting Figure C2 we can fit, as previously in the concluding remarks of Part I, a smooth average curve. Each simulation by itself is characterized by large fluctuations which result from complex dynamics with sensitive dependence on initial conditions. In spite of this complexity, the average response can be correctly predicted on the basis

of comparatively simple transport equations. This implies an enormous reduction of complexity which is at the core of the possibility of using continuum models. It is important to note that this reduction of complexity is not the simple result of a spatial coarse-graining operation - indeed, the size of the simulations is so small that it falls below the characteristic size of any 'representative volume element' that would be needed to define spatial averages in a meaningful manner. Instead, the averages are performed over ensembles of initial conditions and it remains to be understood which features of the dynamics allow each autonomous realization of the 3DDD calculations to behave in such a manner that, in spite of the complex and intermittent fluctuation behavior, the average response allows for a simple continuum description.

Appendices

Appendix A
Derivation of the edge-screw model

We start out from the fundamental kinetic equation (I.2.8),

$$\partial_t \rho = -\partial_\phi[\rho v_\phi] - \nabla \cdot [\rho \boldsymbol{v}] + \rho v k \ . \tag{A.1}$$

Note that, for a discrete dislocation system, the density function ρ has the structure $\rho = \rho(\boldsymbol{r})\delta(\phi - \phi(\boldsymbol{r}))$ since the dislocation orientation is uniquely defined in each point. The partial densities R_s and R_e are given by

$$R_\mathrm{s}(\boldsymbol{r}) = \int \rho \cos\phi \mathrm{d}\phi \quad , \quad R_\mathrm{e}(\boldsymbol{r}) = \int \rho \sin\phi \mathrm{d}\phi \ . \tag{A.2}$$

and for a discrete system the local dislocation orientation can be expressed through the relation $\tan\phi = R_\mathrm{s}(\boldsymbol{r})/R_\mathrm{e}(\boldsymbol{r}) = R_\mathrm{s}/R_\mathrm{e}$. Inserting these relations into the kinetic equation, and assuming an orientation-independent dislocation mobility (no explicit dependence of $|v|$ on ϕ), we find

$$\begin{aligned} \partial_t R_\mathrm{s} &= R_\mathrm{s} v k - R_\mathrm{e}(\boldsymbol{e}_\mathrm{t}\nabla)v - \frac{R_\mathrm{s}}{\rho}(\boldsymbol{e}_\mathrm{g}\nabla)[\rho v] \ , \\ \partial_t R_\mathrm{e} &= R_\mathrm{e} v k + R_\mathrm{s}(\boldsymbol{e}_\mathrm{t}\nabla)v - \frac{R_\mathrm{e}}{\rho}(\boldsymbol{e}_\mathrm{g}\nabla)[\rho v] \ . \end{aligned} \tag{A.3}$$

Finally we use that the dislocation glide and tangent vectors are given by $\boldsymbol{e}_\mathrm{g} = \sin\phi \boldsymbol{e}_x - \cos\phi \boldsymbol{e}_y = (R_\mathrm{e}/\rho)\boldsymbol{e}_x - (R_\mathrm{s}/\rho)\boldsymbol{e}_y$ and $\boldsymbol{e}_\mathrm{t} = \cos\phi \boldsymbol{e}_x + \sin\phi \boldsymbol{e}_y = (R_\mathrm{s}/\rho)\boldsymbol{e}_x + (R_\mathrm{e}/\rho)\boldsymbol{e}_y$, respectively. This leads to

$$\partial_t R_\mathrm{e} = \left[-\frac{R_\mathrm{e}^2}{\rho^2}\partial_x(\rho v) + \frac{R_\mathrm{e}R_\mathrm{s}}{\rho^2}\partial_y(\rho v)\right] + R_\mathrm{s}\left[\frac{R_\mathrm{s}}{\rho}\partial_x v + \frac{R_\mathrm{e}}{\rho}\partial_y v\right] + R_\mathrm{e} v k \ , \tag{A.4}$$

$$\partial_t R_\mathrm{s} = \left[-\frac{R_\mathrm{e}R_\mathrm{s}}{\rho^2}\partial_x(\rho v) + \frac{R_\mathrm{s}^2}{\rho^2}\partial_y(\rho v)\right] - R_\mathrm{e}\left[\frac{R_\mathrm{s}}{\rho}\partial_x v + \frac{R_\mathrm{e}}{\rho}\partial_y v\right] + R_\mathrm{s} v k \ . \tag{A.5}$$

When averaging these equations, it is necessary to consider terms of the type $\langle R_\mathrm{s}^2/\rho^2\rangle$ or $\langle R_\mathrm{s}/\rho\rangle$. The average is understood as an average over some mesoscopic volume ΔV and all orientations of segments within that volume. To prove some useful relationships, we divide all dis-

location lines contained within ΔV into short segments of length l, which we label with the discrete index β. The edge and screw lengths of a given segment are $l_{\rm s}^{\beta} = l\cos\phi_{\beta}$ and $l_{\rm e}^{\beta}$. Clearly, $\rho = N_V l/V$ where N_V is the number of segments in V, and $\kappa_{\rm s,e} := \langle R_{\rm s,e}\rangle = \sum_{\beta\in V} l_{\rm s,e}^{\beta}/V$. It is then easy to see the identities

$$\begin{aligned}\langle\frac{R_{\rm e}^2}{\rho^2}\rangle &= \frac{1}{V}\sum_{\beta\in V}\frac{(l_{\rm e}^{\beta})^2}{l} = \frac{1}{N_V}\sum_{\beta\in V}\frac{(l_{\rm e}^{\beta})^2}{l^2}\frac{N_V}{l}V = \frac{\langle R_{\rm e}^2\rangle}{\langle\rho^2\rangle}\ ,\\ \langle\frac{R_{\rm e}^2}{\rho}\rangle &= \frac{1}{N_V}\sum_{\beta\in V}\frac{(l_{\rm e}^{\beta})^2}{l^2} = \frac{\sum_{\beta\in V}(l_{\rm e}^{\beta})^2}{\sum_{\beta\in V} l^2} = \frac{\langle R_{\rm e}^2\rangle}{\langle\rho^2\rangle}\langle\rho\rangle\ ,\end{aligned} \tag{A.6}$$

and similarly for $R_{\rm s}$.

Appendix B
Evaluation of long-range internal stresses

We calculate the internal stresses in an infinite three-dimensional body with an arbitrary plastic distortion field $\boldsymbol{\beta}^{\mathrm{pl}}(\boldsymbol{r})$. The external stress is assumed to be zero. (A non-zero external stress simply adds to the internal stresses.) We start out from the elastic equilibrium equation for the components σ_{ij} of the stress tensor

$$-\partial_j \sigma_{ij} = f_i \ , \tag{B.1}$$

where f_i are the body forces and sums are performed over repeated indices. The above equation can be rewritten in terms of the components u_i of the elastic displacement vector as

$$-\partial_j C_{ilkl} \partial_k u_l = f_i, \tag{B.2}$$

where C_{ijkl} are components of Hooke's tensor. The solution of Equation (B.2) has the form

$$u_i(\mathbf{r}) = \int \Gamma_{ik}(\mathbf{r} - \mathbf{r}') f_k(\mathbf{r}') d^3 r' \tag{B.3}$$

where the Fourier transform of the elastic Green's tensor $\Gamma_{ik}(\mathbf{r})$ is $\tilde{\Gamma}_{ik}(\mathbf{k}) = [-C_{ijkl} k_j k_l]^{-1}$.

We now first consider the particular problem of a plastically deformed 'inclusion' where the plastic distortion has a constant value β^{pl} over a certain volume V and is zero elsewhere. This *inclusion problem* is solved as follows: The volume V is first cut out of the surrounding matrix and deformed plastically in order to produce a stress-free strain β^{pl}. To re-insert it into the matrix, interface tractions are applied, such that the original shape is restored. According to Equation (B.1) these interface tractions are

$$f_i = C_{ijkl} \beta^{\mathrm{pl}}_{kl} \partial_j H_V(\mathbf{r}), \tag{B.4}$$

where the function $H_V(\mathbf{r})$ is equal to unity within V and zero elsewhere. The volume is then placed in its original position and relaxed. Elastic relaxation proceeds until the tractions pro-

duced by the relaxation strain β^{r} balance those given by Equation (B.4). The Fourier transform of the corresponding displacement field is

$$u_i^r(\mathbf{k}) = i\Gamma_{ik}(\mathbf{k})C_{klmn}\beta_{mn}^{\mathrm{pl}}k_l H_V(\mathbf{k}) \ . \tag{B.5}$$

The total elastic distortion is then the sum of the relaxation strain and the initial distortion $-\beta_{ij}^{\mathrm{pl}}H_V(\mathbf{r})$ applied to "restore" the original shape before relaxation. The associated total stress reads $\sigma_{ij}(\mathbf{r}) = C_{ijkl}(\beta_{kl}^{\mathrm{r}} - \beta_{kl}^{\mathrm{pl}}H_V(\mathbf{r}))$ and its Fourier transform is

$$\sigma_{ij}(\mathbf{k}) = -C_{ijlm}\left(k_m k_o \tilde{\Gamma}_{ln}(\mathbf{k})C_{nopq} + \frac{1}{9}\delta_{lp}\delta_{mq}\right)\beta_{pq}^{\mathrm{pl}}H_V \ . \tag{B.6}$$

The angular average

$$\tilde{\Gamma}_{ijlm}^0 = \frac{1}{4\pi}\int C_{ijno}[k_o k_q \tilde{\Gamma}_{np}(\mathbf{k})C_{pqlm} + \frac{1}{9}\delta_{ln}\delta_{mo}]d\Omega \tag{B.7}$$

does not depend on the modulus k of the wavevector since $\tilde{\Gamma}_{np}$ scales like k^{-2}. The stress hence can be written as

$$\sigma_{ij}(\mathbf{k}) = [-\tilde{\Gamma}_{ijlm}^0 + \tilde{\Gamma}^*(\mathbf{k}/k)]\beta_{lm}^{\mathrm{pl}}H_V(\mathbf{k}) \ , \tag{B.8}$$

where the second term is simply defined by $\tilde{\Gamma}^*(\mathbf{k}/k) = C_{ijno}[k_o k_q \tilde{\Gamma}_{np}(\mathbf{k})C_{pqlm} + \frac{1}{9}\delta_{ln}\delta_{mo}] - \tilde{\Gamma}_{ijlm}^0$.

The above procedure can be straightforwardly generalized for an arbitrary distribution of the plastic distortion $\beta^{\mathrm{pl}}(\mathbf{r})$ by considering each volume element as a separate "inclusion". Equation (B.8) becomes

$$\sigma_{ij}(\mathbf{k}) = [-\tilde{\Gamma}_{ijlm}^0 + \tilde{\Gamma}^*(\mathbf{k}/k)]\beta_{lm}^{\mathrm{pl}}(\mathbf{k}) \tag{B.9}$$

and, in real space,

$$\sigma_{ij}(\boldsymbol{r}) = -\tilde{\Gamma}_{ijlm}^0\beta_{lm}^{\mathrm{pl}}(\mathbf{r}) + \int \Gamma^*(\mathbf{r}-\mathbf{r}')\beta_{lm}^{\mathrm{pl}}(\mathbf{r}')d^3r' \ . \tag{B.10}$$

The non-local kernel $\Gamma^*(\mathbf{r}-\mathbf{r}')$ is the inverse Fourier transform of $\tilde{\Gamma}^*(\mathbf{k}/k)$; it scales like $1/r^2$ in two-dimensional space and like $1/r^3$ in three dimensional space and has zero angular average. What has been done so far holds for strain fields that go to zero at infinite distances. If the asymptotic value of the plastic strain assumes a non-zero value $\beta^{\mathrm{pl},\infty}$, we have to add the

corresponding stress-free strain as follows:

$$\sigma_{ij}(\mathbf{k}) = \tilde{\Gamma}^0_{ijlm}[\beta^{\mathrm{pl},\infty}_{lm} - \beta^{\mathrm{pl}}_{lm}(\mathbf{r})] + \int \Gamma^*(\mathbf{r}-\mathbf{r}')\beta^{\mathrm{pl}}_{lm}(\mathbf{r}')d^3r'. \tag{B.11}$$

For a plastic distortion field which has the *average* value $\langle\beta^{\mathrm{pl}}\rangle$, the asymptotic value $\beta^{\mathrm{pl},\infty}$ is replaced by the average $\langle\beta^{\mathrm{pl}}\rangle$ since the fluctuation contributions average out if integrated over the infinite contour. Hence, the internal stress can be envisaged as the sum of a mean-field contribution and a non-local term with a kernel of zero angular average.

References

Publications

Articles in International Journals

M. Zaiser, N. Nikitas, T. Hochrainer and E. C. Aifantis, *Modelling size effects using 3D density-based dislocation dynamics*, Phil. Mag. **87** Nos 8-9 1283 (2007).

M. Zaiser and N. Nikitas, *Slip avalanches in crystal plasticity: scaling of the avalanche cut-off*, J. Stat. Mech. P04013 (2007).

Conference Proceedings

M. Yang, V. Koutsos, N. Nikitas and M. Zaiser, *Size effects in tensile failure of defected carbon nanotubes with defects - from atomistic simulation to continuum models*, in: 2005 Joint ASME/ASCE/SES Conference on Mechanics and Materials (McMAT2005), (Baton Rouge, USA, 2005), 3.T1.N.4.

N. Nikitas, *Dislocation-Motivated Constitutive Equations and Application to size effects in constrained plastic flow*, in: 3rd Int. Conf. on Multiscale Materials Modelling, (Freiburg, Germany, 2006), pp. 358.

Bibliography

[1] M. Zaiser, Advances in Physics **54** 185 (2006).

[2] U. F. Kocks, in *Unified Constitutive Equations for Creep and Plasticity: Constitutive Behavior Based on Crystal Plasticity*, edited by A. K. Miller, (Elsevier Appl. Sci., 1987), pp. 1-88.

[3] C. Teodosiu, in *Large Plastic Deformation of Crystalline Aggregates: Dislocation Modelling of Crystalline Plasticity*, edited by C. Teodosiu, (Springer-Verlag, CISM, 1996), pp. 21-80.

[4] *Dislocations in Solids: On dislocation patterning*, edited by H. Suzuki, T. Ninomiya, K. Sumino, S. Takeuchi, (Tokyo Univ. Press, 1985).

[5] E. C. Aifantis, Mater. Sci. Eng. **81** 563 (1986).

[6] M. Zaiser and E. C. Aifantis, *Materials Instabilities and Deformation Patterning in Plasticity, In: Recent Research Developments in Metallurgical and Materials Sciences* Vol. 3, (Research Signpost, Trivandrum, 1999), pp. 79-103.

[7] E. C. Aifantis, in *Defects Fracture and Fatigue: Dislocation kinetics and the formation of deformation bands*, edited by G. C. Sih and J. W. Provan, (Martinus-Nijhoff, The Hague, 1981), pp. 75-84.

[8] E. C. Aifantis, Int. J. Non-Linear Mech. **31** 797 (1996).

[9] A. Kelly and R. B. Nicholson, Prog. Mater. Sci. **10** 151 (1963).

[10] R. Ebeling and M. F. Ashby, Phil. Mag. **13** 805 (1966).

[11] U. Essmann, M. Rapp and M. Wilkins, Acta Metall. **16** 1275 (1968).

[12] M. D. Uchic, D. M. Dimiduk, J. N. Florando, W. D. Nix, Science **305** (2004).

[13] N. A. Fleck, G. M. Muller, M. F. Ashby and J. W. Hutchinson, Acta Metall. **42** 475 (1994).

[14] J. S. Stölken and A. G. Evans, Acta Mater. **46** 5109 (1998).

[15] P. Shotriya, S. M. Allameh, J. Lou, T. Bucheit and W. O. Soboyejo, Mech. Mater. **35** 233 (2003).

[16] C. Motz, T. Schöberl and R. Pippan, Acta Mater. **53** 4269 (2005).

[17] M. A. Haque and M. T. A. Saif, Acta Mater. **51** 3053 (2003).

[18] W. D. Nix and H. Gao, J. Mech. Phys. Solids **46** 411 (1998).

[19] H. Gao, Y. Huang, W. D. Nix, and J. W. Hutchinson, J. Mech. Phys. Solids **47** 1239 (1999).

[20] E. C. Aifantis, Int. J. Fracture **95** 299 (1999).

[21] E. C. Aifantis, Mechanics of Materials **35** 259 (2003).

[22] I. Tsagrakis, A. Konstantinides and E. C. Aifantis, Mechanics of Materials **35** 733 (2003).

[23] A. Needleman and J. Gil Sevillano, Scripta Materialia **48** 109 (2002).

[24] M. Zaiser and E. C. Aifantis, Scripta Materialia **48** 133 (2002).

[25] B. Devincre and M. Condat, Acta Metall. Mater. **40** 2629 (1992).

[26] B. Devincre and L. P. Kubin, Mater. Sci. Eng. A **8** 234 (1997).

[27] N. M. Ghoniem, S. H. Tong and L. Z. Sun, Phys. Rev. B **61** 913 (2000).

[28] H. M. Zbib, T. D. de La Rubia, R. Rhee and J. P. Hirth, J. Nucl. Mater. **276** 154 (2000).

[29] V. Bulatov, J. F. Justo, W. Cai, *et al.*, Phil. Mag. A **81** 1257 (2001).

[30] Y. U. Wang, Y. M. Jin, A. M. Cuitino and A. G. Khachaturyan, Acta Mater. **49** 1847 (2001).

[31] M. Koslowski, A. M. Cuitino and M. Ortiz, J. Mech. Phys. Solids **50** 2597 (2002).

[32] A. Acharya, Journal Mech. Phys. Solids **49** 761 (2001).

[33] A. Acharya, Phil. Mag. **87** 1349 (2007).

[34] U. F. Kocks, J. Eng. Mater. Technol. **98** 76 (1976).

[35] L. P. Kubin and Y. Estrin, Rev. Phys. Appl. **23** 573 (1988).

[36] D. Kuhlmann-Wilsdorf and J. H. Van Der Merwe, Mater. Sci. Eng. **55** 79 (1982).

[37] L. Holt, J. Appl. Phys. **41** 3197 (1970).

[38] K. Kondo, in *Proc. 2. Japan Nat. Congress of Appl. Mech.* (1952).

[39] J. F. Nye, Acta Metallurgica **1** 152 (1953).

[40] E. Kröner, *Kontinuumstheorie der Versetzungen und Eigenspannungen* (Springer-Verlag, Berlin, 1958).

[41] T. Mura, Phil. Mag. **8** 843 (1963).

[42] A. M. Kosevich, in *Dislocations in Solids*, edited by F. R. N. Nabarro, Vol. 1, (North Holland, Amsterdam, 1979), pp. 33-142.

[43] E. Kröner, *Continuum theory of defects* (North Holland, Amsterdam, 1981).

[44] D. J. Bammann and E. C. Aifantis, Acta Mechanica **45** 91 (1982).

[45] D. Walgraef and E. C. Aifantis, J. Appl. Phys. **58** 688 (1985).

[46] D. Walgraef and E. C. Aifantis, Res Mechanica **23** 161 (1988).

[47] J. Pontes, D. Walgraef and E. C. Aifantis, Int. J. Plasticity **22** 1486 (2006).

[48] A. E. Romanov and E. C. Aifantis, Scripta Met. Mat. **29** 707 (1993).

[49] A. E. Romanov and E. C. Aifantis, Scripta Met. Mat. **30** 1293, 1581 (1994).

[50] E. C. Aifantis, J. Eng. Mater. Tech. **121** 189 (1999).

[51] E. C. Aifantis, Int. J. Plasticity **3** 211 (1987).

[52] H. M. Zbib and E. C. Aifantis, Res Mechanica **23** 261, 279, 293 (1988).

[53] P. Hähner, Mater. Sci. Eng. A **164**, 23 (1993).

[54] I. Groma, F. Csikor and M. Zaiser, Acta Mater. **51** 1271 (2003).

[55] M. Zaiser, M.-C. Miguel, and I. Groma, Phys. Rev. B **64** 224102 (2001).

[56] I. Groma, G. Györgyi and B. Kocsis, Phil. Mag **87** 1185 (2007).

[57] S. Yefimov, I. Groma and E. Van der Giessen, J. Mech. Phys. Solids **52** 279 (2004).

[58] S. Yefimov, I. Groma and E. Van der Giessen, Modelling Simul. Mater. Sci. Eng. **12** 1069 (2004).

[59] A. El-Azab, Phys. Rev. B **61** 11956 (2000).

[60] R. Sedlacek, J. Kratochvil, and E. Werner, Phil. Mag. **83** 3735 (2003).

[61] T. Hochrainer, M. Zaiser and P. Gumbsch, Phil. Mag. **87** 1261 (2007).

[62] T. Hochrainer and M. Zaiser, in *Fundamentals of a continuum theory of dislocations in Proc. International Conference on Statistical Mechanics of Plasticity and Related Instabilities.* , PoS(SMPRI2005)002 (2006).

[63] M. Zaiser and T. Hochrainer, Scripta Mater. **54** 717 (2006).

[64] M.-C. Miguel, A. Vespignani, M. Zaiser and S. Zapperi, Phys. Rev. Letters **89** 165501 (2002).

[65] M. Zaiser and A. El-Azab, in *Multiscale Phenomena in Materials*, edited by H. M. Zbib, D. H. Lassila, L. E. Levine and K. J. Hemker, MRS Proceedings, Vol. 779, (MRS, Warrendale (PA), 2004), W5.7.

[66] A. El-Azab, J. Deng and M. Tang, Phil. Mag. **87** 1201 (2007).

[67] J. Kratochvil, in *Proc. 2nd Int. Conf. on Multiscale Materials Modelling*, Ed. N.M. Ghoniem, (UCLA 2004), pp. 221-223.

[68] A. Arsenlis, D. M. Parks, R. Becker, V. V. Bulatov, J. Mech. Phys. Solids **52** 1213 (2004).

[69] W. D. Nix, Metallurgical Transactions **20** 2217 (1989).

[70] R. Sedlacek, Mater. Sci. Eng. A **393** 387 (2005).

[71] R. Sedlacek and E. Werner, Phys. Rev. B **69** 134114 (2004).

[72] F. F. Csikor, C. Motz, D. Weygand, M. Zaiser and S. Zapperi, Science **318** 251 (2007).

[73] C. Motz and D. Weygand, in preparation.

[74] S. Sun, B. L. Adams and W. E. King, Phil. Mag. A **80** 9 (2000).

[75] J. Y. Shu, N. A. Fleck, E. Van der Giessen and A. Needleman, J. Mech. Phys. Solids **49** 1361 (2001).

[76] R. Dickman, M. A. Munoz, A.Vespignani and S. Zapperi, Braz. J. Phys. **30** 27 (2000).

[77] R. Frigg, Stud. Hist. Phil. Sci. **34** 613 (2003).

[78] H. J. Jensen, *Self-Organized Criticality - Emergent Complex Behavior in Physical and Biological Systems* (Cambridge University Press, New York, 1998).

[79] E. C. Aifantis, Int. J. Engng. Sci. **30** 1279 (1992).

[80] H. Neuhäuser, in *Dislocations in Solids*, edited by F. R. N. Nabarro, Vol. 4, (North-Holland, Amsterdam, 1984), pp. 319-440.

[81] M. Zaiser, F. Madani Grasset, Vasileios Koutsos and E. C. Aifantis, Phys. Rev. Letters **93** 195507 (2004).

[82] D. M. Dimiduk, C. Woodward , R. LeSar, and M. D. Uchic , Science **26** 1188 (2006).

[83] K. Chen and P. Bak, Phys. Rev. A **43** 625 (1991).

[84] M.-C. Miguel, A. Vespignani, S. Zapperi, J. Weiss, and J.-R.Grasso , Nature **410** 667 (2001).

[85] J. Weiss and J.-R Grasso, J. Phys. Chem. B **101** 6113 (1997).

[86] M. Zaiser and P. Moretti, J. Stat. Mech. P08004 (2005).

[87] M. Zaiser and E. C. Aifantis, Int. J. Plasticity **22** 1432 (2006).

[88] M. Koslowski, R. LeSar and R. Thomson, Phys. Rev. Letters **93** 125502 (2004).

[89] J. Schwerdtfeger, E. M. Nadgorny, F. Madani-Grasset, V. Koutsos, J. R. Blackford and M. Zaiser, J. Stat. Mech. L04001 (2007).

[90] M. Zaiser, K. Bay and P. Hahner, Acta Materialia **47** 2463 (1999).

[91] T. Richeton, P. Dobron, F. Chmelik, J. Weiss and F. Louchet, Mater. Sci. Engng. A **424** 190 (2006).

[92] M. Zaiser and E. C. Aifantis, submited.

[93] M. Zaiser and A. Seeger, in *Dislocations in Solids*, edited by F. R. N. Nabarro, Vol. 11, (North-Holland, Amsterdam, 2002), pp. 1-100.

[94] E. Van der Giessen and A. Needleman, Modelling Simul. Mater. Sci. Eng. **3** 689 (1995).

[95] M. Zaiser and N. Nikitas, J. Stat. Mech. P04013 (2007).

[96] J.P. Hirth and J. Lothe, *Theory of Dislocations* (McGraw Hill, New York, 1968).

[97] T. Richeton, J. Weiss and F. Louchet, Nature Materials **4** 465 (2005).

[98] H. Mughrabi, Acta Metall. **31** 1367 (1983).

[99] H. Mughrabi, Rev. Phys. Appl. **23** 367 (1988).